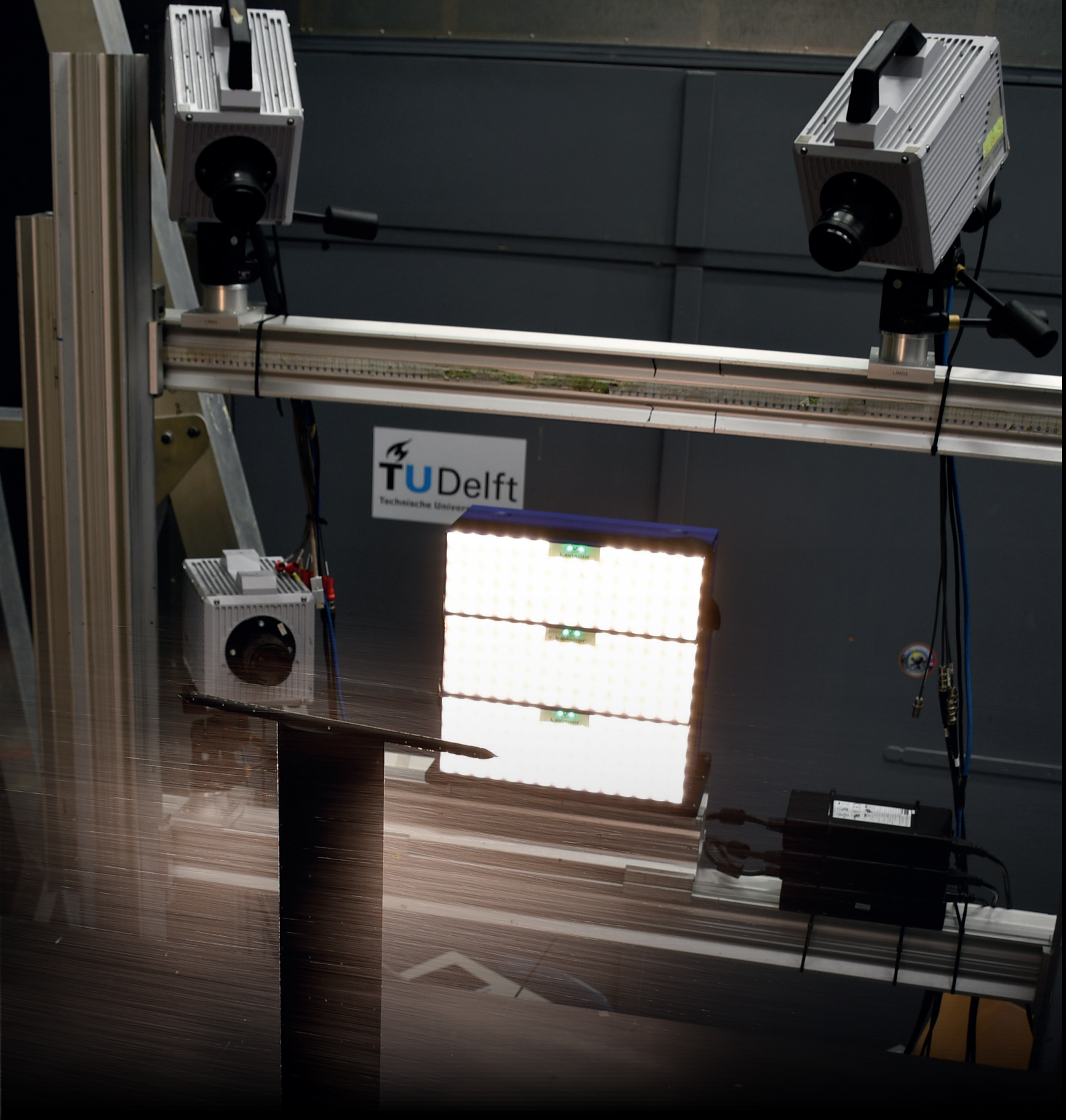

Aerodynamic load evaluation on a highly flexible wing by Lagrangian Particle Tracking

J. L. Costa Fernández

TU Delft

Aerodynamic load evaluation on a highly flexible wing by Lagrangian Particle Tracking

by

José Luis Costa Fernández

to obtain the degree of Master of Science
at the Delft University of Technology,
to be defended publicly on March 10th, 2022 at 10:00 a.m.

Student number:	5145694	
Project duration:	September 2020 - February 2022	
Thesis committee:	Dr.ir. B.W. van Oudheusden,	TU Delft, Chair
	Dr. A. Sciacchitano,	TU Delft, supervisor
	Dr. J. Sodja,	TU Delft, supervisor
	Ir. C. Mertens,	TU Delft, daily supervisor
	Dr. C. Ferreira,	TU Delft, external examiner

An electronic version of this thesis is available at http://repository.tudelft.nl/.

TU Delft

Acknowledgements

This master thesis marks the culmination of my studies in aerospace engineering, being definitely a special occasion to look back and think about all the help I have received throughout this long journey.

I would first like to thank Dr. Andrea Schiacchitano, Dr. Bas van Oudheusden and Dr. Jurij Sodja for giving me the opportunity to take part in this research project as a master's student. Furthermore, I would also like to thank them for their continuous supervision and advice. Their genuine interest and support, together with their invaluable experience and knowledge, guided me along this journey, pushing me to do better and explore areas that were previously hidden to me. I really hope this master thesis has been successful in making a small contribution to the large-scale experimental aerodynamics field.

Secondly, I would especially like to thank Christoph Mertens for his inestimable advice and support over the past 15 months. I have really enjoyed working with you. Your sense of humour, patience and constructive criticism have helped me grow, both professionally and personally. Due to the unexpected and difficult circumstances, I faced during the project, I really think that it is fair to say that, without your almost daily assistance and motivation, I would have given up on reaching the final objective of graduating and completing this thesis. I would also like to acknowledge your help and Andrián's with the Lagrangian Particle Tracking measurements during the wind tunnel experiments.

On the other hand, I would also like to thank my roommates Andreu, Carlos and Josema for being a priceless support during my stay at Delft. Their positive vibes contributed to the creation of a unique atmosphere in a place I called home over the last two years. I am also extremely thankful for all my MSc Aerospace Engineering colleagues. Thank you Thomas, Fabio, Miguel and Ravi for guiding me and helping me take my first steps at the Aerospace Faculty; I always felt welcomed when you were around. A special mention to my fellow compatriots Marina, Oscar and Xavi. Your friendship has helped me feel a bit closer to our home country during these hard moments and I really hope I will continue to enjoy it over many years.

Por último y más importante, me gustaría dar gracias a mi familia, especialmente a mis padres. Es difícil describir cómo de agradecido estoy por todo lo que habéis hecho por mi. Vuestro ejemplo y esfuerzo son una constante fuente de inspiración. No puedo agradeceros lo suficiente el apoyo que he sentido en cada una de las decisiones que he tomado en estos últimos años. Espero poder haber correspondido vuestro esfuerzo y que estéis orgullosos de lo que he conseguido. A ti Rocío, no hay nada que pueda decir que no te haya dicho ya. Espero que esta tesis marque un punto y seguido en la aventura de nuestras vidas. Gracias por estar siempre ahí.

José Luis Costa Fernández
Delft, February, 2022

Abstract

The minimization of pollutant emissions throughout the complete life-cycle of modern aircraft is one of the greatest demands that aviation faces nowadays. The implementation of lightweight structures constitutes an appealing improvement towards the achievement of sustainable aviation in the foreseeable future. Nevertheless, the use of such flexible structures might lead to challenging Fluid-Structure Interaction (FSI) problems. In spite of the advances made for their prediction, their complete computational characterization still constitutes a challenge and, as a consequence, experimental wind tunnel investigations remain an important tool for their study.

Test objects employed in aeroelastic experimental campaigns are normally instrumented with conventional devices like strain gauges, piezoelectric accelerometers, pressure probes and load cells. These measurement systems provide accurate and precise data for the characterization of both interfaces (flow and structure) of the FSI problem. Nevertheless, their employment supposes various strong limitations, among which the most relevant are their intrusiveness, the complexity of the experimental setup and their limited information density (pointwise measurements). The state-of-the-art optical quantitative flow measurement technique, known as Lagrangian Particle Tracking (LPT), has been recently proven capable of overcoming the drawbacks of the forenamed measurement systems, providing simultaneous structure and volumetric (3D3C) flowfield data in a non-intrusive way. In addition, its combination with novel flow tracers, Helium-Filled Soap Bubbles (HFSB), and more efficient particle tracking algorithms, Shake-The-Box (STB), has permitted the extension of the achievable measurement domain (in the order of cubic meters) at an affordable computational cost.

This thesis aims to evaluate the capabilities of such measurement techniques (LPT combined with STB algorithms and HFSB tracers) to determine the aerodynamic loads over large-scale flexible test objects during experimental aeroelastic investigations. Such analysis is performed by means of a wind tunnel campaign, carried out in the Open Jet Facility at TU Delft, that involves a highly-flexible wing, with a 100 mm chord and a 550 mm span, subjected to both steady and unsteady inflow conditions. The assessment of the aeroelastic phenomena is executed at a freestream velocity of $U_\infty \approx 18.3$ m/s, corresponding to a Reynolds number of $\mathrm{Re} \approx 1.25 \cdot 10^5$ based on the wing chord. The unsteady inflow conditions are defined through the actuation of a gust generator mounted at the outlet of the wind tunnel nozzle. Furthermore, a regular grid of circular reflective markers is distributed over the test object surface with the objective of characterizing its structural dynamics and improving the overall aeroelastic analysis.

Three different load determination methods are employed to retrieve the aerodynamic forces acting on the test object once the Lagrangian velocity data is transformed into Eulerian fields through ensemble averaging (binning) processes: On the one hand, the integral momentum conservation equation in its classical formulation. On the other hand, the integral momentum conservation equation with an alternative formulation that prevents the explicit use of the static pressure and any other quantity that cannot be directly obtained through LPT. Finally, the Kutta-Joukowski theorem, which relies on the obtainment of the circulation along a path enclosing the model. The measurements of a 6-axis force balance are taken as a reference to assess the accuracy and precision of these methods.

The results obtained through the implementation of these load determination techniques are presented following the specified structure: First, the sensitivity of each of the methods to various parameters like the spatio-temporal discretization of the velocity data, the location of the control volume boundaries or the concentration of tracing particles is assessed. Then, aerodynamic loads in test cases involving steady inflow conditions (*Static Cases*) are examined through the analysis of their spanwise distribution and by comparing their integral magnitude with reference load cell measurements. To conclude, a similar investigation is conducted with the gust encounter data (*Dynamic Cases*), where sectional and integral results are analyzed independently. These results are complemented with information on the structure dynamics, which is obtained through the tracking of surface markers, to assist in the description and characterization of the complete aeroelastic problem.

Contents

List of Figures

List of Tables

List of Symbols

Load determination methods

$(\cdot)'$	Sectional quantities	-
$(\cdot)_b$	Body quantities	-
$(\cdot)_S$	Surface quantities	-
$(\cdot)_w$	Wake quantities	-
$(\cdot)_\infty$	Freestream quantities	-
Γ	Circulation	m^2/s
γ	Vortex strength	m/s
$\overline{\mathbf{u}}$	Mean velocity vector	m/s
$\mathbf{F}$	Force vector	N
$\mathbf{n}$	Unit vector	-
$\mathbf{u}'$	Velocity fluctuation vector	m/s
$\mathbf{u}$	Velocity vector	m/s
$\mathbf{x}$	Position vector	m
$\mathcal{N}$	Dimensional constant	-
μ	Kinematic viscosity	$N \cdot s/m^2$
ω	Vorticity vector	1/s
ρ	Density	kg/m^3
τ	Viscous stress tensor	N/m^2
L	Lift force	N
p	Static pressure	Pa
t	Time	s
U	Velocity magnitude	m/s

PIV principles

$(\cdot)_f$	Fluid quantities	-
$(\cdot)_p$	Particle quantities	-
λ	Wavelength	m
$\mathbf{x}$	Displacement vector	m
μ	Kinematic viscosity	$N \cdot s/m^2$
ρ	Density	kg/m^3
τ	Relaxation time	s
C_s	Scattering cross section	m^2
d	Diameter	m
I_0	Incident light intensity	W/m^2
M	Magnification factor	-
P_s	Scattered power	W
t	Time	s
U	Velocity magnitude	m/s

Experimental setup

$(\cdot)_\infty$	Freestream quantities	-
α_0	Pitch angle	deg
β	Vane oscillation amplitude	deg
$\dot{N}$	Production rate	1/s
$\varnothing$	Diameter	-
A_{cross}	Cross sectional area	m^2
C	Concentration	$1/cm^3$
f	Frequency	Hz
$f_\#$	Focal ratio	-
k	Reduced frequency	-
n_{nozz}	Number of nozzles	-
Re	Reynolds number	-
U	Velocity magnitude	m/s

Data processing

$(\cdot)'$	Non-dimensional quantities	-
$(\cdot)_\infty$	Freestream quantities	-
$(\cdot)_B$	Interrogation window quantities	-
$(\cdot)_p$	Particle quantities	-
α_0	Pitch angle	deg

β	Sweep angle	deg
ω	Oscillation angular velocity	rad/s
ϕ	Phase lag	rad
θ	Twist angle	deg
φ	Dihedral angle	deg
A	Oscillation amplitude	m
d	Displacement	m
f	Frequency	Hz
l	Length	m
N	Number (count)	-
R	Radius	m
s	Wing span	m
T	Oscillation period	s
t	Time	s
U	Velocity magnitude	m/s
u_i	Velocity component	m/s
x_c	Relative chordwise position	-
y	Wing position	m
y_0	Equilibrium wing position	m
y_t	Relative thickness	-

Results

$(\cdot)'$	Non-dimensional quantities	-
$(\cdot)_\infty$	Freestream quantities	-
$(\cdot)_{BL}$	Boundary layer quantities	-
$(\cdot)_B$	Interrogation window quantities	-
$(\cdot)_{CV}$	Control Volume quantities	-
$(\cdot)_C$	Grid cell quantities	-
$(\cdot)_G$	Gust quantities	-
α_0	Geometric angle of attack	deg
α_G	Gust-induced angle of attack	deg
α_P	Plunge-induced angle of attack	deg
λ	Wavelength	m
σ	Noise level	-
τ	Time lag	s
c	Wing chord	m
c_l	Sectional lift coefficient	-
d	Distance	m
F	Aerodynamic force	N
k	Reduced frequency	-
l	Length	mm
M	Aerodynamic moment	N/m
T	Oscillation period	s
U	Velocity magnitude	m/s
u_i	Velocity component	m/s
f	Frequency	Hz
z	Spanwise coordinate	m

List of Acronyms

B.C. Boundary Conditions 6

CFD Computational Fluid Dynamics 3, 19
CVV Coaxial Volumetric Velocimetry 22

DES Detached Eddy Simulations 3
DMT Derivative-Moment Transformation 7, 8, 10
DOF Degree Of Freedom 60

EASA European Aviation Safety Agency 2
EPTV Ensemble Particle Tracking Velocimetry 19

FAA Federal Aviation Administration 2
FEM Finite Element Methods 3
FFT Fast Fourier Transform 59
FOV Field of View 15, 38, 40, 41, 71, 72
FSI Fluid-Structure Interaction v, 1–3, 5, 22–24, 47, 95–98
FVM Finite Volume Methods 3

GVT Ground Vibration Test 32

HFSB Helium-Filled Soap Bubbles v, 4, 13, 17, 21–23, 25, 27, 28, 35–38, 76, 95
HWA Hot Wire Anemometry 13

IPR Iterative Particle Reconstruction 18, 19, 38, 39

LCO Limit-Cycle Oscillations 3
LDV Laser Doppler Velocimetry 13
LES Large Eddy Simulations 3
LEV Leading Edge Vortex 21
LPT Lagrangian Particle Tracking v, 10, 11, 22, 23, 33, 35–38, 41, 42, 48, 63, 95, 97, 98

MART Multiplicative Algebraic Reconstruction Technique 15, 17

OJF Open Jet Facility v, 25–27, 31, 32, 95
OTF Optical Transfer Function 37, 38

PIV Particle Image Velocimetry 3–6, 8, 13–23, 25–29, 32, 33, 35–39, 47, 48, 58, 73, 77, 78, 95
PTU Programmable Time Unit 29
PTV Particle Tracking Velocimetry 18–20

RANS Reynolds-Averaged Navier-Stokes 3
RV Root Vortex 21

SMART Sequential Multiplicative Algebraic Reconstruction Technique 20
STB Shake-The-Box v, 4, 13, 18–23, 26, 29, 35–38
SV Scanning Vibrometer 20

TEV Trailing Edge Vortex 21
TV Tip Vortex 21

VSC Volume Self-Calibration 37, 38

1

Introduction

One of the greatest challenges that aviation faces nowadays is the reduction of pollutant emissions throughout the complete life-cycle of modern aircrafts. Among other organizations and institutions, the High Level Group on Aviation Research of the European Commission defined the mission and vision of the European Union for the aerospace industry in 2050 (Aviation Research 2011). Out of other objectives, the European Commission proposed a 75% reduction in CO_2 per passenger kilometre and a 90% reduction in NO_x emissions relative to the capabilities of typical new aircrafts at the beginning of the century.

Aside from other obvious improvements in powerplants and fuels, the employment of composite materials in modern airplanes, such as the Airbus 350 XWB shown in Figure 1.1, constitutes an appealing improvement towards the achievement of a sustainable aviation in the foreseeable future, as it permits the development and implementation of lightweight structures, thus reducing aircrafts fuel consumption and emissions. However, as a result of their increased flexibility, the use of these lightweight structures in slender bodies like aircraft wings might lead to challenging nonlinear Fluid-Structure Interaction (FSI) phenomena, which appear when fluid-immersed flexible bodies interact with their surroundings. For this reason, they need to be studied, considering all the contributors to the problem, in a discipline known as aeroelasticity.

Figure 1.1: A350 XWB, with more than a 54% of its structure made of composite materials[1].

[1] https://www.aerospace-technology.com/projects/a350wxb/

One of the most relevant strategies to classify aeroelastic events depending on the nature of their load generation mechanisms was proposed by Collar 1946. As seen in Figure 1.2, the contributors to these FSI phenomena were classified in three main groups, capable of describing most aeroelastic problems: aerodynamic forces that appear as surface pressure distributions over the test object due its interaction with the surrounding fluid; elastic forces and stresses directly related to the structural properties of bodies caused by geometric deformations; and inertial forces arising from body mass accelerations.

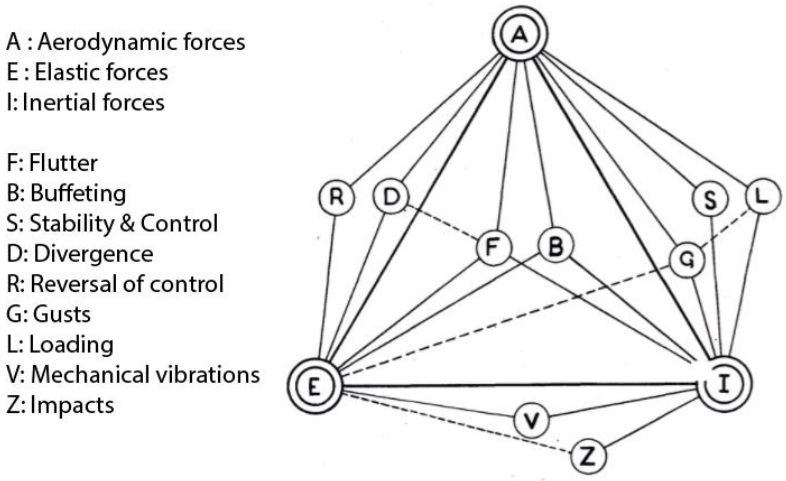

Figure 1.2: Triangle of forces. Reproduced from Collar 1946.

Collar's triangle shows these three contributors (forces) in its vertices and attributes to their interaction the appearance of different aeroelastic problems and phenomena. Such events do not have to involve all three sources (aerodynamic, elastic and inertial), but only some of them, to be considered as FSI problems: vibrations arise from structure solid mechanics (E+I); divergence appears as a consequence of the interaction of elastic and aerodynamic forces (E+A); and stability and control are only affected by inertial and aerodynamic phenomena (I+A). Nevertheless, some of the most challenging and interesting FSI problems; such as flutter, buffeting or gust encounters; occur when all three contributors take part (A+E+I). Among the forenamed aeroelastic events, static wing loading and gust encounters have been chosen as the test cases for the present experimental investigation.

Gusts are demonstrations of the atmospheric perturbations that aircrafts might encounter during their routine operation. These disturbances in the freestream velocity can take any direction, although the present research focuses on vertical gusts (perpendicular to the freestream velocity, Figure 1.3). As the appearance of such phenomena influences the control & stability capabilities of aircrafts and the loads to be withstand by them, they are currently incorporated in aircraft certification processes authored by aviation regulatory agencies like the Federal Aviation Administration (FAA) or the European Aviation Safety Agency (EASA).

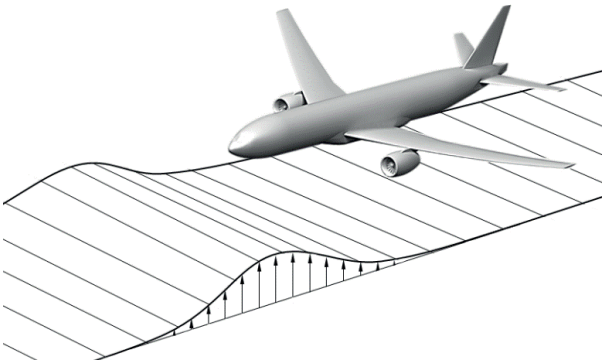

Figure 1.3: Illustration of a vertical gust hitting an aircraft in flight. Reproduced from Lancelot et al. 2017.

Three different approaches can be employed to analyze and characterize Fluid-Structure Interaction problems and assess their impact in aircraft performance throughout the certification processes: theoretical or analytical models, computational or numerical methods and experimental investigations.

Regarding analytical aeroelasticity models, they rely on theories of structure dynamics and aerodynamics that are normally limited by very restrictive hypotheses. Some of the most relevant aeroelasticity models (Theodorsen 1934 and Sears 1941) that were developed in the mid-nineteenth century considered important assumptions like 2D flows, linearized potential aerodynamics, thin airfoil theory or small perturbations theory. Nonetheless, these models were capable of describing and explaining fundamental effects of simple unsteady aeroelasticity problems like the time-shift between airfoil kinematics and generated aerodynamic forces as a consequence of the wake shedding downstream of the airfoil. Therefore, analytical models are restricted to basic problems and applications, although the findings obtained through their employment offer insightful information of the physical principles that govern them.

Such theoretical models are the basis of more complex and functional numerical methods that can be applied to world-alike problems to analyze both structure and fluid interfaces.

On the one hand, concerning aerodynamic computational solvers (Computational Fluid Dynamics), they are based on discretized formulations of the Navier-Stokes equations. The discretization of these fluid dynamics equations is generally conducted through Finite Volume Methods (FVM), which are easily adaptable to complex forms and geometries. In addition, most of these solvers (Reynolds-Averaged Navier-Stokes, Detached Eddy Simulations, Large Eddy Simulations...) involve relevant simplifications, mainly related to the treatment of flow turbulence. On the other hand, with respect to structural numerical methods, they are normally based on the linear and non-linear theories of elasticity, whose differential equations are discretized implementing Finite Element Methods (FEM). To characterize the coupled interactions of aerodynamic, elastic and inertial phenomena in aeroelastic problems, both CFD and FEM solvers are required.

During the last decade, great improvements in the available computational power have been achieved. These advancements have permitted the implementation of linear numerical tools in simplified aeroelastic problems like flutter and gust encounters. Nevertheless, the available processing power is still incapable of dealing with more realistic problems involving unsteady viscous flows (for which high-order flow models are required), more complex geometries or non-linear phenomena like Limit-Cycle Oscillations (LCO). As a consequence, experimental campaigns are still needed to identify events that cannot be observed through numerical simulations, to validate and verify results obtained with computational tools and to gain insight on the principles that govern complex FSI phenomena.

As described in Collar 1946 and shown in Figure 1.2, aeroelastic events result from the interaction of loads of different nature. For this reason, to properly represent FSI problems, both structural and flowfield measurements must be conducted. Initially, the most widely used measurement systems to characterize structural forces and accelerations in aeroelastic experimental campaigns were multi-axis balances (Dietz et al. 2003), strain gauges (Gkiolas et al. 2018) or accelerometers (Moulin et al. 2007). Similarly, pressure probes and transducers were first used as the main tool to determine both steady and unsteady aerodynamic loads on wind tunnel tests.

Nevertheless, these conventional measurement techniques do not meet certain requirements that guarantee an appropriate description of the complete aeroelastic problem, among which the most relevant are:

- Simultaneous measurement of flowfield and structural quantities.
- Non-intrusiveness of the measurement system to avoid alterations of the test case.
- Sufficient information density (whole-field techniques preferred).
- Reduced complexity of the system to guarantee its versatility.

Anyhow, the state-of-the-art technique for quantitative velocity flowfield measurements, known as Particle Image Velocimetry (PIV), has been recently proven to be capable of retrieving simultaneous information of both the structural and aerodynamic interfaces in aeroelastic experimental tests (Mitrotta et al. 2021), while

overcoming most of the aforementioned limitations of conventional measurement systems. Furthermore, various studies have shown the potential of PIV data to determine the aerodynamic forces acting on fluid-immersed bodies through different methods like the Kutta-Joukowski theorem (Anderson Jr 2017) or the evaluation of the integral momentum conservation equation on a control volume enclosing a body with various formulations (Unal et al. 1997 and Noca et al. 1999).

However, to the best of the authors knowledge, none of these studies has aimed to determine the aerodynamic loads on such a relevant aeroelastic problem as a gust encounter by a highly flexible wing employing volumetric (3C3D) measurements to account for 3D unsteady flow structures, together with up-to-date tracing particles (Helium-Filled Soap Bubbles), that permit large-scale measurements, and the innovative Lagrangian Particle Tracking algorithm known as Shake-The-Box (STB). This consideration motivates the research objective of the current masters thesis:

"Evaluate the capabilities of Lagrangian Particle Tracking to determine the aerodynamic loads acting on large-scale flexible bodies by means of the experimental investigation of a highly-flexible wing subjected to both steady and unsteady inflow conditions. "

In the following chapters of this thesis, a summary of the most relevant non-intrusive methods to determine aerodynamic loads from velocity data, together with a brief description of their main assumptions and limitations, will be presented (Chapter 2). Then, in Chapter 3, the working principles of Particle Image Velocimetry (PIV), along with innovative tracing particles (HFSB) and tracking algorithms (STB), will be described. In addition, various examples of the employment of PIV in aeroelastic experimental campaigns will be introduced. Chapter 3 will conclude with the definition of the main research objective and the formulation of its research questions. Eventually, the experimental procedures applied to accomplish the proposed research objective will be depicted in Chapter 4, followed by a brief description of the experiment test cases. Afterwards, in Chapter 5, the data processing strategies followed in the execution of this thesis will be presented, followed, in Chapter 6, by a discussion of the results reached through their implementation. Finally, a review of the most relevant conclusions, as well as some recommendations for future studies, will be provided in Chapter 7.

2

Non-intrusive load determination methods

As mentioned previously, aeroelastic wind tunnel campaigns should ideally employ non-intrusive measurement systems capable of evaluating structural and flow quantities simultaneously. Following these criteria, in order to identify the contribution of the flow interface to the FSI problem, non-intrusive aerodynamic load determination techniques are required. For this reason, a review of the most relevant non-intrusive methods to determine aerodynamic loads and moments acting over fluid-immersed bodies from velocity field data is in the author's interest. In this chapter, two of these methods will be provided: On the one hand, the evaluation of the integral momentum conservation equation inside a control volume and, on the other hand, the application of the Kutta-Joukowski theorem to velocity field data. The focus will be placed on the theoretical principles that govern these procedures, as well as on the assumptions taken in their implementation and their related limitations.

2.1. Integral momentum conservation

Newton's second law, which defines forces as the time rate change of linear momentum, can be applied to finite control volumes to obtain the forces experienced by the fluid inside them in terms of flowfield quantities like pressure, velocity or density (Anderson Jr 2017). Similarly, when control volumes enclose bodies, it is possible to define the force exerted by them on the surrounding fluid. So, taking into account Newton's third law, aerodynamic loads on immersed bodies, which are equal and opposite to these body-to-fluid forces, can be expressed as:

$$\mathbf{F}(t) = -\int_V \frac{\partial(\rho\mathbf{u})}{\partial t} dV - \int_S (\rho\mathbf{u}\cdot d\mathbf{S})\mathbf{u} - \int_S p d\mathbf{S} + \int_S \tau \cdot d\mathbf{S} \tag{2.1}$$

The employment of the integral momentum conservation equation in its classical form (Equation 2.1) implies the explicit evaluation of the pressure over the contours of the control volume. However, pressure is not a measurable quantity in PIV systems and additional processing steps are required. Oudheusden 2013 reviews different existent approaches to extract pressure fields from experimental planar-PIV data employing fluid mechanics governing equations: assuming incompressible flow conditions, the Navier-Stokes momentum equation can be used to infer pressure gradients from velocity and acceleration fields. Considering known fluid density and viscosity and neglecting body forces, the pressure gradient in an Eulerian reference frame can be expressed as:

$$\nabla p = -\rho\frac{\partial \mathbf{u}}{\partial t} - \rho(\mathbf{u}\cdot\nabla)\mathbf{u} + \mu\nabla^2\mathbf{u} \tag{2.2}$$

Alternatively, Poisson's pressure equation, which results from the evaluation of the divergence of the pressure gradient (Equation 2.2), can also be used to evaluate the pressure from velocity data:

$$\nabla^2 p = -\rho\nabla\cdot(\mathbf{u}\cdot\nabla)\mathbf{u} \tag{2.3}$$

Although both approaches are theoretically equivalent, their practical implementation differs substantially: the integration of the pressure gradient requires prescribed values of the pressure (Dirichlet B.C.) where it is imposed (origin of the numerical integration), while Poisson's pressure equation needs both prescribed pressure (Dirichlet B.C.), where it is imposed, and pressure gradients (Neumann B.C.) over the remaining control volume contours. In addition, the discretization of the terms of both equations results in an inconsistent propagation of the numerical error, thus in different sensitivities to the spatio-temporal resolution. The reader is referred to Oudheusden 2013, Liu et al. 2006 and Baur et al. 1999 to gain insight on different numerical implementation strategies, like the space-marching integration or the omni-directional integration, to evaluate the pressure field from both the pressure gradient and Poisson's equations.

Nevertheless, in order to reduce the error propagation due to the discrete application of the operators in Equation 2.2 and Equation 2.3, various studies; among which Kurtulus et al. 2006, Jardin et al. 2009 and Guissart et al. 2017 are the most appealing; proposed the division of the flowfield into inviscid irrotational steady regions, where Bernoulli's equation (Equation 2.4) could be applied, and viscous rotational zones, where pressure needed to be evaluated completely using the Navier-Stokes momentum equation.

$$p + \frac{1}{2}\rho U^2 = \text{constant} \tag{2.4}$$

Even in applications involving fully disturbed flow domains, which is the case in most PIV measurements due to the limited size of their field of view, an extended version of Bernoulli's equation (Equation 2.6), valid for irrotational inviscid advective flows with small mean velocity gradients, is assumed to be acceptable.

$$p + \frac{1}{2}\rho\left(\overline{\mathbf{u}}\cdot\overline{\mathbf{u}} + \mathbf{u}'\cdot\mathbf{u}'\right) = \text{constant} \tag{2.5}$$

Further modifications should be implemented to Equation 2.4 when unsteady flow regimes are considered. These modifications rely on the capability to describe irrotational velocity fields as gradients of velocity potentials ($\nabla\varphi$), thus permitting the derivation of Equation 2.5 from the momentum conservation Euler equation in constant density flows (Batchelor 1967):

$$\rho\frac{\partial\varphi}{\partial t} + p + \frac{1}{2}\rho U^2 = \text{constant} \tag{2.6}$$

In Kurtulus et al. 2006 three different pressure evaluation approaches were tested. First, the direct integration of the pressure gradient across the control volume contours was considered. Then, Bernoulli's equation was employed irrespectively of the rotational and viscous nature of the flow in certain regions of the domain. Finally, a division of the field of view was performed between regions where flow could be considered as quasi-steady, inviscid and irrotational and regions where this assumption could not be met, using Bernoulli's equation and the numerical integration of the pressure gradient respectively. In this study, the rotational region of the flow was considered to occupy the entire downstream boundary of the control volume.

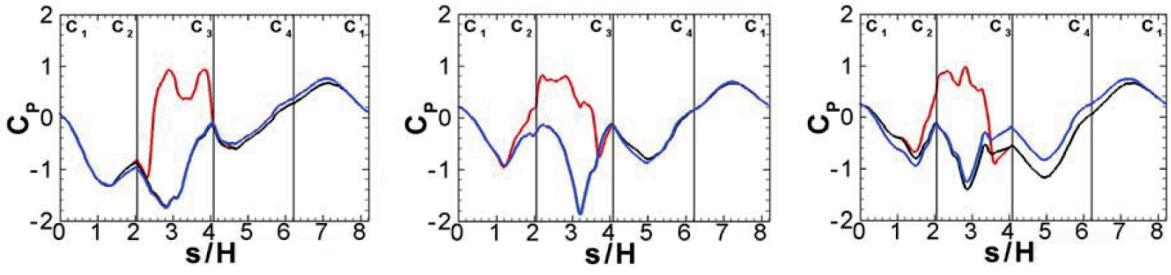

Figure 2.1: Pressure coefficients over rectangular contours. Bernoulli equation (red line); Mixed approach (black line); NS equations integration (blue line). Reproduced from Kurtulus et al. 2006.

As shown in Figure 2.1, Kurtulus et al. 2006 proved that Bernoulli's equation was inadequate within the body wake resulting in higher pressure levels, as total pressure losses due to viscous effects are not considered. Moreover, it was also demonstrated that the use of Bernoulli's equation in inviscid irrotational quasi-steady

regions was acceptable, as resultant pressure distributions were generally in good agreement with those obtained through the direct integration of the pressure gradient. Finally, the sensitivity of the pressure distribution to the presence of local measurement or numerical errors when computed solely through the integration of the pressure gradient was manifested, as certain deviations in the pressure outside the viscous region, that could only be caused by the numerical propagation of error in the space-marching integration process, were observed in some cases. So, due to its robustness with respect to local errors and its physical consistency within the viscous region, the use of the mixed approach was justified in Kurtulus et al. 2006.

Further steps towards the optimal division of the domain into viscous rotational and inviscid irrotational regions were taken in Jardin et al. 2009 and Guissart et al. 2017. Both articles proposed the use of flow quantities to determine the limits of the viscous region, thus improving the previous consideration of taking the entire downstream contour as a viscous rotational region and opening the door to the use of mixed approaches to obtain the static pressure over the entire flowfield. A non-dimensional vorticity threshold of 0.1, which led to an error reduction of 1% in the pressure term (Equation 2.1), was used in Jardin et al. 2009; while the Γ_2 function was used as the viscous region identifier in Guissart et al. 2017. In addition, this last article also compared the reconstructed pressure at the points where viscous and inviscid regions met (points B′ and C′ in Figure 2.2), linearly weighting the resultant error along the contour wake region (B′C′ segment).

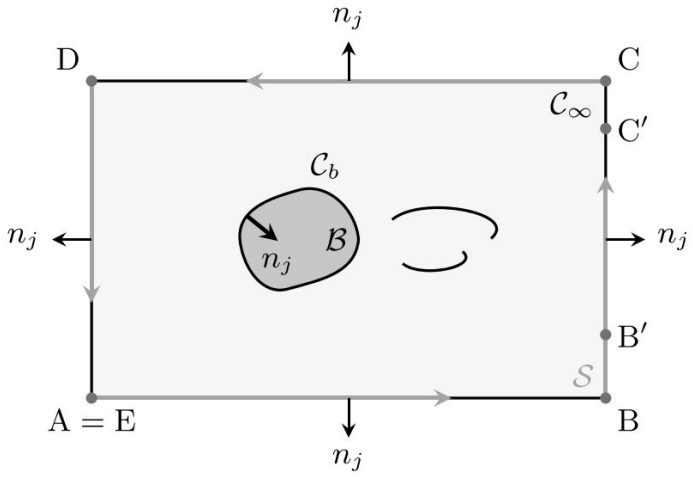

Figure 2.2: Schematic view of the control surface **S** and its contours $\mathbf{C}_\infty$ and $\mathbf{C_b}$ around the geometry **B** of interest. Reproduced from Guissart et al. 2017.

In this thesis, the pressure over the control volume boundaries, needed to implement the integral momentum conservation equation in its classical form (Equation 2.1), is explicitly evaluated following the approach proposed in the aforementioned studies: Bernoulli's equation in its extended form (Equation 2.6) is employed over all the control volume boundaries except for the viscous rotational region at the downstream contour, where the pressure gradient is integrated. In addition, as done in Guissart et al. 2017, a linear weighting over the wake region is applied to account for the error of the pressure at the viscous-inviscid interface. The viscous-rotational segment (wake) at the downstream control volume contour is identified using a vorticity threshold equal to $0.3 \cdot \omega_{max}$.

On the other hand, as seen in Equation 2.1, the unsteady term in the integral momentum conservation equation involves the evaluation of volume integrals, which requires the employment of flowfield data across the entire control volume. However, for large-scale applications, it is still very difficult to obtain clean data close to the surface of the body. Consequently, a technique solely based on the surface integration over the control volume external boundaries, away from the body surface, is highly recommended. Nevertheless, flow steadiness is a severe limitation that does not hold in most aerodynamic applications. For this reason, a transformation of the unsteady term in its volume formulation to an equivalent surface integral formulation is required. This transformation of the volume integral, known as the Derivative-Moment Transformation (DMT), was performed by J. Z. Wu et al. 2005.

$$\int_V \mathbf{u} dV = -\int_V \mathbf{x}(\nabla\cdot\mathbf{u})dV + \int_{\partial V}\mathbf{x}(\mathbf{u}\cdot\mathbf{n})dS = -\int_V \mathbf{x}(\nabla\cdot\mathbf{u})dV + \int_S \mathbf{x}(\mathbf{u}\cdot\mathbf{n})dS + \int_{S_b}\mathbf{x}(\mathbf{u_b}\cdot\mathbf{n_b})dS_b \tag{2.7}$$

The DMT, when applied to incompressible (divergence-free $\nabla\cdot\mathbf{u}=0$) flows and thin bodies, leads to a formulation of the unsteady term in Equation 2.1 equal to:

$$\int_V \mathbf{u} dV = \int_S \mathbf{x}(\mathbf{u}\cdot\mathbf{n})dS \tag{2.8}$$

In this thesis, the unsteady term of the integral momentum conservation equation will be evaluated employing its Derivative-Moment Transformation (Equation 2.8), considering the test model as a thin body and assuming incompressible flow conditions ($M<0.3$).

2.1.1. Vorticity - Noca formulation

In order to avoid the specific use of the static pressure over the control volume boundaries, preventing its indirect derivation from velocity data, an alternative formulation of the integral momentum conservation equation, only dependent on the velocity field and its temporal and spatial derivatives, was proposed by several studies, among which Noca et al. 1999 was the most relevant.

$$\mathbf{F} = -\frac{1}{\mathcal{N}-1}\frac{\mathrm{d}}{\mathrm{d}t}\int_{V_\infty(t)}\mathbf{x}\wedge\omega \mathrm{d}V + \frac{1}{\mathcal{N}-1}\frac{\mathrm{d}}{\mathrm{d}t}\oint_{S_b(t)}\mathbf{x}\wedge(\mathbf{n}\wedge\mathbf{u})\mathrm{d}S - \oint_{S_b(t)}\mathbf{n}\cdot(\mathbf{u}-\mathbf{u}_S)\mathbf{u}\mathrm{d}S \tag{2.9}$$

The alternative formulation of the integral momentum conservation equation provided by Noca et al. 1999 was derived from the original "impulse equation over infinite domains" (Equation 2.9) presented in Batchelor 1967, generalized for viscous flows involving solid bodies in J. C. Wu 1981 and evaluated on field applications in Lighthill 1996. However, Equation 2.9 required the whole vorticity field to be known and a null net circulation in 2D spaces, which for most experimental studies supposes a major restriction as the field of view of quantitative flowfield measurement systems like PIV is limited. For this reason, Noca et al. 1999 extended the applicability of Equation 2.9 to any test case, even those where the vorticity was not confined in finite regions, by accounting for the convection of the vorticity away from the control volume.

Among the three different formulations proposed in Noca et al. 1999 (impulse, momentum and flux), the most appealing is the "flux equation" (Equation 2.10), as it is expressed solely in terms of surface integrals and flow quantities at the control volume contours (DMT by J. Z. Wu et al. 2005), thus avoiding the use of data close to the body surface.

$$\mathbf{F} = \oint_{S(t)}\mathbf{n}\cdot\gamma_{\text{flux}}\mathrm{d}S - \oint_{S_b(t)}\mathbf{n}\cdot(\mathbf{u}-\mathbf{u}_S)\mathbf{u}\mathrm{d}S - \frac{\mathrm{d}}{\mathrm{d}t}\oint_{S_b(t)}\mathbf{n}\cdot(\mathbf{ux})\mathrm{d}S \tag{2.10}$$

Where,

$$\gamma_{\text{flux}} = \frac{1}{2}u^2\mathbf{I} - \mathbf{uu} - \frac{1}{\mathcal{N}-1}\mathbf{u}(\mathbf{x}\wedge\omega) + \frac{1}{N-1}\omega(\mathbf{x}\wedge\mathbf{u}) -$$
$$-\frac{1}{\mathcal{N}-1}\left[\left(\mathbf{x}\cdot\frac{\partial\mathbf{u}}{\partial t}\right)\mathrm{I} - \mathbf{x}\frac{\partial\mathbf{u}}{\partial t} + (N-1)\frac{\partial\mathbf{u}}{\partial t}\mathbf{x}\right] + \frac{1}{\mathcal{N}-1}[\mathbf{x}\cdot(\nabla\cdot\tau)\mathbf{I} - \mathbf{x}(\nabla\cdot\tau)] + \tau$$

In this thesis, the "flux equation" (Equation 2.10) is employed as an alternative to the classical formulation of the integral momentum conservation equation. As no suction nor blow of the boundary layer is included in the test model and the wing employed in the experimental campaign is assumed to behave as a thin body, the second and third terms in Equation 2.10 are neglected.

During the present experimental investigation, the viscous terms in Equation 2.1 and Equation 2.10 are neglected. This measure is taken in order to prevent the inclusion of undesired noise in the reconstructed loads,

since the weight of the viscous terms in the overall aerodynamic forces obtained through momentum conservation methods is very small when the distance of the control volume boundaries to the body surface is large enough. The relative contribution of the viscous terms to the aerodynamic forces has already been analyzed in previous studies such as David et al. 2009, Jardin et al. 2009 and Mohebbian et al. 2012, which concluded that their effect on the overall forces was minor (about 0.2% of the total lift force).

2.2. Kutta-Joukowski theorem

Aside from the obtainment of aerodynamic forces through the evaluation of the integral momentum conservation in control volumes enclosing bodies, the Kutta-Joukowski theorem entails an alternative to retrieve lift forces acting on fluid immersed bodies in steady incompressible inviscid flows. This theorem states that the lift force per unit span in two-dimensional bodies is directly proportional to the body bound circulation:

$$L' = \rho_\infty V_\infty \Gamma \tag{2.11}$$

Where Γ corresponds to the finite bound circulation, defined as the line integral of the velocity around a closed curve enclosing the body:

$$\Gamma = -\int_S (\nabla \times \mathbf{V}) \cdot \mathbf{dS} = -\oint_C \mathbf{V} \cdot \mathbf{ds}$$

However, in unsteady applications, Equation 2.11 does not consider the influence of the flow acceleration and quasi-steady lift forces resulting from its application. Nevertheless, assuming unsteady potential flow around thin airfoils, the overall circulation can be attributed to the addition of the airfoil bound vortex strength (γ_b) and the vorticity shed in the airfoil wake (γ_w). This shed vorticity arises from the time rate change of the airfoil bound vortex strength, following Kelvin's theorem (Anderson Jr 2017, chapter 4). The bound vortex strength (γ_b) relates to the bound circulation (Γ_b) as:

$$\Gamma_b(t) = \int_0^c \gamma_b(x,t)\mathrm{d}x$$

while the time rate change of the bound circulation in thin airfoil applications is directly proportional to the shed vorticity, which is convected at freestream velocity forming a planar wake:

$$-\frac{\partial \Gamma_b(t)}{\partial t} = U_\infty \gamma_w(c,t)$$

As a result, the unsteady lift force in incompressible inviscid flows involving thin airfoils can be expressed as:

$$L'(t) = \rho U_\infty \Gamma_b(t) + \rho \int_0^c \frac{\partial}{\partial t}\Gamma_b(x,t)dx \tag{2.12}$$

In this thesis, both the original Kutta-Joukowski theorem (Equation 2.11) and its alternative formulation for unsteady applications involving thin bodies (Equation 2.12) will be employed to evaluate the lift force of the flexible model. Even if the hypothesis under which the theorem is established (2D steady inviscid incompressible flows) were not met completely, previous studies like Sharma et al. 2012 have shown that results are still in good agreement with validation data.

2.3. Summary

To conclude this chapter, a brief summary of the forenamed non-intrusive load determination techniques will be provided in this section, pointing out their main advantages and drawbacks and covering aspects such as their most relevant assumptions, their theoretical applicability or their expected sensitivity to measurement and numerical errors.

Integral momentum conservation - Classical formulation (Unal)

The most relevant aspects to point out from the integral momentum conservation equation in its classical formulation are:

- Theoretically, the integral momentum conservation equation in its classical formulation can be applied to any flow regime, as it is the integral formulation of the Navier-Stokes momentum equation and no assumptions or simplifications are taken in the process.
- Need of a control volume enclosing the body under study.
- Requires the explicit determination of the pressure over the boundaries of the control volume, which is not directly measurable with LPT.
- Unsteady terms involve the evaluation of volume integrals, which require the employment of velocity data close to the body surface affected by measurement errors and aberrations. Such volume integrals can be transformed into surface integrals (DMT) in divergence-free flows (incompressible; $\nabla \cdot \mathbf{u} = 0$) and thin body applications. By doing so, aerodynamic loads would be exclusively dependent on control volume boundary quantities.
- Involves the evaluation of spatial gradients in the pressure determination procedures and in the viscous term (Equation 2.1). These derivatives might amplify the influence of numerical measurement errors, thus affecting the resultant aerodynamic force.

Integral momentum conservation - Vorticity formulation (Noca)

The most relevant aspects to point out from the integral momentum conservation equation in its alternative vorticity formulation are:

- Theoretically, the vorticity formulation of the integral momentum conservation equation can be applied to any flow regime, as it is directly derived from the Navier-Stokes momentum equation and no assumptions or simplifications are taken in the process.
- Need of a control volume enclosing the body under study.
- Only requires quantities that can be directly measured with LPT measurement systems or that are directly obtained from spatial and temporal gradients of them.
- Unsteady terms involve the evaluation of volume integrals, which require the employment of velocity data close to the body surface affected by measurement errors and aberrations. Such volume integrals can be transformed into surface integrals (DMT) in divergence-free flows (incompressible; $\nabla \cdot \mathbf{u} = 0$) and thin body applications. By doing so, aerodynamic loads would be exclusively dependent on control volume boundary quantities.
- Involves the evaluation of spatial gradients in almost all terms taking part in the determination of aerodynamic forces (Equation 2.10).

Kutta-Joukowski theorem

The most relevant aspects to point out from the Kutta-Joukowski theorem are:

- Theoretically, the applicability of the Kutta-Joukowski theorem is limited to certain flow regimes, as it is derived under the assumptions of steady, incompressible and irrotational flows. Nevertheless, some studies like Sharma et al. 2012 have obtained results in good agreement with reference data in separated and unsteady flow regimes.
- Limited to 2D flows.
- It is not capable of obtaining integral body forces, only sectional forces.
- Need of a closed path enclosing the body section under study.
- Its unsteady formulation assumes unsteady potential flow around airfoils and thin airfoil theory is employed for its derivation.

- Only requires quantities that can be directly measured with LPT measurement systems or that are directly obtained from spatial and temporal gradients of them.
- It does not require spatial derivation of LPT quantities (velocity). For this reason, it is less susceptible to be influenced by numerical measurement errors than the Navier-Stokes momentum equation methods mentioned previously.

3

PIV principles and Research Objective

As presented in Chapter 2, there exist several non-intrusive methods capable of retrieving aerodynamic loads in fluid immersed bodies from velocity field data. However, to meet the requirements of ideal measurement systems for experimental aeroelastic tests proposed in Chapter 1, the employed velocity data must be obtained following the same criteria. The state-of-the-art technique for whole-field quantitative velocity measurements, known as Particle Image Velocimetry (PIV), has proven to be an attractive alternative to conventional velocity measurement systems (e.g. pressure probes, Hot Wire Anemometry (HWA) or Laser Doppler Velocimetry (LDV)) due to its limited intrusiveness, its capability to deliver high-density information with acceptable spatio-temporal resolution and its versatility. In addition, very recent studies, like Mitrotta et al. 2021, have shown its potential to perform simultaneous readings of structural and flow quantities. For this reason, and as stated previously, the goal of this thesis is to assess the capability to infer the aerodynamic loads on such a relevant aeroelastic problem as a highly-flexible wing encountering steady and unsteady inflow conditions employing volumetric PIV measurements exclusively.

In this chapter, a brief overview of the working principles of PIV will be provided. In addition, the role of alternative flow tracers (Helium-Filled Soap Bubbles (HFSB)) in the feasibility of large-scale volumetric PIV measurements will be explained. Furthermore, the fundamentals of the state-of-the-art Lagrangian Particle Tracking algorithm (Shake-The-Box), together with its impact in the determination of velocity fields in experimental campaigns, will be presented. Finally, some examples of previous studies involving the determination of aerodynamic loads from PIV velocity data will be given.

3.1. Working principles of Particle Image Velocimetry

During Particle Image Velocimetry (PIV) measurements, fluid is seeded with particles that are used as flow tracers. These particles require certain mechanical and scattering properties that permit a proper tracing of the flow and a sufficient light scatter. To conduct the measurements, the region of interest in the flowfield is illuminated with a light sheet that is normally generated by a pulsed laser and shaped with various lenses and mirrors. In this way, when flow tracers cross the region of interest, the light sheet illuminates the particles and the scattered light can be recorded by the imaging optics (usually digital cameras). In addition, in order to be capable of reconstructing the velocity field, particles must be illuminated and recorded at least twice within a short time interval Δt.

Each pair of images, obtained from consecutive light pulses, is then divided into small regions or windows where mean displacement vectors $\mathbf{x} = [\Delta x, \Delta y]$ of the particles contained in every window are defined. These displacement vectors are obtained by applying statistical cross-correlation operations to equivalent windows belonging to consecutive light pulses (t and $t+\Delta t$). Finally, and taking into account the imaging magnification factor (M), the instantaneous velocity components in each window can be easily computed (Equation 3.1) and combined to obtain the velocity field.

$$u_i = \frac{\Delta x_i}{M \cdot \Delta t} \tag{3.1}$$

However, the PIV setup shown in Figure 3.1 and the aforementioned working principles only permit the reconstruction of in-plane velocity components in two-dimensional domains (2D2C), missing useful information such as the out-of-plane velocity component or the out-of-plane velocity gradients. So, if the flow were three-dimensional, the out-of-plane velocity component would become a source of error, being this error greater as the distance to the axis of the recording system increases (Raffel et al. 2018).

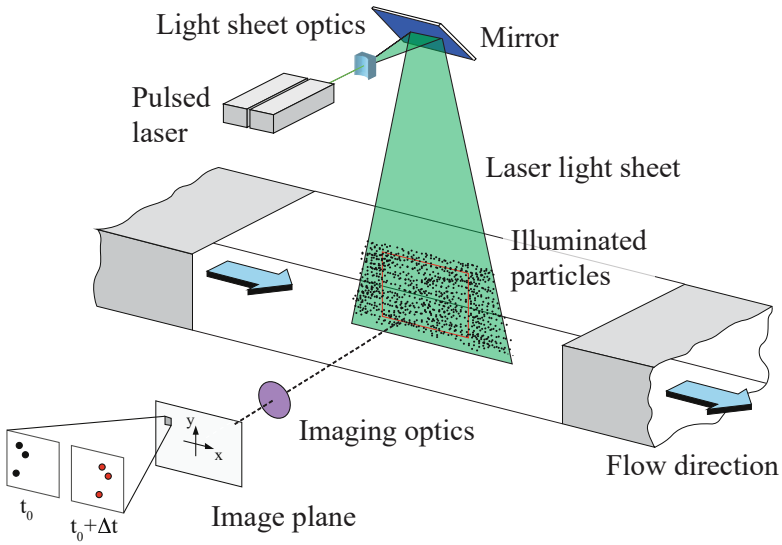

Figure 3.1: Planar PIV setup schematic. Reproduced from Raffel et al. 2018.

In order to remedy the limitations of planar-PIV, a second optical imaging system (camera) was introduced in the experimental setup by Arroyo et al. 1991. This second camera permitted the determination of the out-of-plane velocity component through the application of stereoscopic methods to the recorded images: although both recorded velocity fields were different, the reconstructed velocity field from both images was unique and the discrepancies between the original velocity fields could only be attributed to the out-of-plane velocity component. Nevertheless, even after all velocity components in a planar domain (2D3C) were measurable, the velocity field was not completely captured, as the out-of-plane gradients could not be measured yet. For this reason, after stereo-PIV was developed, research efforts were pointed towards the determination of the out-of-plane gradients from volumetric measurements to obtain a complete characterization of the velocity field. Initially, some studies like Kähler et al. 2000 or Mullin et al. 2005 proposed dual-plane stereoscopic PIV measurements, which consisted in conventional stereo-PIV systems moving along certain directions, to determine the out-of-plane gradients in given planar positions. However, although this approach allowed a better understanding of the flowfield, it was still very limited in the characterization of phenomena of greater dimensions.

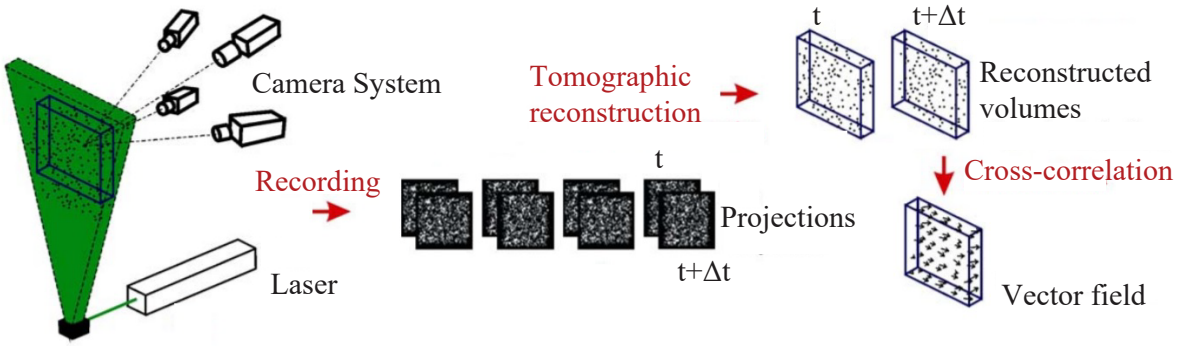

Figure 3.2: Working principle of tomographic PIV. Reproduced from Elsinga et al. 2006.

Both the limitation in the measured velocity component of planar-PIV and the dimensional limitations of stereo-PIV were overcome with the appearance of tomographic PIV (Elsinga et al. 2006), which permitted the complete characterization (3C3D) of unsteady coherent flow structures. This new PIV technique included at least a third imaging optic system (camera) and a volumetric region where flow tracers were pulsed-illuminated and recorded (Figure 3.2). The 3D displacement vectors were obtained from 3D particle distributions by means of a volumetric cross-correlation algorithm, known as Multiplicative Algebraic Reconstruction Technique (MART). Thanks to its ability to reconstruct instantaneous three-dimensional velocity fields, tomographic PIV was employed in various studies involving unsteady and turbulent flow phenomena like Scarano et al. 2010, where flow structures in the near region of jets of different outlet geometries were investigated; or Scarano et al. 2009, which studied cylinder wakes, both shown in Figure 3.3.

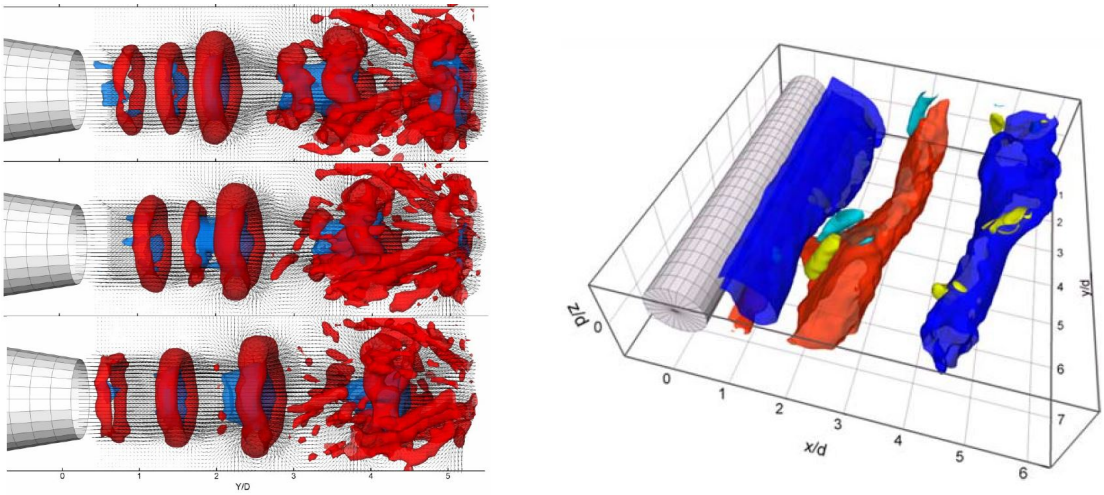

(a) Circular jet vorticity and axial velocity iso-surfaces. Reproduced from Scarano et al. 2010.

(b) Cylinder wake vorticity iso-surfaces. Reproduced from Scarano et al. 2009.

Figure 3.3: Experimental tomographic PIV studies.

However, the thickness of the Field of View in conventional tomographic PIV measurements was limited by two factors: light intensity (energy density) being inversely proportional to the thickness of expanded light beams and restrictive in-focus imaging demands that required small optical apertures (high $f_{\#}$), thus reducing the captured light intensity. For this reason, only small measurement volumes could be achieved with typical tomographic PIV setups, as seen in Table 3.1 where typical sizes of volumetric field of views in tomographic PIV experiments are shown (Scarano 2013).

	Pulse energy [mJ]	**Thickness [mm]**	**Volume [cm^3]**
Low-rep rate, air	200	4 to 12	20 to 50
Low-rep rate, water	200	10 to 40	100 to 200
High-speed (3 kHz) air	10	4 to 8	10 to 20
High-speed (1 kHz) water	50	10 to 20	20 to 50

Table 3.1: Typical measurement volume in tomographic PIV experiments. Reproduced from Scarano 2013

3.2. Large-scale measurements

The complete characterization of velocity flowfields (3D3C) in experimental flow measurement campaigns was a long-term objective that was finally achieved with the development of tomographic PIV methods. Nevertheless, the applicability of this new technique was still limited to small volumes. In this section, an overview of the main developments that permitted the implementation of tomographic PIV measurements in large-scale cases will be presented.

3.2.1. Helium-Filled Soap Bubbles

As mentioned before, tomographic PIV measurement volumes are mainly limited by the scattered light of flow tracers. This light intensity depends both on the pulse energy of the light source, which during the last decades has remained unaltered, and the scattering efficiency of the tracing particles. For this reason, efforts were pointed towards the development of alternative flow tracers with greater scattering efficiency. This property of tracing particles is normally quantified by means of the scattering cross-section (C_s), which is defined as the ratio between the scattered power (P_s) and the intensity (I_0) of the incident light (Raffel et al. 2018). As seen in Figure 3.4, the scattering cross-section is directly proportional to the diameter of the particles (d_p), the light wavelength (λ) and the ratio between the refractive index of the tracers and the fluid around them (Melling 1997). For this reason, considering exclusively the scattering requirements and taking into account that both the light wavelength and the refractive index ratio are normally fixed, the desirable diameter of particle tracers is the greatest possible.

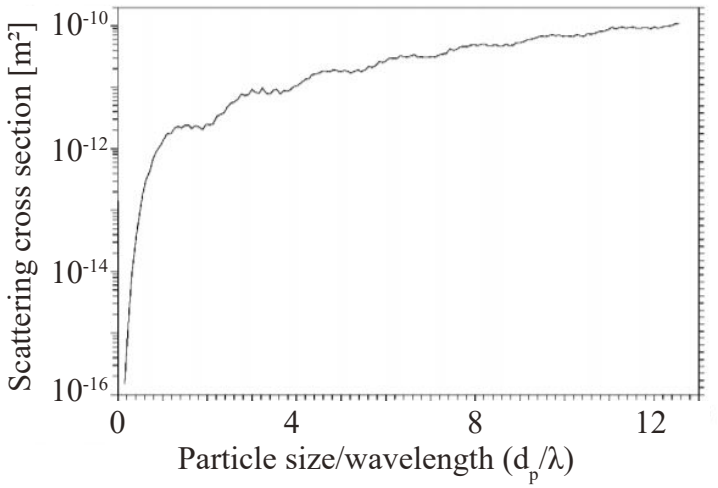

Figure 3.4: Scattering cross-section Vs. particle size (refractive index $m = 1.6$). Reproduced from Melling 1997.

Nevertheless, tracing particles must meet certain mechanical requisites to ensure a proper characterization of the flowfield under study. These mechanical properties are related to the capability of tracers to match the flow behaviour, resulting in small discrepancies between their velocity and the velocity of the fluid surrounding them (slip velocity or velocity lag). Among all the terms that affect the dynamics of small spherical particles like flow tracers (added mass force, non-inertial force, Basset force...), the quasi-steady viscous term, also known as Stokes' drag, is the most dominant (Raffel et al. 2018). So, neglecting other contributions, the slip velocity of accelerated tracing particles can be expressed as:

$$U_s = U_p - U = d_p^2 \frac{(\rho_p - \rho_f)}{18\mu} \frac{\mathrm{d}U}{\mathrm{d}t}, \tag{3.2}$$

Where U_p corresponds to the particle velocity, U is the flow velocity, ρ_f and ρ_p are the fluid density and particles density respectively and μ is the fluid viscosity.

Alternatively, the capability of flow tracers to adapt their velocity to flowfield changes can also be estimated by their relaxation time (τ_p), which consists of the ratio between the velocity lag and the flow acceleration (Raffel et al. 2018).

$$\tau_p = d_p^2 \frac{(\rho_p - \rho_f)}{18\mu} \tag{3.3}$$

Taking both quantities under consideration and analyzing the parameters that define them, it is easily observable that mechanical requirements of flow tracers in PIV measurements are governed by two main factors, whose minimization is desired: On the one hand, the buoyancy of tracing particles, defined as the difference

between particles and flow densities $\left(\rho_p - \rho_f\right)$; and, on the other hand, the diameter of flow tracers, as seen in Figure 3.5. However, neutral buoyancy in conventional flow tracers like oil droplets or metal oxide powders (TiO_2 or Al_2O_3) is only achievable in liquid flows, being the diameter of the particles (d_p) the determinant quantity in the velocity lag for gas flows. This situation led to a conflict of interests between the scattering and mechanical properties of tracing particles in gas flows and required a compromise between both, resulting in flow tracers with diameters between $0.5\mu m$ and $50\mu m$ (Raffel et al. 2018).

Nonetheless, Helium-Filled Soap Bubbles (HFSB), introduced in PIV measurements by Bosbach et al. 2009, appeared as an alternative to conventional flow tracers for large-scale PIV measurements, as they were capable of maintaining appropriate mechanical properties with greater particle diameters ($200\mu m$ to $300\mu m$) thanks to their neutral buoyancy. Soon after, the use of HFSB in wind tunnel experimental campaigns was tested by Scarano et al. 2015 and Caridi et al. 2016, where particle relaxation times between $10\mu s$ and $30\mu s$ were obtained, thus showing that HFSB were suitable for low-speed large-scale PIV measurements conducted in wind tunnels.

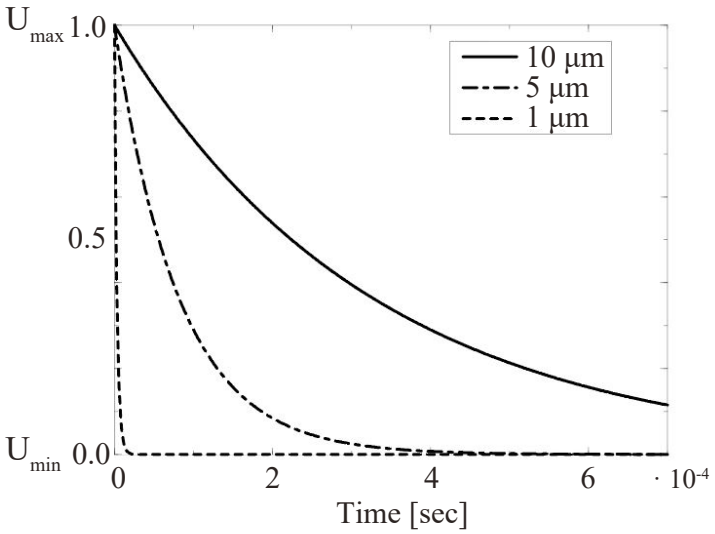

Figure 3.5: Relaxation time of oil particles in decelerating air flows. Reproduced from Raffel et al. 2018.

Given the dimensions of the test model, which will be later presented in Chapter 4, and the interest of obtaining not only sectional but also integral forces, these innovative Helium-Filled Soap Bubbles are chosen in this thesis as the flow tracers for the PIV measurements in the aeroelastic experimental investigation.

3.3. Lagrangian Particle Tracking

As previously mentioned, tomographic PIV obtains the distribution of flow tracing particles from their projections on two-dimensional images acquired with multiple imaging systems (cameras). Through different algorithms like MART, these tracers are reproduced as intensity distribution in three-dimensional interrogation volumes (voxels) that discretize the field of view. Then, 3D cross-correlations are employed in image pairs from consecutive light pulses to obtain volumetric velocity fields.

Although tomo-PIV permits high particle image densities (0.05 particles per pixel), the technique involves certain limitations: the appearance of ambiguities, known as ghost particles, alter the resultant vectorial velocity field. The influence of these ghost particles is intensified for higher particles densities. In addition, the working principles of tomo-PIV reconstruction algorithms include the evaluation of spatial averages over the voxels, thus flattening the spatial gradients and dissipating the finest flow structures. Furthermore, the representation of the position of the particles with volumetric interrogation windows involves inevitable positioning errors, in the order of 0.15-0.2 pixels for zero-noise synthetic data (Wieneke 2013), that affect the reconstructed flowfield. Finally, cross-correlation based methods like tomo-PIV involve other general drawbacks like the high computational time and the memory requirements to perform the velocity field reconstructions.

The downsides of tomo-PIV exhibit the interest in obtaining knowledge of individual particles in space and time to permit the evaluation of the acceleration and the velocity of every flow tracer in the measurement domain. By doing so, the spatial averaging over volumetric interrogation windows would be avoided and the spatial resolution of the reconstructed flowfield would be conveniently increased. Traditionally, particles were positioned in each camera-plane through the application of 2D-Gaussian intensity fits, triangulating the resultant planar distributions of each camera and obtaining 3D particle arrangements, which tracked in space and time lead to the desired Lagrangian particle trajectories (3D PTV Nishino et al. 1989). Nevertheless, these particle positioning techniques were only feasible for low particle image densities (around 0.005 particles), as greater tracer densities resulted in an overlap of particle images that generated unacceptable proportions of ghost particles that altered the accuracy of the method (Cierpka et al. 2013).

For this reason, alternative Lagrangian particle tracking methods that alleviated the particle image density restrictions of conventional 3D-PTV were developed. An appealing alternative, known as Iterative Particle Reconstruction (IPR), was proposed by Wieneke 2013. IPR proceed as conventional 3D-PTV in its first steps: 2D particle distributions are triangulated in the three-dimensional space to reconstruct volumetric particle distributions. However, in this alternative particle tracking technique, the resultant particle arrangements are projected back to the planar domain and compared to the original camera images, adjusting both the position and intensity of the particles to match the original measurements. The forenamed procedure is repeated until the local residuals are minimized and the 3D particle disposition converges to the final solution. The number of iterations can be increased to improve the accuracy of the technique at the expense of computational effort. However, although some of the main drawbacks of tomo-PIV (position accuracy and spatial resolution) and conventional 3D-PTV (low image particle density requirements) were overcome with IPR, the problem with ghost particles could not be solved for high tracer concentrations.

To overcome the limitations of Iterative Particle Reconstruction and other Lagrangian particle tracking techniques, an alternative algorithm, which is the state-of-the-art method for particle tracking in aerodynamic imaging measurements, was developed by Schanz et al. 2016. This algorithm is known as Shake-The-Box (STB).

3.3.1. Shake-The-Box

While the previous tracking methods treated every time instant and its corresponding measurements individually, STB employs both spatial and temporal information. In Shake-The-Box, the temporal information is used to predict the position of the particles in the successive time-steps by extrapolating known particle paths. This leads to a robust particle tracking technique valid for high particle image densities that discard almost all ghost particles. Compared to other tracking algorithms, STB inverts the conventional tracking process: tracks are determined prior to the reconstruction of the particle distribution by using accessible flowfield information to guess the particle disposal.

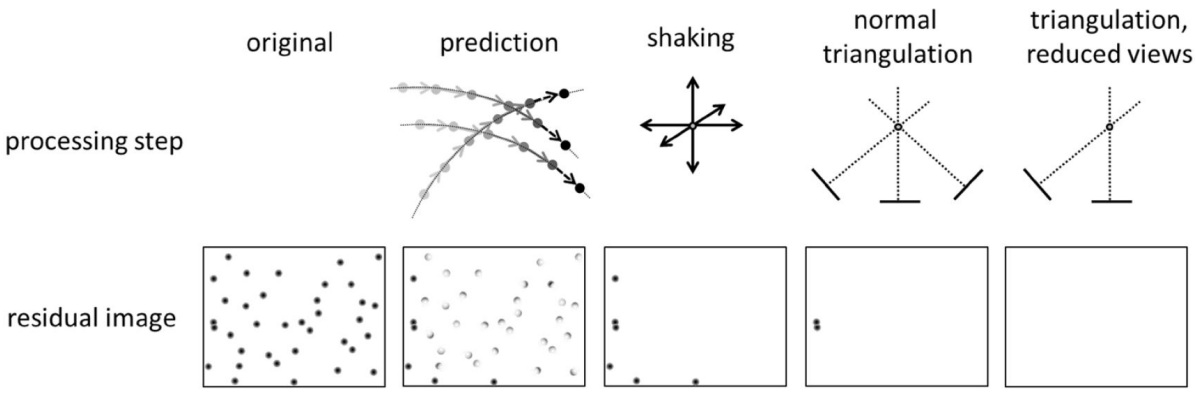

Figure 3.6: Schematic description of the Shake-The-Box procedure for one time-step in the converged state. Reproduced from Schanz et al. 2016.

Two main assumptions were considered in the development of the algorithm, as stated in Schanz et al. 2016:

- Particles within the measurement volume do not disappear.
- Knowledge of particle trajectories permits accurate estimations of their position in the next time-step.

The application of the Shake-The-Box tracking algorithm can be divided into three stages or phases:

1. **Initialization Phase:** No previous information about the particle tracks is available at the first time-steps of the measurement. For this reason, an alternative approach must be used to detect a sufficient number of tracks to move to the convergence phase. Two procedures can be employed to identify these initial tracks:
   - Direct identification of particles position by means of IPR or traditional 3D-PTV algorithms. These *candidate particles* are tracked across the initial time-steps, typically $n_{Init} = 4$ (Schanz et al. 2016). The untracked particles are discarded and considered as ghost particles.
   - Employment of predictors at the first time-steps of the measurement. These predictors can be defined by means of tomo-PIV reconstruction of the initial time-steps, information from previous measurements or CFD data.
2. **Convergence Phase:** Once the particles corresponding to the first n_{Init} time-steps have been properly tracked, they are used to guess the particles position in the successive time-steps implementing Wiener filters (Wiener 1949). Nevertheless, the particles position at t_{n+1} reconstructed from the particle tracks in t_n will not be fully coincident with the actual position of the particles. For this reason, the predicted particles are "shaken" following different methods ("Normal" or "Initial" shake) and compared to their actual location iteratively until the image local residuals are minimized. In addition, ghost particles need to be discarded and particles entering the field of view must be detected in this phase of the tracking algorithm. A schematic of the procedures described and employed in the converged state is shown in Figure 3.6.
3. **Converged Phase:** In the last phase of the algorithm, the number of tracked particles is maintained almost unvaried. The ending tracks in this phase correspond to tracers leaving the field of view. New particle tracks coincide with particles entering the measurement volume.

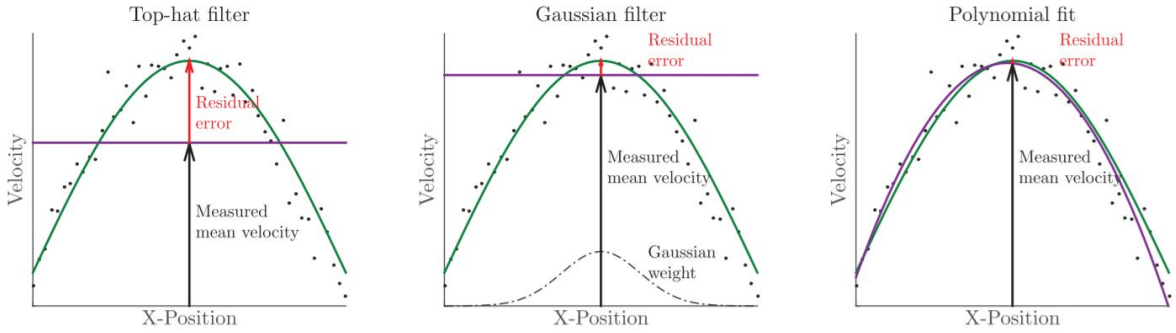

Figure 3.7: Sources of error due to residual velocity gradient within an interrogation spot. Reproduced from Agüera et al. 2016.

Although the reconstruction of Lagrangian particle tracks through the application of the Shake-The-Box tracking algorithm supposes a considerable improvement in terms of spatial resolution, positioning of particles, removal of ghost particles and mitigation of the computational cost; the identification of coherent and meaningful flow structures and the evaluation of flow statistics requires the interpolation of these discrete tracks data onto Eulerian grids. A method to retrieve Eulerian flowfield information from Lagrangian tracks, known as Ensemble Particle Tracking Velocimetry (EPTV), was developed by Agüera et al. 2016. This method divides the entire measurement volume into discrete spherical interrogation volumes where local flow statistics are derived from discrete velocity vectors of particles contained inside them. Different methods to compute these velocity statistics can be used, from top-hat filter to more complex polynomial fits of the velocity vectors in the interrogation volume.

3.3.2. Shake-The-Box Vs Tomographic PIV

The quality of velocity fields reconstructed by means of the Shake-The-Box algorithm was assessed in Schanz et al. 2016 by comparing the flowfields resulting from the application of both STB and tomographic PIV methods to time-resolved data of a transitional jet in a water tank. As seen in Figure 3.8, tomo-PIV (SMART) results show a more irregular radial distribution of the largest flow structures in the jet, together with a reduced number of the smallest flow structures. These improvements in the STB results are caused by various factors, among which the increased position accuracy, the removal of ghost particles and the avoidance of spatial filtering and velocity gradients smoothing are the most relevant.

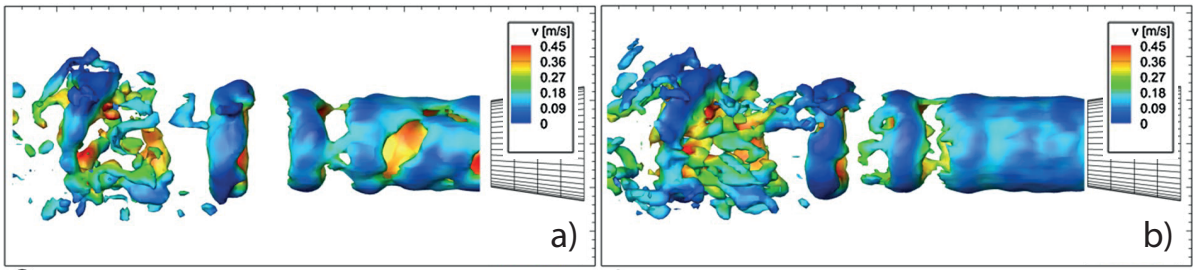

Figure 3.8: **a:** Isosurfaces of vorticity (= 175/s), obtained with Tomo-PIV processing; **b:** results from STB and grid interpolation at the same spatial resolution. Reproduced from Schanz et al. 2016.

3.3.3. Shake-The-Box for structure markers tracking

Shake-The-Box algorithm, whose procedures are described in Section 3.3.1, has been proven to effectively determine the tracks (position in space and time) of structure markers in very recent studies like Mitrotta et al. 2021, where robotic volumetric Particle Tracking Velocimetry (PTV) was employed to obtain simultaneous structural and flow measurements of a flexible flat plate encountering controlled gusts. However, the differences in the shape of the surface markers and the flow tracers (2D circles and 3D spheres respectively), result in increased positional uncertainties, which are proportional to the distance to the measurement probes and their orientation with respect to the markers' normal direction (Schneiders et al. 2018 and Mitrotta et al. 2021). Nevertheless, such uncertainties in the instantaneous position of surface tracers can be diminished through track regularization techniques (Savitzky et al. 1964). These procedures, whose results can be seen in Figure 3.9, consist in the implementation of sliding regressions of polynomials (at least second-order).

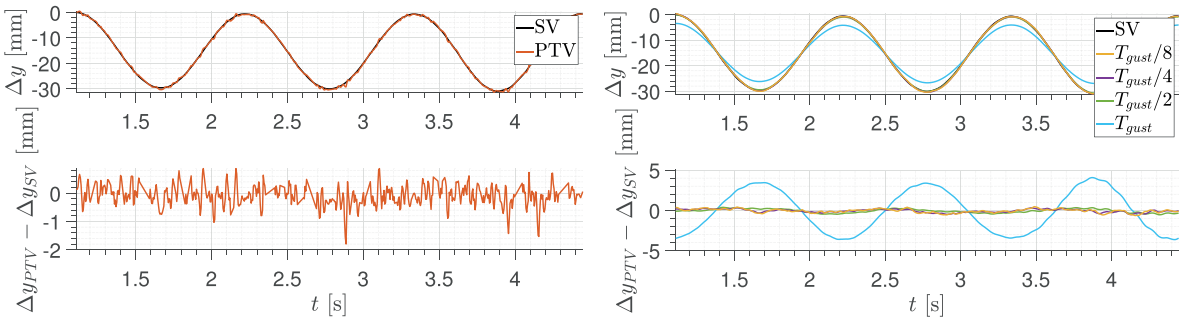

(a) No filtering.

(b) Savitzky-Golay filtering.

Figure 3.9: Time history of the instantaneous displacement measured by robotic volumetric PTV and SV (top) and of the related error (bottom) in non-filtered (left) and filtered (right) data. Reproduced from Mitrotta et al. 2021

PTV measurements were found to be in good agreement with the reference harmonic signal described by the Scanning Vibrometer (SV) measurements in Mitrotta et al. 2021, as seen in Figure 3.9a. The bias error (ϵ_b) and the random error (ϵ_r) of the PTV measurements with respect to the SV results were $\epsilon_b \approx -0.09$ mm and $\epsilon_b \approx 0.38$ mm, corresponding to 0.3% and 1.3% of the average displacement amplitude respectively. Similar results were found for filtered (Savitzky-Golay filter) marker displacement results, as appreciated in Figure 3.9b. For

kernels of 1/4 of the gust period, random errors resulted in $\epsilon_b \approx -0.10$ mm and $\epsilon_b \approx 0.20$ mm, respectively 0.3% and 0.7% of the average displacement amplitude. These results (Mitrotta et al. 2021) showed the feasibility of STB algorithms to obtain precise and accurate structural measurements in dynamic objects, while retrieving velocity field measurements from flow tracing particles and bubbles.

3.4. Non-intrusive load determination methods applied to PIV data

Various techniques described in Chapter 2 have been applied to PIV velocity data in recent studies showing its potential to determine aerodynamic loads in experimental campaigns. Initially, planar-PIV data was employed to study sectional forces in either steady (Unal et al. 1997, Noca et al. 1999 and Oudheusden et al. 2008) or moving (David et al. 2009, Villegas et al. 2013, Gharali et al. 2014, Ferreira et al. 2011, Sterenborg et al. 2014) test objects. Soon after, a step forward was taken to account for the effects of the out-of-plane velocity component in the loads, by employing stereo-PIV measurements (Ragni et al. 2011 and Tronchin et al. 2013). However, the dimensional limitations of both planar and stereoscopic Particle Image Velocimetry were not overcome until volumetric quantitative flowfield measurements (3C3D) were employed to fully characterize the velocity field from where the aerodynamic loads were derived.

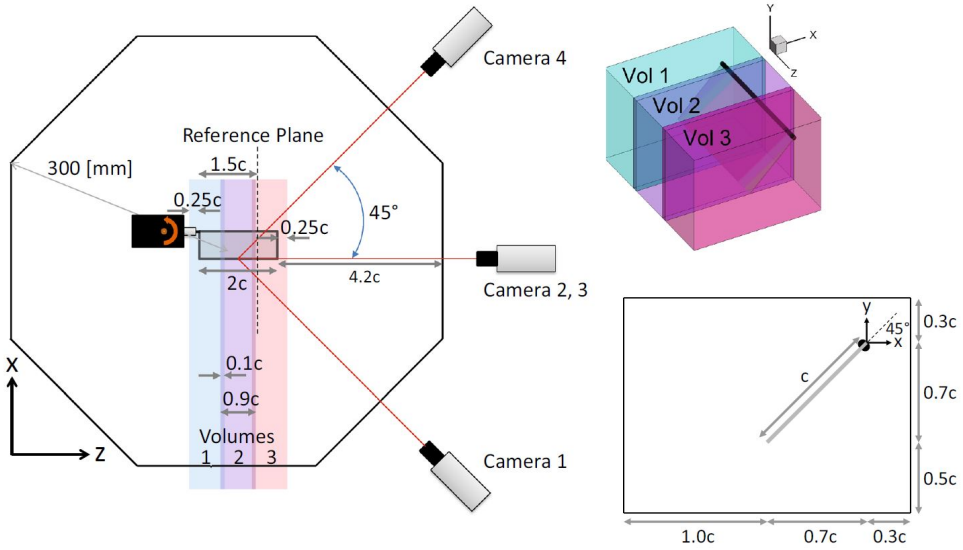

Figure 3.10: Experimental setup (*Left*), measurement volumes (*Right-top*) and field of view (*Right-bottom*). Reproduced from Meerendonk et al. 2018.

Tomographic PIV measurements were employed in Meerendonk et al. 2018 to characterize the 3D velocity field around a low-aspect-ratio flexible revolving wing. The integral momentum conservation equation in its classical form (Equation 2.1) was employed to derive the aerodynamic loads acting on the test model at three spanwise locations from the resultant velocity data. The use of tomo-PIV was motivated by the unsteady and three-dimensional nature of the resultant flow structures, as well as to analyze the correlation between the temporal evolution of fluid-dynamic forces and flow vortical structures. An illustration of the experimental setup employed in the study, together with the location of the measurement volumes and the chordwise field of view, is presented in Figure 3.10.

The use of tomo-PIV proved to be fundamental for the achievement of the research objectives. The effect of the wing flexibility in the resultant lift and drag forces was determined. A relation between the location of the most relevant flow structures (Leading Edge Vortex (LEV), Trailing Edge Vortex (TEV), Tip Vortex (TV) and Root Vortex (RV)) and the variation of sectional forces was established. Finally, the connection between the evolution of the spanwise pressure gradient and the development of the LEV was identified.

Similarly, 3C3D velocity data was used in Mertens et al. 2021b to determine the aerodynamic loads on a pitching airfoil model at its midspan plane. Nevertheless, contrary to previous studies, HFSB tracing particles and STB tracking algorithms were employed to conduct the PIV measurements, thus permitting greater mea-

surement volumes and improving the accuracy of the reconstructed velocity field. The load determination methods chosen for the study were the Kutta-Joukowski theorem and an alternative surface pressure reconstruction technique, which will not be considered in the present thesis. Although the employed methods were adapted from unsteady potential flow and thin airfoil theories, the resultant loads were in good agreement with the reference measurements for both methods, as seen in Figure 3.11. However, although 3D3C velocity measurements were employed, this study developed a two-dimensional analysis of the aerodynamic problem in a single sectional plane (midspan plane), thus not taking advantage of all the available flowfield information. On the other hand, a deeper analysis of the problem was performed in this research by measuring the airfoil surface position, as it was also done in Mitrotta et al. 2021. This surface reconstruction was done employing the same system that was used for the flowfield measurements (PIV), thus proving the capability of Particle Image Velocimetry, combined with Lagrangian Particle Tracking (LPT) algorithms, to fulfill all the requirements of ideal aeroelastic measurement systems defined in Chapter 1.

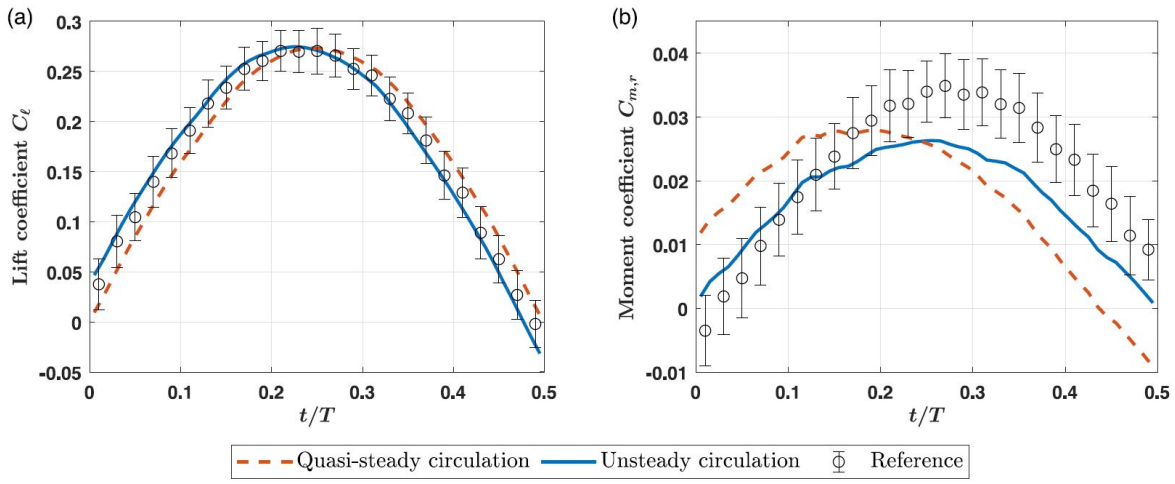

Figure 3.11: Aerodynamic coefficient for the pitching airfoil with fixed flap, (a) lift, (b) moment around the pitch axis. Reproduced from Mertens et al. 2021b.

A step forward was taken in Rojas 2020 by implementing the Kutta-Joukowski theorem to determine the spanwise lift force distribution in a flexible wing from 3C3D velocity data. As it was done in Mertens et al. 2021b, the PIV measurements were performed employing HFSB as flow tracers, thus permitting larger measurement volumes, and STB tracking algorithms. In addition, this study also investigated the dynamics of the flexible wing under various inflow conditions by tracking reflective markers distributed over the surface of the test model. Once again, the combination of 3C3D PIV measurements and LPT algorithms proved to be a feasible alternative to conventional aeroelastic measurement systems capable of performing simultaneous readings of structural and flow quantities, while minimizing the intrusiveness of the sensors and providing whole-field information with acceptable spatio-temporal resolutions. Nevertheless, the procedures employed in Rojas 2020 involved several limitations, among which the most relevant were: the limitation of the freestream velocity and the Reynolds number by the PIV setup (Coaxial Volumetric Velocimetry), the uncertain applicability of the Kutta-Joukowski theorem in test cases comprising significant unsteady viscous flow phenomena and the difficulties to characterize the complete aeroelastic phenomena with limited sectional information, as the entire test object could not be measured.

3.5. Research objective

A review of the most relevant literature has revealed that most aeroelastic experimental campaigns, used to validate and verify numerical FSI simulations, employ conventional sensors (strain gauges, accelerometers, pressure transducers, load cells...) that carry considerable limitations. However, alternative optical measurement techniques, such as PIV, have proven to be attractive tools to overcome these drawbacks. Among others, the most relevant improvements that Particle Image Velocimetry incorporates with respect to classic aeroelastic measurement systems are its limited intrusiveness, its capability to provide high density (whole-field) information with acceptable spatio-temporal resolution and its ability to perform simultaneous measure-

ments of both flow and structural quantities. As described in previous sections, various studies have aimed to determine aerodynamic loads and moments in fluid-immersed bodies by implementing non-intrusive load determination methods to experimental PIV velocity data. However, to the best of the author's knowledge, none of these studies has employed volumetric measurements in large-scale wind tunnel experiments to account for the effects of three-dimensional flow phenomena in the derived forces.

This thesis proposes the use of data obtained through the whole-field quantitative velocity measurement technique of Lagrangian Particle Tracking (LPT), together with Helium-Filled Soap Bubbles tracing particles and Shake-The-Box tracking algorithms, to analyze the capabilities of different non-intrusive load determination techniques to determine the aerodynamic loads on test models in aeroelastic experimental campaigns. The proposal of the thesis is evaluated in such a relevant FSI problem as a highly-flexible wing encountering different freestream conditions. Therefore, the research objective of the thesis can be formulated as:

"Evaluate the capabilities of Lagrangian Particle Tracking to determine the aerodynamic loads acting on large-scale flexible bodies by means of the experimental investigation of a highly-flexible wing subjected to both steady and unsteady inflow conditions."

The achievement of the proposed research objective is contingent upon the answer to several research questions and the achievement of secondary goals. The foremost research question of this thesis reads:

"How feasible and accurate is the use of Lagrangian Particle Tracking (LPT) algorithms for determining aerodynamic loads in large-scale experimental aeroelastic investigations involving highly-flexible wings?"

In order to answer this question unequivocally, various quantifiable features have to be taken into account. Firstly, the sensitivity of the non-intrusive load determination methods under study to various parameters of the measured data like its spatio-temporal resolution, its noise or the shape and size of the measurement field of view must be evaluated. These considerations lead to the first group of secondary questions with regard to the feasibility of non-intrusive load determination methods to determine aerodynamic loads from PIV data:

- *What is the sensitivity of the proposed load determination methods to the spatial resolution of the measured velocity fields?*
- *What is the sensitivity of the proposed load determination methods to the temporal resolution of the measured velocity fields?*
- *What is the sensitivity of the proposed load determination methods to the presence of random noise in the data?*
- *What is the sensitivity of the proposed load determination methods to the shape and size of the integration path/control volume?*

Secondly, once the sensitivity of each of the methods to different variables has been assessed, it is necessary to study their applicability and accuracy in various flow regimes and conditions. This investigation leads to the answering of the second subset of questions that contribute to the resolution of the main research question:

- *What is the accuracy of the proposed load determination methods under steady linear aerodynamics conditions?*
- *What is the accuracy of the proposed load determination methods under steady non-linear aerodynamics conditions?*
- *What is the accuracy of the proposed load determination methods in quasi-steady* $(0 < k < 0.05)$ *aerodynamics conditions?*
- *What is the accuracy of the proposed load determination methods in unsteady* $(k > 0.05)$ *aerodynamics conditions?*

The research objective is achieved through the answer to the main research question and its derived subquestions. These questions are clarified by means of a wind tunnel experimental campaign. In such test, both the desired inflow conditions (steady and unsteady) and the wing attitude are established with the target of defining the appropriate environment to answer the proposed questions. Tomographic Particle Image

Velocimetry is employed to capture the velocity field surrounding the flexible wing from where its aerodynamic forces are computed. By doing so, this Master's thesis aims to obtain unexampled conclusions about the capabilities of each of the proposed non-intrusive load determination methods in large-scale FSI experiments involving highly-flexible structures undergoing large deformations.

4

Experimental Setup and Procedures

A wind tunnel experimental campaign is conducted to answer the enumerated research questions in the fulfillment of the proposed research objective. In this chapter, a detailed explanation of all the features involved in the wind tunnel investigation will be provided. Moreover, a summary of the data acquisition strategies employed in the measurement of the structural and flow quantities of interest will be given. Finally, a brief description of the analyzed test cases, together with their motivation, will be performed.

4.1. Wind tunnel

The investigation is performed in the Open Jet Facility (OJF) at the Delft University of Technology. The OJF is an open test section closed return wind tunnel with an octagonal outlet of 2.85 x 2.85 m^2 and a 3:1 contraction ratio. It is powered by a 500 kW electrical engine which drives a turbine able to supply air speeds up to 35 m/s. The nominal turbulence intensity 1 m away from the tunnel nozzle outlet is 0.5% (Lignarolo 2016), although greater values were expected in the present study due to the presence of the HFSB seeding rake and the gust generator, as reported in Giaquinta et al. 2019. A schematic of the wind tunnel facilities is given in Figure 4.1.

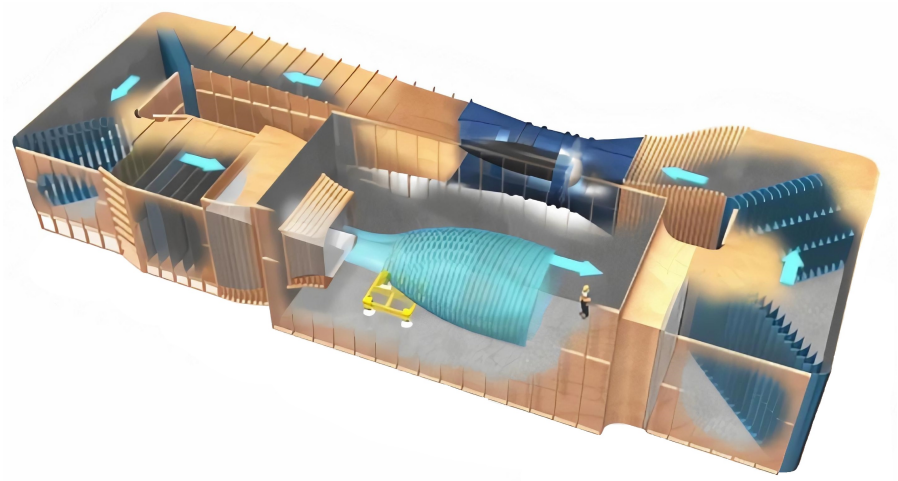

Figure 4.1: Schematic of the Open Jet Facility at the TU Delft [2].

The choice of the OJF to carry out the experimental campaign is motivated by the size of the test object and the space occupied by the equipment involved in the obtainment of the measurements (HFSB seeder, gust generator, PIV optical sensors, etc.), being the Open Jet Facility the only wind tunnel in the university capable of accommodating all of them.

[2] https://www.tudelft.nl/lr/organisatie/afdelingen/aerodynamics-wind-energy-flight-performance-and-propulsion/facilities/low-speed-wind-tunnels/open-jet-facility

4.2. Gust generator

In order to generate the unsteady inflow conditions in form of controlled gust profiles (cross-flow velocity component) at the open test section of the OJF, a gust generator, specifically developed by Lancelot et al. 2017 to adapt to the requirements of the Open Jet Facility, is mounted at the outlet of its settling chamber.

The gust generator is composed of an aluminium frame, rigidly fixed to the ground of the open test section, that holds the rest of the system components (vanes, actuators and control systems). Moreover, two vertically mounted foam wings, with a constant NACA 0014 airfoil section of 0.3 m chord length, occupy the entire height of the nozzle outlet (h = 2.88m). A set of electromechanical actuators, connected to the base of the vanes and controlled with a LabView user interface, provide the required motion of the gust wings to generate the desired velocity profile. The employed gust generator is able to provide both discrete and continuous gusts with frequencies between 0.5 and 10 Hz and vane oscillation amplitudes up to 10°.

4.3. Test object

The experimental investigation requires the test object to react with large deformations when subjected to unsteady inflow conditions within the wind tunnel operational speed range. For this reason, the model employed is a highly flexible wing, similar to the aeroelastic benchmark model design described in Avin et al. 2021, capable of sustaining tip bending displacements of more than 50% of its span.

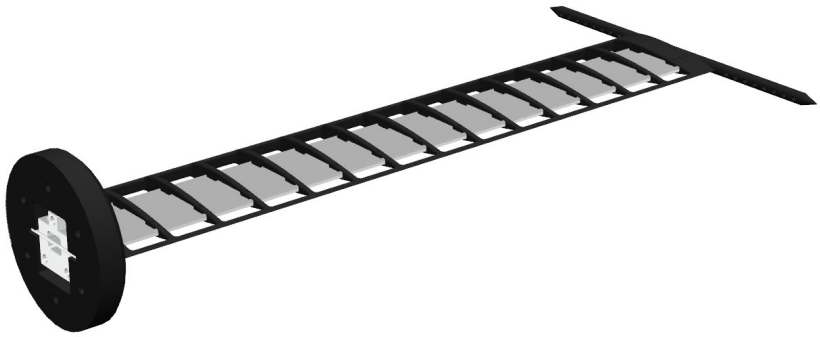

Figure 4.2: Test model structure: Nylon skeleton (black) and aluminium spar (silver).

The unswept wing presents a constant NACA 0018 airfoil section with a 100 mm chord and a 550 mm span. Its primary structure, which is shown in Figure 4.2, consists of a 3D printed Nylon 12 chassis. An Aluminium 7075 spar of 570 mm span, 60 mm width and 1.5 mm thickness is bonded to the nylon chassis employing LOCTITE 495 adhesive. The spar material has a density of 2810 kg/m^3 and a Young Modulus of 71.7 GPa. The wing skeleton is covered by a black self-adhesive Oralight Polyester coating foil with a grammage of 36 g/m^2. A ∅10 mm, 300 mm long rod is located at the model wingtip. A ∅120 mm, 22 mm tall solid cylinder is included at the bottom of the test object to permit its clamping. The model is attached to the force balance with six countersunk M6 bolts. The weight of the test object without the bottom clamping cylinder being considered is 0.321 kg.

Furthermore, a secondary objective of the research is the reconstruction of the wing deformed shape with the same PIV setup employed for the flowfield measurements. These structural measurements are performed by imaging and tracking reflective markers distributed over the wing surface in space and time. The model is first spray-painted with a matte black color to minimize the undesired surface light reflections. Then, white circular markers with a diameter of 1.5 ± 0.2 mm are imprinted on the wing surface employing a white color spray. The markers are distributed using a laser cut mask with a predefined regular pattern over each of the ribs of the wing. The markers are spaced by 30 mm and 38.25 mm in the chordwise and spanwise directions respectively. The size, shape and location of the surface reflective markers are chosen based on the experience of previous experiments (Mitrotta et al. 2021 and Rojas 2020). These parameters are chosen to guarantee an appropriate trade-off between marker detectability and pixel saturation and to permit their tracking with flow tracers tracking algorithms (STB). A reconstruction of distribution of the markers over the test object, together with its most relevant dimensions, is shown in Figure 4.3.

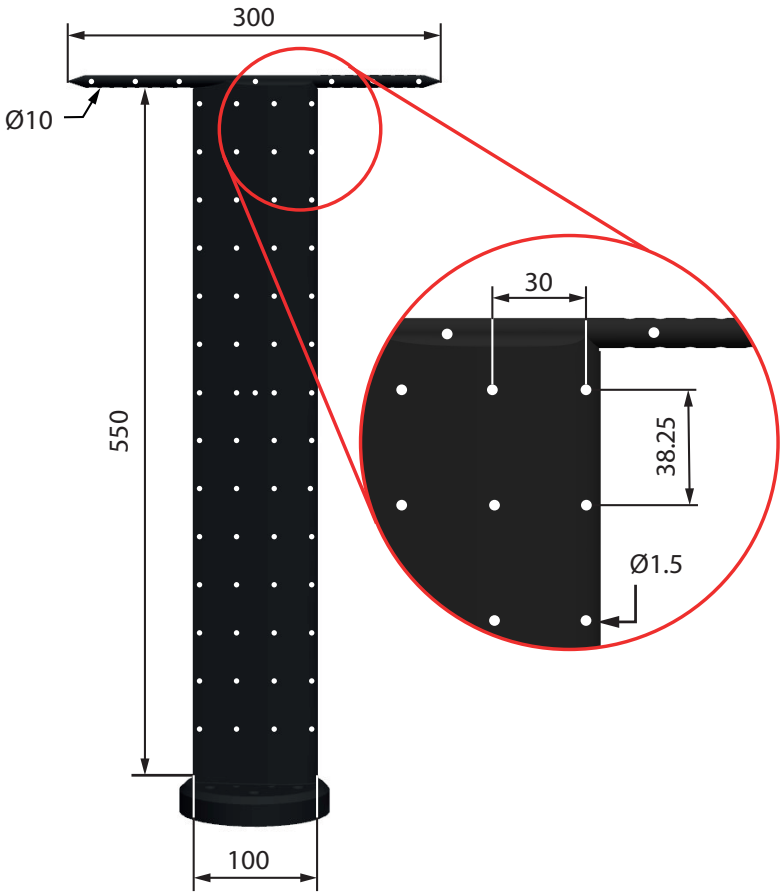

Figure 4.3: Surface reflective markers grid over the test model with some of its most relevant dimensions in millimeters.

4.4. PIV system

Conducting Particle Image Velocimetry measurements is one of the most important aspects of this thesis. The different components employed in the acquisition of the velocity field by means of this non-intrusive measurement technique will be presented in this section.

4.4.1. Seeding setup

Due to the large-scale of the experimental investigation, Helium-Filled Soap Bubbles are chosen as the flow tracers to be used in the PIV measurements of this thesis. These particles are generated and seeded in the test section of the wind tunnel through a seeding system developed by TU Delft Aerospace Faculty. The seeding rake is composed of 200 nozzles equally distributed along 10 vertical symmetric wings. Each nozzle has a production rate of $3{\cdot}10^4$ bubble $\cdot\, s^{-1}$ (Caridi et al. 2016). The resultant seeding cross-section is 500 x 1000 mm^2.

The seeding rake Figure 4.4a is positioned inside the settling chamber of the OJF to minimize the turbulence intensity increase due to its presence, which is estimated to be around 1% (Giaquinta et al. 2019), and to achieve an increment in the particle concentration at the open test section after the stream tube is contracted through the nozzle. As described in Caridi et al. 2016, the resultant seeding concentration at the test section in this experimental investigation is estimated to be:

$$C = \frac{\rho \cdot \dot{N} \cdot n_{\text{nozzles}}}{A_{cross} \cdot U_\infty} = \frac{3 \cdot 3 \cdot 10^4 \cdot 200}{0.5 \cdot 18.3} \approx 2 \cdot 10^6 \text{m}^{-3} \approx 2 \text{cm}^{-3}$$

Where $n_{nozzles}$ is the total number of nozzles in the seeding rake; A_{cross} is the seeding cross-section and ρ is the nozzle contraction ratio.

(a) HFSB seeding rake.

(b) HFSB LaVision Fluid Supply Unit [3].

Figure 4.4: Helium-Filled Soap Bubbles seeding system.

A *LaVision* HFSB generator (Figure 4.4b) is employed to produce the tracing particles while controlling the parameters involved in the process by modifying the pressure at each of their compartments.

4.4.2. Illumination source

The HFSB were illuminated with three stacked *LaVision LED-Flashlight 300* modules (Figure 4.5). Each illumination module is composed by 72 white high-power LEDs that can generate light pulses with operational frequencies between 0 and 20 kHz. The combined illumination area is 300 x 300 mm^2, with an opening angle of $10° \pm 5°$. This area corresponds to $-1 < x/c < 1$ in the chordwise (x) direction and half wing span in the spanwise (z) direction. The depth of the illumination volume (working distance) goes from 0.5 m to 2 m from the light source. The resultant measurement volume was approximately 22.5 litres (300 x 300 x 250 mm).

Figure 4.5: LaVision LED-Flashlight 300 [4].

4.4.3. Optical sensors

Three high-speed *LaVision Photron Fastcam SA1.1* cameras (Figure 4.6) are used to capture the tracing particles around the flexible wing and the surface reflective markers. The maximum sensor size of the cameras is dependent on the image sampling rate of the system. In this experimental investigation, a sensor size of 1024 x 1024 px is chosen, which results in an acquisition frequency of 5.4 kHz. This configuration is maintained through all the PIV measurements. A ∅50 mm objective is attached to each of the cameras and a $f_\# = 22$ is chosen to focus the desired field of view. The resultant focal depth is 500 mm approximately.

[3] https://www.lavision.de/en/applications/fluid-mechanics/piv-system-components/seeding-devices/
[4] https://www.lavision.de/en/applications/materials-testing/system-components/illumination/

Figure 4.6: LaVision Photron Fastcam SA1.1 camera [5].

4.4.4. Data acquisition system

The Particle Image Velocimetry measurement setup is completed with a data acquisition computer that includes the commercial software *LaVision DaVis 10.1.0.5* that implements the control strategies. A Programmable Time Unit (PTU), shown in Figure 4.7, with a 0.05 ns jitter, is employed to trigger the illumination source (LEDs) and the imaging sensors (high-speed cameras). The PTU is equipped with external trigger signal receptors, which have been used in this experimental campaign to synchronize the PIV system with the gust generator. The *LaVision DaVis 10.1.0.5* software is employed for the acquisition of all the images, their pre-processing and the implementation of the STB tracking algorithm during the experimental investigation.

Figure 4.7: Programmable Time Unit LaVision PTU X [6].

4.5. Force balance

As presented in Chapter 3, the main objective of this thesis is to evaluate the capabilities of volumetric PIV measurements, together with STB tracking algorithms, to reconstruct aerodynamic loads over fluid immersed bodies in experimental aeroelastic investigations. It is, therefore, necessary to perform alternative measurements of the quantities of interest to validate the results of this alternative non-intrusive load determination technique.

A force balance, operated at an acquisition frequency of 100 Hz, is chosen as the validation measurement system in this thesis. The measurement system sits on top of a rotating table that is employed to modify the geometric incidence angle of the test object. The flexible wing model is connected to the balance through an aluminium plate, which is attached to its base with six countersunk M6 bolts, employing eight M8 hexagonal head bolts. The reference measurement system (force balance) consists of a metric and a non-metric frame connected by six load cells (6-axis force balance). Such cells are sensitive to single directions and are decoupled from the rest cells through elastic hinges. The main dimensions of the force balance are given in Figure 4.8.

[5] https://photron.com/es/fastcam-sa1-1/
[6] https://www.lavision.de/en/products/cameras/programmable-timing-unit-ptu-x/

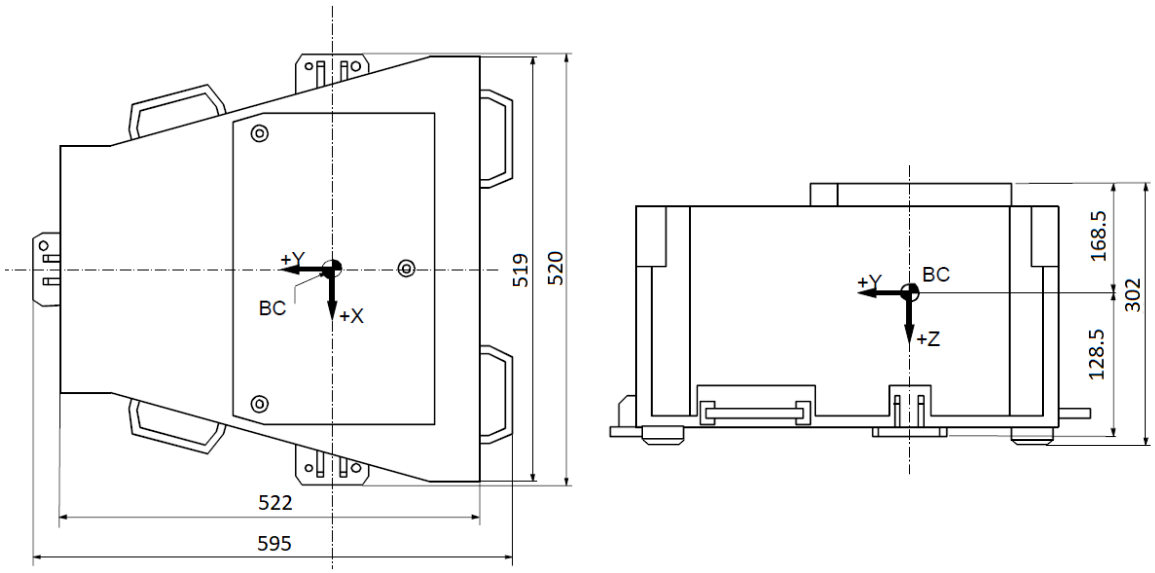

(a) Top View.

(b) Lateral View.

Figure 4.8: Force balance and mount schematic. Most relevant dimensions in millimeters.

The maximum nominal ranges of simultaneously measured loads and single load measurements in the force balance system employed as a reference in the present experimental investigation are given in Table 4.1. Nevertheless, the latter is not of interest in the present experimental investigation, as only simultaneous 6-component measurements were considered.

	Simultaneous measurements	**Single measurements**
Axial Force (F_x)	±250N	±250N
Side Force (F_y)	±500N	±600N
Vertical Force (F_z)	±500N	±3500N
Rolling Moment (M_x)	±500Nm	±550Nm
Pitching Moment (M_y)	±250Nm	±500Nm
Yawing Moment (M_z)	±50Nm	±125Nm

Table 4.1: Force balance load and moment ranges.

The accuracy of the force balance system was determined by means of a first-order dead weight calibration, which resulted in maximum error magnitudes of about 0.15% and standard deviations of 0.05% of the measured load. Such calibration procedures and accuracy parameters are described and defined in the force balance specification sheet. A detailed enumeration of the maximum error and the standard deviation of each of the load cells included in the force balance system is given in Table 4.2.

	ΔF_x	ΔF_y	ΔF_z	ΔM_x	ΔM_y	ΔM_z
Maximum error (ϵ_{max})	0.06	0.23	0.16	0.05	0.05	0.25
Standard deviation (σ)	0.02	0.05	0.05	0.01	0.01	0.07

Table 4.2: Force balance load cells accuracy.

4.6. Experiment setup

The most relevant components of the experimental investigation setup have been enlisted and described in previous sections of this chapter. In this section, a review of their distribution in the OJF will be presented. Moreover, some secondary elements that have not been presented yet will be briefly introduced.

The forenamed components are shown and numbered in Figure 4.9:

1. **Test object:** As discussed in Section 4.3, a flexible wing model is vertically mounted at the outlet of the wind tunnel nozzle.
2. **Imaging sensors:** Presented in Subsection 4.4.3. The cameras are arranged on an aluminium frame located at the left limit of the hydraulic table. Two of the cameras are mounted at the top of the frame pointing downwards, while the remaining camera points upwards and is placed at the bottom of the structure. The lateral angle of the camera is the maximum permitted by the size of the framework.
3. **Illumination source:** Described in Subsection 4.4.2. Three modules are piled up from the bottom of the aluminium frame, where the high-speed cameras are also assembled.
4. **Seeding rake:** Introduced in Subsection 4.4.1. It is located inside the settling chamber of the wind tunnel. The position of the rake is modified in each test case to guarantee a proper seeding density at the measurement volume.
5. **Gust generator:** Outlined in Section 4.2. The vertical vanes are positioned in the center of the aluminum frame that holds the gust generator system.
6. **Force balance & Rotating table:** Showed in Section 4.5. An aerodynamic cover is located upstream of the load cell to prevent the flow stream from affecting its measurements.
7. **Splitting table:** A black wood table that is employed to seal the test model from the clamping and balance components. The objective of the splitting table is the minimization of the interference in the flow stream of any component apart from the flexible wing. It is aligned with the bottom of the nozzle.

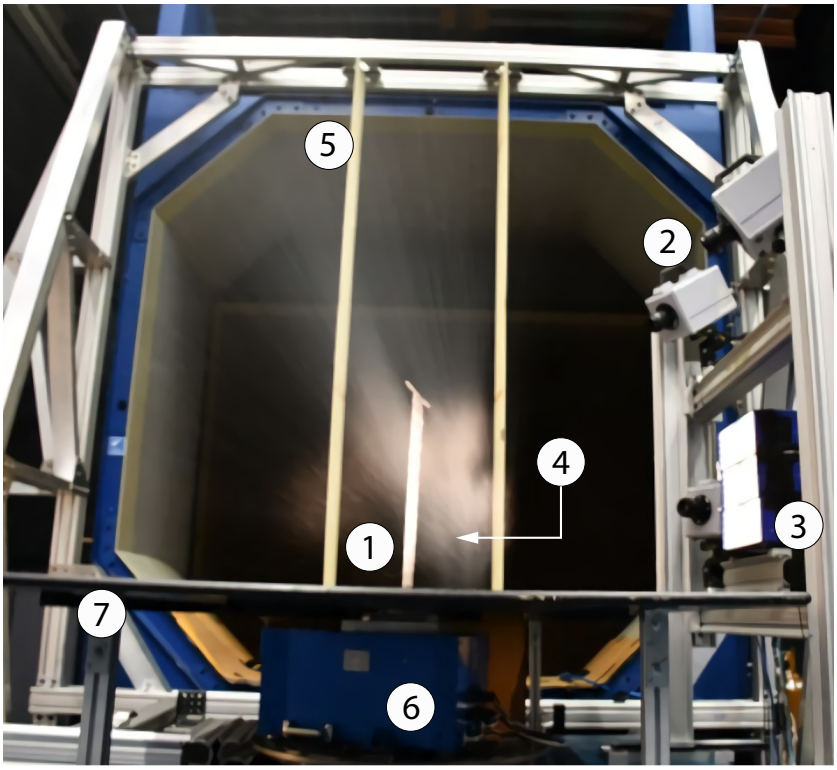

Figure 4.9: Distribution of the most relevant components of the experimental investigation setup.

4.7. Data acquisition procedures

In the last section of this chapter, a description of the setup parameters that define the test matrix of the investigation will be provided, along with a review of the most relevant acquisition strategies employed in the execution of the experimental campaign.

4.7.1. Test matrix

Although the experimental campaign lasted three weeks, only four days were employed to conduct the PIV measurements. For this reason, a carefully designed test matrix was necessary to obtain test data capable of answering the proposed research questions and to achieve the main research objective.

The experimental investigation is divided into two main groups of measurements. On the one hand, test cases involving steady inflow conditions that result in static behaviours of the test object. On the other hand, cases comprising unsteady periodic inflow conditions, imposed by the gust generator, that produce dynamic periodic responses in the flexible wing model. The freestream velocity is maximized to achieve relevant Reynolds numbers and large wing deformations. However, in order to assure the feasibility of the measurements (acceptable particle concentration, prevent vibrations in the experimental setup, etc.), the maximum flow speed of the Open Jet Facility (35 m/s) is not reached. Instead, the wind tunnel is operated at a freestream velocity of $U_\infty \approx 18.3$ m/s; resulting in a Reynolds number of $\mathrm{Re} \approx 1.25 \cdot 10^5$ based on the wing chord.

Concerning the group of measurements with steady inflow conditions, two test cases are proposed:

- **Static Case 1:** The motivation of this first static case is the evaluation of the effects of 3D finite wing phenomena. Fully attached flow with moderate deformations are sought. The geometric incidence angle of the flexible wing is established at $\alpha_0 = 5°$.
- **Static Case 2:** The interest behind the second static case is the analysis of the impact of limited flow viscous effects combined with 3D finite wing phenomena. Greater deflections are attempted while preventing big structural vibrations that do not meet the staticity requirement. The geometric incidence angle of the model is fixed at $\alpha_0 = 10°$.

With regard to the measurements with unsteady periodic inflow conditions, two test cases are proposed:

- **Dynamic Case 1:** The objective of this test case is the assessment of the impact of 3D finite wing effects combined with unsteady flow conditions. For this reason, the frequency of the gust generator is established at f = 5.7 Hz, which results in a reduced frequency of $k \approx 0.1$. Fully attached flow with relatively small deformation is desired. For this reason, the geometric incidence angle of the flexible wing is set at $\alpha_0 = 5°$, while the amplitude of the gust vane oscillation is chosen to be $\beta = 5°$.
- **Dynamic Case 2:** The purpose of the second dynamic case is the investigation of the effect of very large deformations with partial flow separation. Therefore, the gust frequency is chosen to be very close to the first bending (f = 3.2 Hz), which has been previously identified through a Ground Vibration Test (GVT). The geometric incidence angle of the flexible wing is established at $\alpha_0 = 10°$, while the amplitude of the gust vane oscillation is $\beta = 5°$.

	Freestream Velocity [m/s]	α_0 **[deg.]**	**Gust Amplitude [deg.]**	**Gust Frequency [Hz]**
Static Case 1	18.3	5	-	-
Static Case 2	18.3	10	-	-
Dynamic Case 1	18.3	5	5	5.7
Dynamic Case 2	18.3	10	5	3.2

Table 4.3: Simplified test matrix of the experimental campaign.

4.7.2. PIV measurements

As mentioned before, PIV measurements are employed in this thesis to obtain both structural and flowfield LPT data. The sampling frequency of the measurement system is fixed at 5.4 kHz and acquisition times of $t = 1.01s$ (5457 images) and $t = 0.19s$ (1000 images) are used in the flow and structural measurements respectively. The acquisition time of the flowfield measurements is limited by the RAM memory of the high-speed cameras (8 GB). Only one measurement is performed in each static test case, as the acquisition time is sufficient to achieve acceptable particle densities at the measurement volume after the LPT data is time-averaged. However, the phase-averaging of the data in the dynamic cases to account for the unsteadiness of the flow requires more measurements to reach enough particle concentrations around the test object at each phase. In this thesis, five measurements have been performed for each dynamic test case.

On the other hand, due to the limited size of the measurement volume in the vertical direction ($z_V \approx 300$ mm), two different distributions of the imaging sensors are needed to cover the entire span of the model (Figure 4.10). In addition, two acquisitions are performed at each half of the wing, where the geometric incidence angle is $+\alpha_0$ (suction side) and $-\alpha_0$ (pressure side) respectively, to exploit the symmetry of the test object and simplify the data acquisition (Figure 4.11). The resulting four separate measurement volumes are merged together by transforming the LPT data from the measurement coordinate system to the wind tunnel coordinate system employing rigid-body transformations.

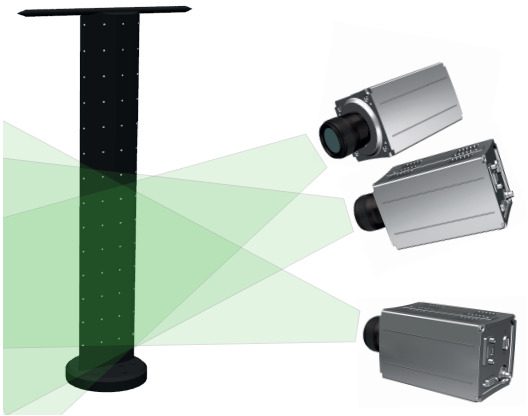

Figure 4.10: Bottom half measurement volume.

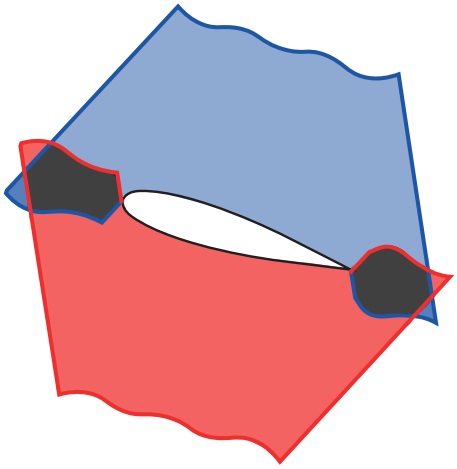

Figure 4.11: Suction side FOV (blue); pressure side FOV (red); overlap region (grey).

5

Data processing strategies

During the experimental investigation, several measurements are performed employing different measurement systems, which have been previously described in Chapter 4. A large amount of images is acquired with the volumetric PIV setup, while text files are obtained from the force balance readings. To answer the research questions proposed in Chapter 3, reaching the main research objective, these sets of data need to be processed and analyzed properly. The strategies followed for this purpose are depicted in this chapter.

Most of the PIV measurements conducted in this thesis result in simultaneous information of structural markers and flow tracing particles. For this reason, the first preprocessing step, which is described in Section 5.1.1, involves their separation into independent data sets. Once the tracers are isolated in independent images, more preprocessing routines are needed to prepare them for their processing (STB). Preprocessing and processing operations are described in Section 5.1 and Section 5.2 respectively. After LPT data is obtained, post-processing operations are required to recover the final flowfield around the test object and its structural displacements. Then, several operations are needed to evaluate the wing aerodynamic loads through the implementation of the theoretical methods described in Chapter 2. All the post-processing steps will be explained in Section 5.3. Finally, the analysis of the force balance measurements is discussed in Section 5.5.

5.1. PIV data preprocessing

Some preprocessing operations are required before flow tracing particles and surface markers are tracked employing the Shake-The-Box algorithm. These steps are mainly related to the isolation of the tracers from undesired reflections and data noise to improve the performance of the LPT algorithms.

5.1.1. Data separation

In this experimental investigation, most of the raw PIV images contain both HFSB and surface markers (Figure 5.1a). Therefore, the first preprocessing step involved in the obtainment of aerodynamic loads consists in their separation into independent data sets. To perform this separation, it is assumed that, in general, flow particles travel much faster than surface markers. Taking this hypothesis under consideration, time-series filtering operations are employed to perform the uncoupling.

A Butterworth High-Pass filter, first implemented to PIV data in Sciacchitano et al. 2014 to remove unwanted reflections and background noise, is used in this research to subtract the surface markers from the raw images. This filter is based on the decomposition of the pixel intensity signal in the frequency domain and the subsequent removal of the low-frequency spectrum (structural markers and surface reflections). A kernel of 7 images is chosen, as it results in an acceptable trade off between the effective removal of surface markers and the inclusion of undesired ghost particles (Figure 5.1b). On the other hand, to acquire data sets of isolated structural tracers information, flow particles are removed from the raw images using a symmetrical time minimum filter. This time operation holds the minimum light intensity at each pixel over a given filter length, which in this thesis is chosen to be 3 images. Contrary to flow tracing particles, surface markers are expected to occupy the same position over the chosen filter kernel for all test cases. For this reason, the implementation of such filter results in the subtraction of illuminated HFSB from the raw images (Figure 5.2a).

(a) Raw image. (b) Flow particles data. (c) Surface data.

Figure 5.1: Raw image and separated flow and structural images. Light intensity displayed with a grey scale.

All the images employed in the present experimental investigation employ the aforementioned separation techniques and parameters. Nevertheless, further steps are needed in the structural isolated images before tracking algorithms are implemented. These operations are described in the following section. No extra operations are required in the separated flow tracers images before particles are tracked with Shake-The-Box.

5.1.2. Structure data preprocessing

Once the illuminated HFSB have been removed from the raw PIV images, further preprocessing operations before the LPT algorithms are implemented to track the reflective markers. Firstly, a sliding minimum filter over a kernel of 12 pixels is subtracted to minimize the influence of undesired surface reflections and noise. Afterwards, a Gaussian smoothing operation over an area of 3x3 pixels is employed to standardize the shape and size of the surface markers. Then, average standard deviation intensity normalization procedures across areas of 40x40 pixels are employed to achieve homogeneous intensity distributions. Finally, geometric masks over regions with persistent reflections are defined to prevent unwanted impact on the final tracking results.

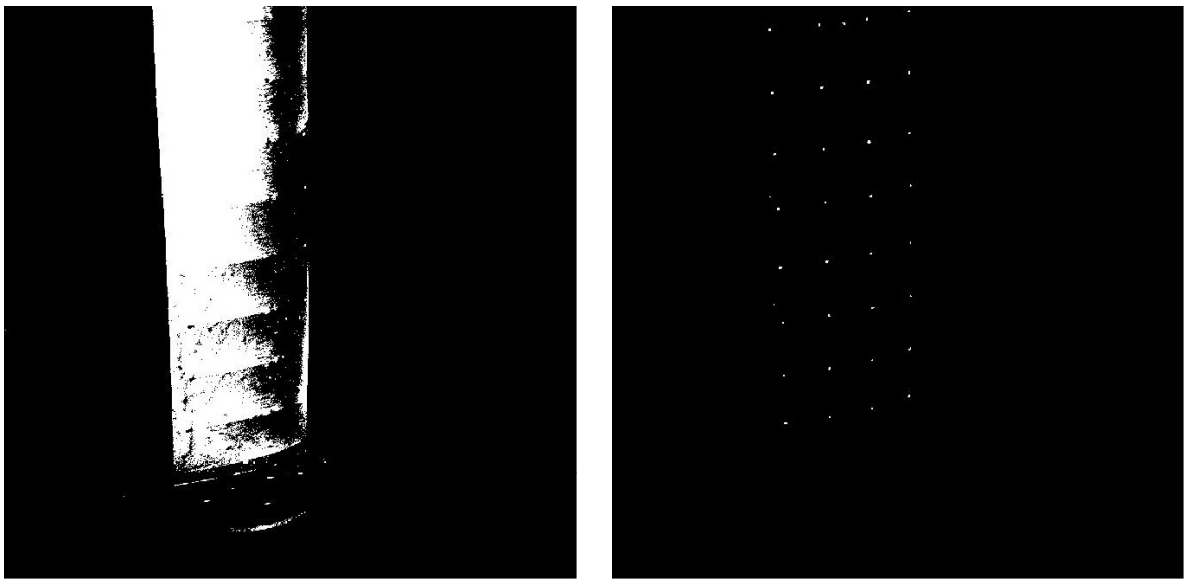

(a) Symmetrical time minimum filter. (b) Final preprocessing image.

Figure 5.2: Structural preprocessing results. Light intensity displayed with a grey scale.

The preprocessing operations and parameters employed to obtain the final structural images are given in Table 5.1, while the differences between the time minimum filter images and the final preprocessing images can be appreciated in Figure 5.2a and Figure 5.2b respectively.

Sliding minimum subtraction	
Kernel [px]	12
Smoothing	
Kernel area [px x px]	3x3
Type	Gaussian
Intensity normalization	
Kernel [pix]	40
Type	Average standard deviation

Table 5.1: Preprocessing operations for structural markers tracking.

5.2. LPT processing operations

After completing the preprocessing operations described in the previous section, several processing steps are needed to transform the PIV images into meaningful flowfield and markers data. The steps taken to obtain such information are described in this section.

5.2.1. Flow particles tracking

HFSB are tracked on the preprocessed PIV images through the Shake-The-Box algorithm. To implement this LPT algorithm, both a Volume Self-Calibration (VSC) and an Optical Transfer Function (OTF) need to be defined. The reader is referred to Wieneke 2013 and Schanz et al. 2016 to gain insight on the working principles of VSC and OTF respectively. For the creation of the VSC and the OTF, undisturbed flow stream images are preferred. In addition, every imaging setup needs independent VSC and OTF. For this reason, 5 different sets of images of the test section without the flexible wing being mounted are defined. The parameters employed in the application of the STB algorithm to trace flow particles are summarized in Table 5.2. The particle tracks information (position and velocity) is obtained in the imaging setup (cameras) reference frame. The transformations needed to obtain this data in the laboratory reference frame are described in Section 5.3.

Particle detection	
Threshold for 2D particle detection [counts]	8.5
Allowed triangulation error [vox]	2
Shaking	
Outer loop iterations	4
Inner loop iterations	4
Shaking particle position [vox]	0.20
Remove particles closer than [vox]	1.00
Particle image shape and intensity	
OTF size factor [-]	1
OTF intensity factor [-]	1
Tracking	
Minimum track length	4 time steps
X velocity limit [m/s]	15 ± 5
Y velocity limit [m/s]	± 2.5
Z velocity limit [m/s]	± 7
Max absolute change in particle shift [vox]	1
Max relative change in particle shift [%]	20
Median filter	off

Table 5.2: STB parameters employed to track flow particles.

5.2.2. Markers tracking

Contrary to flow tracing particles, two different algorithms are employed to analyze the structure dynamics: On the one hand, surface markers are tracked employing an Iterative Particle Reconstruction (IPR) algorithm in the static cases, given their fixed position in space and time. On the other hand, for the test cases involving non-steady inflow conditions imposed by the gust generator, the surface markers are traced with the STB algorithm. Both approaches incorporated non-uniform Optical Transfer Function and Volume Self-Calibration to minimize the tracking errors, as it is also done with flow particles. The chosen parameters for each LPT algorithm are shown in Table 5.4 and Table 5.3.

Particle detection	
Threshold for 2D particle detection [counts]	45
Allowed triangulation error [vox]	2.5
Shaking	
Outer loop iterations	4
Inner loop iterations	4
Shaking particle position [vox]	0.20
Remove particles closer than [vox]	5.5
Particle image shape and intensity	
OTF size factor [-]	0.5
OTF intensity factor [-]	1
Tracking	
Minimum track length	4 time steps
X velocity limit [m/s]	±5
Y velocity limit [m/s]	±15
Z velocity limit [m/s]	±5
Max absolute change in particle shift [vox]	1
Max relative change in particle shift [%]	20
Median filter	off

Table 5.3: STB parameters employed to track surface markers in dynamic cases.

As seen in Table 5.3, the most relevant changes with respect to the setup parameters employed in the HFSB tracking appear in the particle image shape and intensity section. Since the VSC and the OTF are defined employing particles data (Butterworth filtered PIV images), small deviations are expected when they are used to analyze the structural dynamics. In addition, as the distance between surface markers is known, the minimum distance between tracked particles is increased to reduce the noise of the reconstructed marker tracks.

5.3. PIV data post-processing

The implementation of LPT algorithms to preprocessed PIV images result in a Lagrangian description of the flowfield and the structural dynamics in the cameras reference frame. For this reason, several post-processing operations are required to convert this information into manageable data from where aerodynamic loads and other relevant parameters can be extracted.

5.3.1. Reference frame transformations

The first step in the modification of the processed Lagrangian data (both structure markers and flow particles) is the transformation of its reference frame and the subsequent merging of the Fields of View (FOV) belonging to each test case. As described in Section 4.7, due to the limited size of the measurement volume in the spanwise direction of the flexible wing ($\Delta z_{volume} \approx 300$ mm $\approx$ wing span$/2$), two different imaging setups, displaced vertically with respect to each other, are employed to measure the complete test object. In addition, taking advantage of the symmetry of the wing model, mirrored geometric incidence angles ($\pm\alpha_0$) are considered to acquire images on a single side of the wing, corresponding to its pressure and suction sides

respectively. This strategy results in 4 different measurement volumes for each test case that need to be represented in a single data set.

Particle detection	
Threshold for 2D particle detection [counts]	45
Allowed triangulation error [vox]	2.5
Shaking	
Outer loop iterations	4
Inner loop iterations	4
Shaking particle position [vox]	0.10
Remove particles closer than [vox]	5.5
Particle image shape and intensity	
OTF size factor [-]	0.5
OTF intensity factor [-]	1

Table 5.4: IPR parameters employed to track surface markers in static cases.

The reference frame transformation strategy is implemented through auxiliary images that are acquired with every imaging setup. In these supporting PIV measurements, obtained in ground conditions ($U_\infty = 0$ m/s), the test object remains undeformed, which permits the identification of changes in the wing position and attitude caused by variations in the cameras setup exclusively. The required rigid body transformations (translations and rotations) are identified from the differences observed between the forenamed wind-off pictures corresponding to the same test case. The preprocessing operations depicted in Section 5.1 are also employed to modify the auxiliary PIV measurements before the Iterative Particle Reconstruction algorithm is executed. The operations involved in the reference frame transformations are: rotations with respect to the vertical (spanwise) z-axis, equivalent to changes in the pitch angle of the wing; rotations with respect to the transverse (cross-flow) y-axis, comparable to modifications in the wing sweep angle; rotations with respect to the longitudinal (chordwise) x-axis, corresponding to adjustments in the wing dihedral angle; and translations in the three axes.

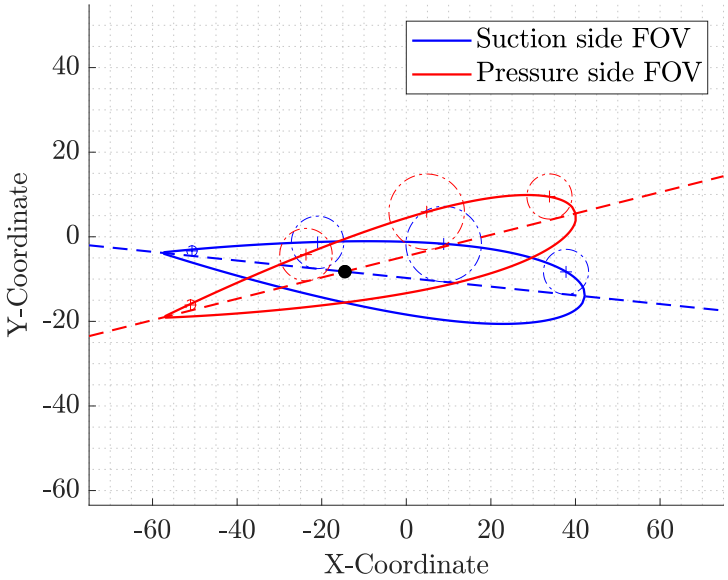

Figure 5.3: Schematic of the procedures for the determination of the pitch rotation axis. Markers positions (blue/red crosses); Airfoil section (blue/red solid line); Half-thickness radius circumferences (blue/red dash-dotted line); Airfoil chord-line (blue/red dashed line); Pitch rotation axis (black dot).

Pitch rotation

Regarding the pitch angle modifications, two parameters are required to execute the data transformations: the coordinates of the axis of rotation and the value of the rotation angle (α). The values of these variables are obtained comparing mirrored measurements ($\pm\alpha_0$) at the same vertical position (either bottom or top FOV). Since the airfoil shape (NACA 0018) and the chordwise position of each of the surface markers are known, the section chord-line can be easily identified. The chord-line is tangent (outer) to the circumferences centered at the location of the markers with a radius equal to the airfoil half-thickness at the corresponding chordwise position. The relative half-thickness of a NACA 0018 airfoil at a given relative chord length follows Equation 5.1.

$$y_t = 90 \cdot \left(0.2969 x_c^{0.5} - 0.126 x_c - 0.3516 x_c^2 + 0.2843 x_c^3 - 0.1036 x_c^4\right) \tag{5.1}$$

The final chord-line equation results from the averaging of the slope and y-intercept of each of the outer-tangent lines in the analyzed section. The procedures to obtain the equations of the external can be found in Weisstein 1999.

Once the chord-line of each pair of mirror images is known, the coordinates of the axis of rotation are easily obtained by recognizing the intersection point between both lines. Assuming that the test model is perfectly centered on the rotating table, the z-rotation axis is expected to be located exactly at the chord mid-point. However, the actual position of the pitch axis is found to be 7 mm behind its expected position. This deviation is persistent in all imaging setups. Thus, the wing assembly on the force balance is slightly shifted in the longitudinal (x-axis) direction. A schematic of the strategy to obtain the location of the pitch rotation axis is shown in Figure 5.3.

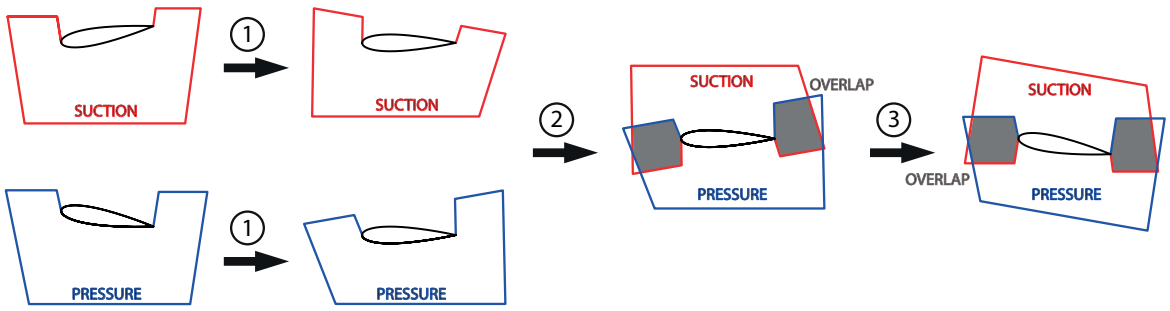

Figure 5.4: Schematic of pitch rotation steps. (1) Align with longitudinal axis; (2) Reverse suction side mirror; (3) Rotate back to original incidence angle.

Concerning the rotation angle, each pair of images (pressure/normal and suction/mirror) is rotated to align their chord-line with the laboratory longitudinal x-axis. Then, the mirroring of the suction side is reversed by changing the sign of all the quantities (position and velocity) in the cross-flow y-axis direction. Finally, both sides are rotated back to their original geometric incidence angle α_0. A schematic of all the steps taken in the pitch rotation transformations is shown in Figure 5.4.

Dihedral and sweep rotations

With regard to the rotation about the longitudinal and traverse axis (x and y axes respectively), similar strategies are followed for both operations. On the one hand, to define the sweep rotation parameters, it is assumed that all trailing edge markers are positioned at the same chordwise location (x-coordinate). Taking this hypothesis into consideration, the sweep angle is obtained from the slope between the top and bottom trailing edge markers of each FOV (wingtip and midspan markers for the top FOV and midspan and wing root markers for the bottom FOV). Similarly, it is considered that all trailing edge markers and leading edge markers are aligned and occupy the same traverse position (y-coordinate). For this reason, the dihedral angle is computed by analyzing the average slope in the y-coordinate between the top and bottom trailing edge and leading edge markers. In both rotating procedures, the axis of rotation is established at the trailing edge of the mid-span rib, which is identified thanks to the extra marker painted at its mid-chord point (Figure 4.3). A schematic of the mentioned rotation angles is given in Figure 5.5 and Figure 5.6.

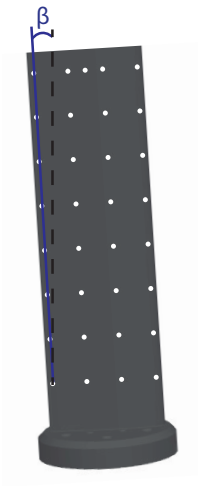

Figure 5.5: Sweep angle.

Figure 5.6: Dihedral angle.

Translations

After the rotation transformations are performed, one last operation is needed to describe the LPT data in the laboratory reference frame: data translation in the three axes of the coordinate system. To perform these translations, the leading edge at the wing-root section is taken as the origin of the laboratory reference frame. In order to position this point, the leading edge marker at the mid-span section, identified with an extra marker at the mid-chord point, is tracked. Then, 310 mm are subtracted in the spanwise (z-coordinate) direction to reach the wing-root section and 5 mm are added in the longitudinal (x-coordinate) direction to meet the actual airfoil leading edge. These values are obtained from the known dimensions of the flexible wing model and the distribution of markers over its surface (Figure 4.3).

Performance of the reference frame transformations

As mentioned previously, Field of View from several measurements are merged in a single data set once they are referenced in the laboratory coordinate system to obtain a complete characterization of the flowfield around the test object. To assess the quality of such reference frame transformations and merging procedures, an accuracy analysis is conducted at the regions where the measurement volumes overlap (Figure 5.4). This study is performed by comparing the flow velocity at points that occupy the same relative position with respect to the wing surface in data obtained during different acquisitions.

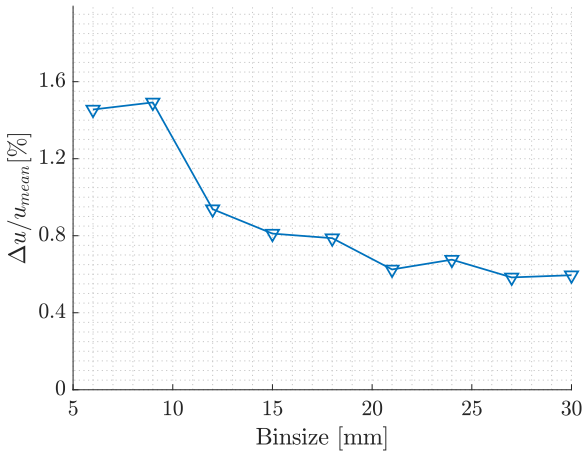

(a) Bottom suction-pressure overlap.

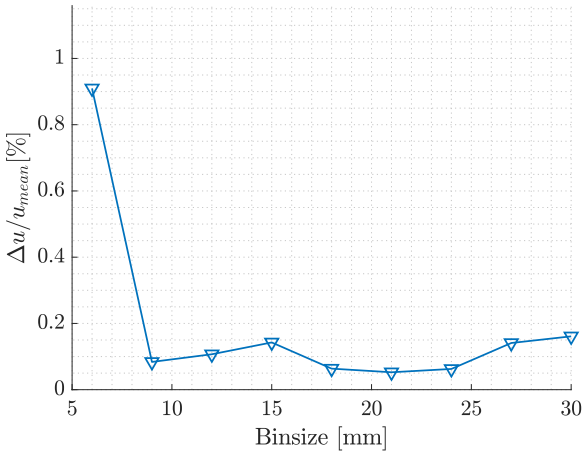

(b) Top suction-pressure overlap.

Figure 5.7: Variation of the flow local velocity magnitude at overlapping regions expressed as a percentage of the local mean flow velocity. Results corresponding to Static Case 2 ($\alpha_0 = 5°$).

In order to prevent the influence of velocity gradients, the points of analysis are located upstream of the test model and away from the wing surface ($\Delta x \approx 50mm \approx c/2$). Typical values of these differences are between 0.25% and 1.75%, as shown in Figure 5.7. Since these variations are on the same order of magnitude as when the merging of the measurement volumes from different acquisitions is performed automatically employing robotic arms (Jux et al. 2018), these differences are considered as acceptable and not further investigated.

5.3.2. Structural markers post-processing

After flow marker tracks are obtained through the implementation of preprocessing operations and LPT algorithms, post-processing procedures are required to acquire the overall information about the structure dynamics. The processing steps required to obtain such data are summarized in Figure 5.15.

Track-sewing algorithm

The implementation of Lagrangian Particle Tracking algorithms in preprocessed structural data results in interrupted paths for most surface markers, being few of them identified with continuous tracks over the entire acquisition time. These disruptions are caused by various events such as the change in particle light intensity; the alteration of the imaged markers shape; the movement of markers out of the measurement volume or their positional uncertainty due to other setup limitations. In order to obtain the instantaneous displacement over the complete measurement period of each of the N_m surface markers (128 markers), reducing the original number of tracks to N_m tracks, a track-sewing algorithm is developed.

The first stage of the sewing algorithm corresponds to the identification of real markers among the particles that are initially tracked (pseudo-markers) at each time step and the subsequent removal of tracks that do not meet certain requirements. This identification phase is composed of various steps:

1. Identify the number of markers (N_z) located within an interval $\pm\Delta$ z = Z mm $\rightarrow$ z $\in (z_i + \Delta z\,,\, z_i - \Delta z)$; where z_i is the vertical coordinate of the analyzed pseudo-marker position.
2. Identify the number of markers (N_x) located within an interval $\pm\Delta$ x = X mm $\rightarrow$ x $\in (x_i + \Delta x\,,\, x_i - \Delta x)$; where x_i is the longitudinal coordinate of the analyzed pseudo-marker position.
3. Discard the pseudo-markers that do not meet the requirements established: $N_x > N_{xmin}$ and $N_z > N_{zmin}$.

In this experimental investigation, the minimum number of markers in the spanwise vicinity (N_{zmin}) is established at 6, considering that 8 markers are painted in each wing rib if both wing sides are taken into account. Similarly, the minimum number of particles that have to be identified in the proximity of each pseudo-marker in the longitudinal direction (N_{xmin}) is 25, knowing that 30 markers are painted in total at each chordwise location. Besides, the size of the search interval in the longitudinal direction is chosen to be ±2.5 mm, while the size of the interrogation interval in the spanwise direction is ±3.75 mm. These parameters might need to be adjusted for other applications or test objects.

Once the first stage of the sewing algorithm is completed, the position of the remaining pseudo-markers, which from now on are considered as the actual wing surface markers, is filtered to obtain their final coordinates at each time step. This second stage of the algorithm consists of two simple levels:

4. Group all markers inside a 3D sphere of radius R_{filter}.
5. Obtain the average position of the markers located inside the forenamed sphere.

In this thesis, a radius of R_{filter} = 5 mm has shown good results in the filtering of the wing structural markers position. This parameter might need to be adjusted to process other data sets.

Finally, after markers are positioned in space at each time step, tracks need to be sewed when interruptions occur. This third stage of the algorithm consists of one main operation:

6. When the track of a filtered marker is interrupted at t_n, a 3D sphere of radius R_{track}, which is centered at the coordinates of the marker at t_n, is created. Filtered marker tracks pertaining to future time steps and located inside the search sphere are considered as the continuation of the interrupted track.

In the present study, a search radius R_{track} = 15 mm is considered.

After the structural marker tracks are identified, transformed to the laboratory reference frame and stitched to avoid interruptions over the complete measurement time; further processing steps are required to reconstruct the flexible wing shape in time, which constitutes the ultimate objective of the structural measurements in this thesis.

Time-averaged markers position in static test cases

In the present experimental investigation, structural staticity is assumed during the static test cases involving steady inflow conditions. The influence of structure vibrations arising from the high flexibility of the wing model is neglected. This assumption is evaluated at the wingtip leading edge marker during the second static test case ($\pm 10°$), as is it the most restrictive in terms of structural displacements.

As shown in Figure 5.8, changes in the longitudinal and spanwise position of the wingtip marker over the complete measurement period are negligible and could be attributed to uncertainties in the tracking procedures. However, these deviations are more relevant in the cross-flow direction, which is also the main direction of the model deformation. Nevertheless, the difference between the maximum deformation and the mean marker position over the whole acquisition time is only 1.45 mm and its standard deviation reduces to 0.65 mm. Such small changes in the y-direction are also recognized as negligible, thus proving the original staticity hypothesis.

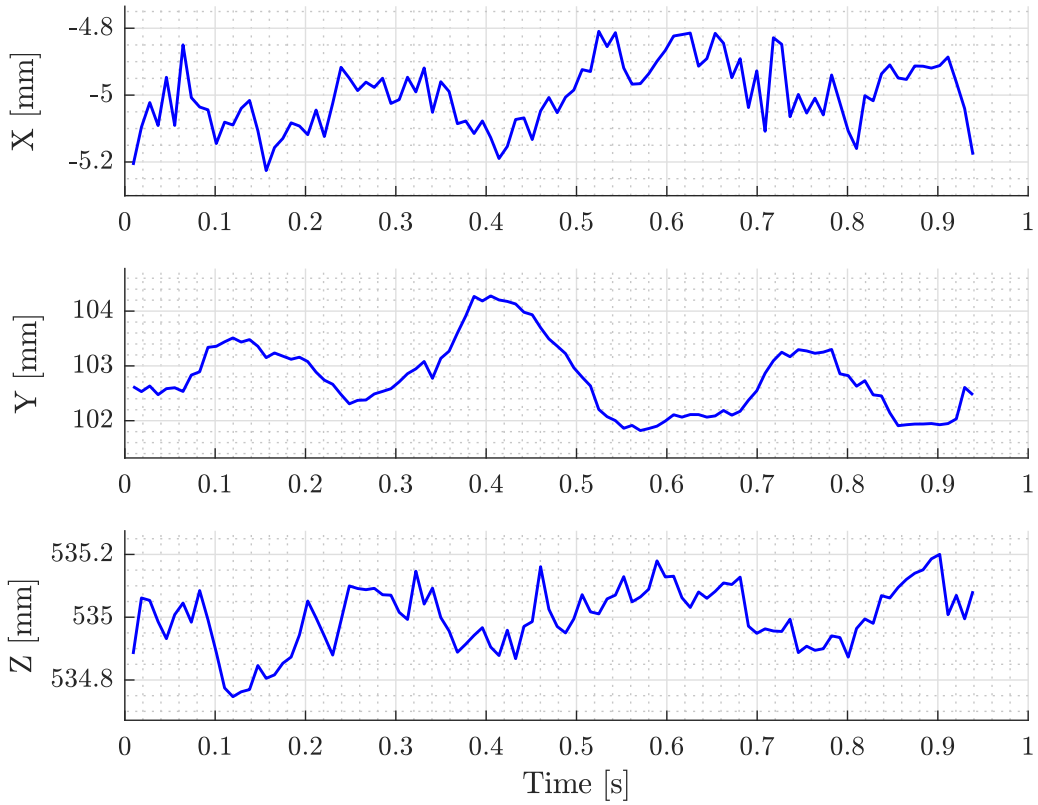

Figure 5.8: Wingtip leading edge marker coordinates. Results corresponding to Static Case 2 ($\alpha_0 = 10°$).

Taking this assumption under consideration, the final coordinates of each of the surface markers results from the time-averaging of their position over the complete measurement period. In addition, a secondary consequence of the staticity hypothesis is the null velocity of the markers over the entire acquisition time. The combination of the reference frame transformations and the sewing algorithms results in a total number of tracked markers very close to the actual number of markers painted over the surface of the test object (128 markers).

Periodicity evaluation in dynamic test cases

In order to study the time-dependent loads acting on the flexible wing with a phase-averaged approach, the periodicity of both the flow and the structure dynamics has to be assessed. This structural analysis is developed on the cross-flow position of the wingtip trailing edge marker. The wingtip section is chosen as a reference due to its restrictiveness in terms of structural deformations and displacements. The longitudinal (x) and spanwise (z) coordinates are not considered in the analysis due to the small changes they experience over the oscillation period. All dynamic measurements (5, as mentioned in Section 4.7) are taken into account to estimate the periodicity of the structural dynamics.

The first step in the assessment of the structure periodicity consists of the definition of a reference sine wave that matches the wing dynamics. This reference oscillation is established employing a least square regression (Equation 5.2) to fit the time-dependent wingtip marker data of all the measurements performed during the experimental campaign.

$$y(t) = y_0 + A\sin(\omega t + \phi) \tag{5.2}$$

The resultant reference oscillations of each of the dynamic test cases, together with the measured marker motions employed in their definition, are shown in Figure 5.9.

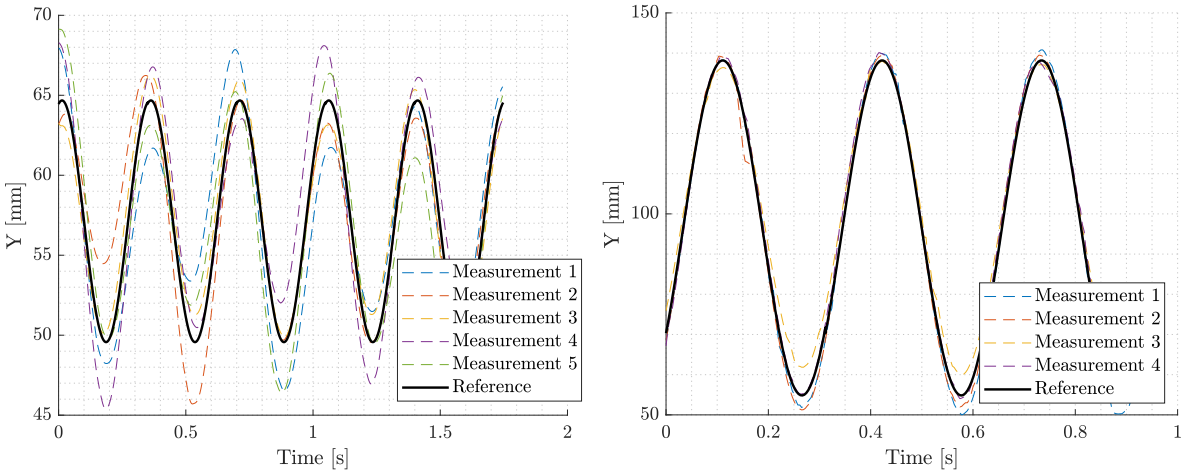

(a) Dynamic Case 1 ($\alpha_0 = 5^\circ$; f = 5.7 Hz). (b) Dynamic Case 2 ($\alpha_0 = 10^\circ$; f = 3.2 Hz).

Figure 5.9: Reference oscillation of the wingtip leading edge marker with measured marker motions.

The second step in the analysis of the periodic repeatably of the wing motion comprises the evaluation of its deviation to the reference oscillations. If the test object showed a completely periodic behaviour, the differences between the measured marker motions and the reference oscillations would be non-existent.

	Deviation to reference [mm]	**Oscillation amplitude** [%]	**Bin size** [%]
Dynamic Case 1	0.2 ± 2.3	1.3	1.3
Dynamic Case 2	0.4 ± 4.2	0.5	2.6

Table 5.5: Overview of the periodicity analysis results in terms of the deviations to the reference motions.

This analysis is executed in both dynamic cases, finding position deviations over the complete cycle of 0.2 ± 2.3 mm and 0.4 ± 4.2 mm in the first and second dynamic experiments (Table 4.3) respectively. These mean deviations correspond to a 1.3% and a 0.5% of the reference oscillation amplitudes (15.1 mm and 83.3 mm) and a 1.3% and a 2.6% of the size of the reference ensemble average interrogation window (15 mm, as it will be explained in the following sections of this chapter). An overview of these results is given in Table 5.5.

In addition, as shown in Figure 5.9, wing motions corresponding to Dynamic Case 1 measurements show certain deviations in the frequency domain over the acquisition time, as phase-shifts with respect to the reference oscillation can be seen in various periods. These phenomena are also visible in the analysis of the position deviation (Figure 5.10), where an oscillatory behaviour of the y-coordinate differences, with frequency $f \approx 3$ Hz, is appreciated. This effect might be attributed to the influence of the first bending mode of the test object ($f \approx 3.2$ Hz), which produces a coupled wing motion that does not follow the excitation frequency ($f \approx 5.7$ Hz) completely.

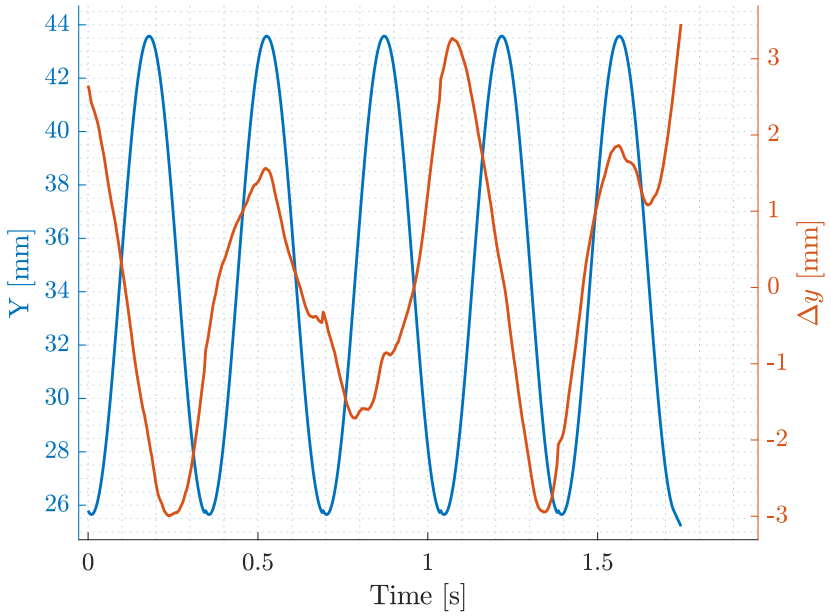

Figure 5.10: Time-dependent correction vector of top marker y-coordinate. Reference oscillation (blue line); Deviation in y-coordinate with respect to the reference oscillation (red line). Results corresponding to 1st measurement in Dynamic Case 1 ($\alpha_0 = 5^\circ$; f = 5.7 Hz).

Nevertheless, these deviations are considered to be sufficiently small compared to relevant parameters like the oscillation amplitude or the ensemble bin size, to ensure the original hypothesis of motion periodicity, thus permitting the post-processing of time-dependent data with a phase-averaged approach.

Phase-averaged markers position in dynamic test cases

After the wing motion periodicity assumption is proven, the time-dependent description of the surface markers needs to be transformed into equivalent phase-averaged data, from where the wing shape at each phase-center can be reconstructed.

First, a similar strategy to that followed for the periodicity analysis is employed: A reference sinusoidal wing motion is defined through non-linear regressions of the structure dynamics (Equation 5.2), from where the reference periods of the aeroelastic events are established ($T_{ref} = 2\pi/\omega$). Then, the temporal information of the Lagrangian data is split into consecutive cycles with duration T_{ref}. Subsequently, the cycle phase-centers ($t = t_{phase}$), are identified in each of the resulting individual cycles by dividing the reference period into a pre-determined number of phases (N_{phases}) and adding the relative time instants of these phase-centers to the starting time of each cycle (Figure 5.11). The number of phases that has been selected to perform the phase-averaged analysis of the time-dependent loads in both dynamic test cases is $N_{phases} = 25$.

Once the reference period is determined, the temporal information of the Lagrangian data is modified to describe it as a single cycle of the original signal. This time-shift value is equal to the difference between the starting time of the cycle being adjusted and the starting time of the first cycle. Eventually, the temporal collapsed data is non-dimensionalized choosing the reference period as characteristic unit ($t' = t/T_{ref}$). As a result, a unique time reference system for data sets pertaining to different measurements is obtained.

After the oscillation periods and phase-centers are determined and the temporal data from all acquisitions is collapsed into a single non-dimensional cycle, the ensemble phase-averaging of the structural data is performed.

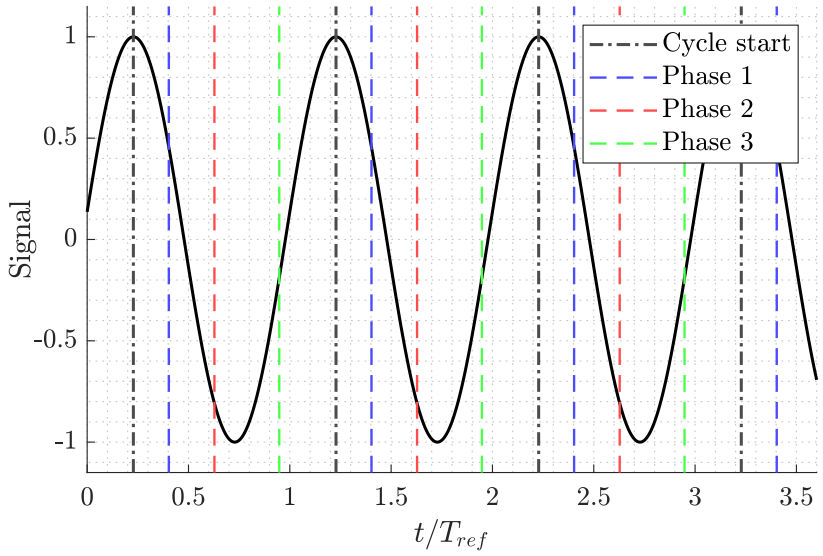

Figure 5.11: Identification of phases over the entire acquisition time.

The first step of the algorithm consists of the recognition of Lagrangian data that falls inside pre-defined temporal bins where the averaging process is executed. To accomplish this objective, it is required to identify marker tracks pertaining to temporal windows (t_{window}) that are centered at the center of the phase being averaged (t_{phase}) and that extended symmetrically for certain time (Δt). A time window of $\pm\Delta t = T_{ref}/20$ has proven to provide acceptable results in the present investigation, although other values might be preferable for other applications and data sets.

$$t_{window} \in \left(t_{phase} \pm \Delta t\right) \tag{5.3}$$

Once marker tracks from different acquisitions that fall inside these temporal windows have been identified, it is required to group those corresponding to the same wing marker before the ensemble average is performed. To do so, a searching sphere with radius $R = 5$ mm is employed, resulting in a final spatio-temporal assembly of the original time-dependent data.

After the grouping of the time-dependent marker tracks from different measurements is performed, the calculation of the phase-averaged position of the wing markers is carried out. This averaging is done employing a sliding time-window regression of a first-order polynomial (Mitrotta et al. 2021). The analysis is developed on each of the groups of markers individually. This linear sliding regression function can be expressed as:

$$x_i\left(t'\right) = a_i + b_i \cdot t' \tag{5.4}$$

Where t' is the non-dimensional time $t(t' = t/T_{ref})$; x_i are the marker coordinates (x, y, z) at $t = t'$; and a_i and b_i are the regression coefficients.

Similarly, the standard deviation of the phase-averaged marker coordinates is given by:

$$\sigma_{x_i} = \sqrt{\frac{1}{N_p - 1}\sum_{n=1}^{N_p}\left(x_{n_i} - x_i\left(t_{phase}/T_{ref}\right)\right)^2} \tag{5.5}$$

Where N_p is the number of points (markers in the group) employed to compute the linear regression, x_{n_i} are the coordinates of the n^{th} data point and t_{phase}/T_{ref} is the non-dimensional phase center time instant. Following this method (Equation 5.4), not only can the phase-averaged marker coordinates and their standard deviations be obtained, but also other relevant quantities such as their phase-averaged velocity components ($v_i = b_i$).

Wing shape reconstruction

All the procedures that have been described up to this point aim to improve the quality of the original PIV images (Section 5.1); acquire Lagrangian information of the markers dynamics (Section 5.2); and modify the resultant track information to obtain both time-averaged and phase-averaged marker grids in the laboratory reference frame. Even though this information is already useful, the reconstruction of the complete wing shape poses an appealing improvement in terms of structural data recovery, which leads to better understandings and descriptions of the FSI event. In addition, the awareness of the reconstructed wing shape permits the definition of masks to be included in the velocity flowfield, which improves the overall performance of the non-intrusive load determination methods. Therefore, the next processing operation to be implemented in the time and phase-averaged structural data is the determination of the wing form.

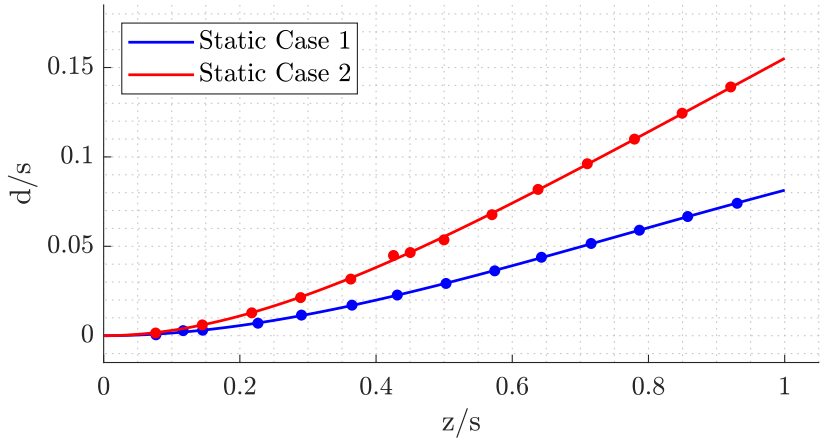

Figure 5.12: trailing edge displacement measurements along the span together a with polynomial curve fit. Measured markers displacement (point); 4^{th} order polynomial fit of the markers displacement (line).

The first step in the reconstruction of the deformed shape of the test object is the positioning of the wing leading and trailing edges at the spanwise locations where the markers are painted (i.e. ribs of the model). The location of these points is found through the known coordinates of the foremost and rearmost surface markers at the suction and pressure sides of the flexible wing (Figure 4.3). Once these coordinates are known, a fourth-order polynomial is employed to fit their distribution in the spanwise direction. The geometric boundary conditions of a beam clamped at its root ($d(z=0)=0$ and $d'(z=0)=0$) are considered in the definition of the fitting model. The results of the polynomial curve fit to the trailing edge marker measurements for both static test cases are given in Figure 5.12. The resultant polynomial is expressed as:

$$d(z) = A \cdot z^4 + B \cdot z^3 + C \cdot z^2 \tag{5.6}$$

Besides, following the determination of the bending (y-coordinate) displacements, the knowledge of the torsional deformation is required to reconstruct the deformed shape of the test object. This torsional deformation, which reaches its maximum at the tip of the flexible wing, can be analyzed in terms of the twist angle (θ) around the elastic axis of the model. In this thesis, the transformed marker tracks have been employed to determine the value of such deformation, finding angles below 0.5° in both static test cases and below 0.75° over the entire cycle of both dynamic cases. Based on these small values of θ and taking into account that the interest of this experimental investigation lays in the determination of aerodynamic loads, the torsional deformation of the wing is considered to be negligible, thus simplifying the wing shape analysis.

Following this reasoning, the wing shape is directly reconstructed from the polynomial curve fit of the bending displacement distribution. This surface-reconstruction phase is achieved through the recognition of the airfoil chord-line along the span, which is directly obtained from the leading and trailing edge displacements. Eventually, the known airfoil shape (NACA 0018) is positioned at each spanwise position by implementing its relative thickness equation (Equation 5.1). Finally, the 3D wing geometry is reconstructed from the resultant mesh of airfoil sections, as seen in Figure 5.13.

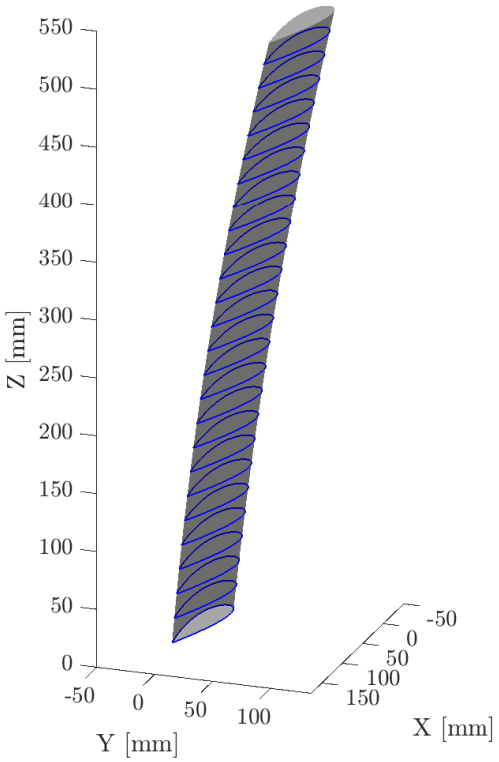

Figure 5.13: Reconstructed wing geometry under loading conditions. Wing surface (grey); airfoils grid (blue line). Results corresponding to Static Case 2 ($\alpha_0 = 10°$).

5.3.3. Lagrangian flow particles post-processing

Once flow particle tracks have been obtained through the implementation of preprocessing operations and LPT algorithms to raw PIV images, further processing steps are required before the non-intrusive load determination methods are implemented. All the processing steps required to obtain the final Eulerian flowfield data are summarized in Figure 5.17.

Wing shadow flow data masking

With the objective of accounting for the shadow generated by the test object, data resulting from the implementation of reference frame transformations is masked before the measurement volumes of different acquisitions are merged. Due to their limited or non-existent optical accessibility, all particles falling inside these shadows are considered to be ghost particles. Their removal supposes an improvement in the accuracy of the final ensemble Eulerian flowfield. The information about the deformed shape of the flexible wing is employed to define the region occupied by these shadows where particle tracks are removed.

First, the position of the wing leading and trailing edges at each spanwise location (z-coordinate) is established. Then, based on the shape of the data gap behind the wing surface, the angle that each of the shadow limits forms with the traverse direction (y-axis) is determined. Finally, this information is employed to define the final shadow shape by drawing lines from both airfoil limits that follow such angles and closing the mask polygon with the chord-line between both points. An example of the procedures taken to implement these wing shadow masks and the resultant particle tracks distribution is given in Figure 5.14.

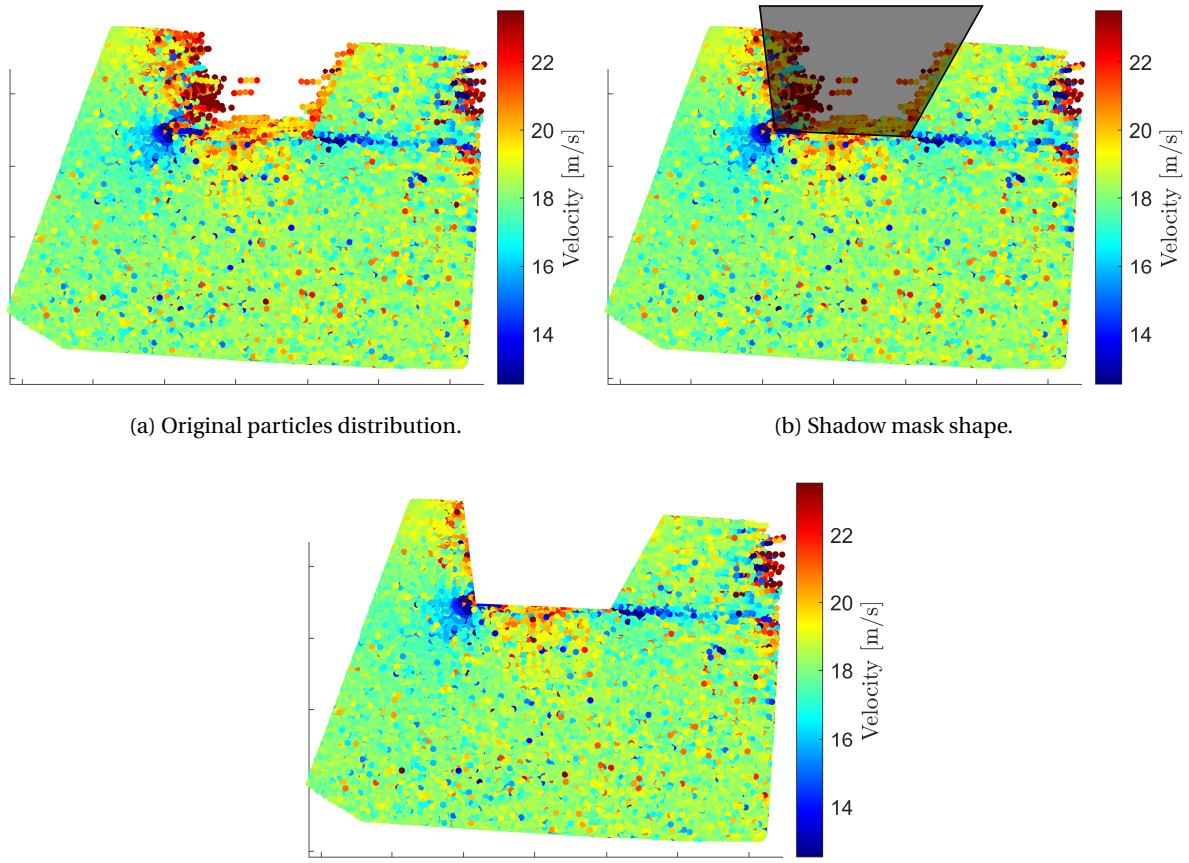

(a) Original particles distribution.

(b) Shadow mask shape.

(c) Masked particle tracks.

Figure 5.14: Wing shadow mask implementation steps. Flowfields corresponding to Static Case 2 ($\alpha_0 = 10°$).

Ensemble averaging of flow particle tracks

After flow particles have been tracked, transformed to the laboratory reference frame, masked and merged into a single data set that covers the entire test model; they need to be converted into Eulerian information described on a structured grid. Depending on the temporal character of the data, two different approaches are taken to perform such transformations:

- **Static test cases:** Spatial ensemble average of the particle tracks over the entire acquisition time.
- **Dynamic test cases:** Spatio-temporal ensemble average of the particle tracks for each cycle phase.

First, a structured mesh that covers the volume occupied by the particles during the entire acquisition time is created. The nodes of the resultant grid are considered as centroids of the spatial interrogation windows employed during the averaging process. These windows have a cubic shape with a linear size l_B. A bin size of $l_B = 15$ mm with a 75% overlap is used in this thesis to obtain the reference Eulerian flowfield from where the aerodynamic loads are computed. Then, a similar strategy to that followed for the phase-averaging of the marker tracks in dynamic test cases is followed: the temporal information of the Lagrangian particle tracks is divided into cycles with duration T_{ref}, which are subsequently collapsed into a single non-dimensional cycle where phases ($N_{phases} = 25$) are defined. Particles falling inside pre-established time windows are identified (Equation 5.3). In this experimental investigation, a time window of $\pm\Delta t = T_{ref}/16$ is selected to obtain the reference phase-averaged Eulerian flowfield from where the aerodynamic loads in dynamic test cases are computed. No temporal information is employed during the ensemble average of the particle tracks from static test cases, as particles from the entire acquisition time are employed to obtain the time-averaged flowfield. Particles contained inside each spatio-temporal window are used to conduct the ensemble time and phase averaging of the Lagrangian flow data.

In order to minimize the uncertainty of the reconstructed velocity flowfield, a minimum number of particles ($N_{p,min}$) inside each spatio-temporal bin is required to implement the ensemble average algorithm. Interrogation windows with a number of particle tracks below the $N_{p,min}$ are not considered for the Eulerian transformation. In the present investigation, the minimum number of particles required for the static test cases is established at $N_{p,min} = 35$, while the number in dynamic test cases is reduced to $N_{p,min} = 20$.

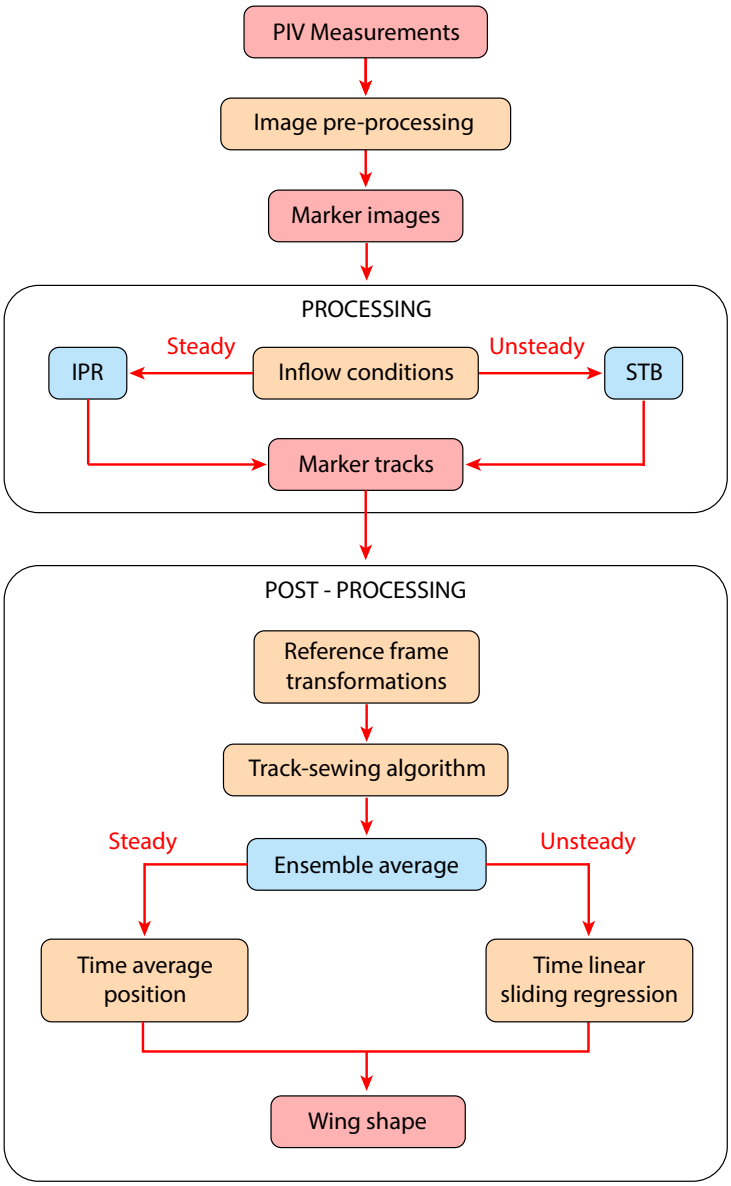

Figure 5.15: Marker tracks processing flow chart.

Various methods can be employed to conduct the ensemble average inside each spatio-temporal bin (Figure 3.7), going from simple top-hat filters, like done by Jux et al. 2018, to higher other methods like the Gaussian function or polynomial fits (Agüera et al. 2016). In this thesis, a first-order polynomial is chosen to fit the Lagrangian data inside each interrogation window. To implement such fit, the particle velocity components are defined as:

$$u_i\left(\Delta x, \Delta y, \Delta z, \Delta t/T_{ref}\right) = a_1 + a_2\Delta x + a_3\Delta y + a_4\Delta z + a_5\Delta t/T_{ref} \tag{5.7}$$

Where Δx, Δy and Δz are the distances to the bin centroid in each of the directions of the cartesian reference frame, $\Delta t/T_{ref}$ is the distance to the phase-center and $a_1, ..., a_5$ are the unknown coefficients that need to be determined to solve the averaging problem. These coefficients are obtained by finding the least-square solution of the system of equations that results from the position and velocity information of each of the particles inside the spatio-temporal interrogation window (Agüera et al. 2016). The temporal term $(a_5 \Delta t)$ of the fitting polynomial (Equation 5.7) is not considered during the ensemble average of the static cases data $(a_5 = 0)$.

The mean velocity of these particles is equivalent to the fit velocity at the center of the bin:

$$\overline{u_i} = u_i\,(0,0,0,0) = a_1 \tag{5.8}$$

Once the polynomial coefficients are determined, other relevant parameters like the mean spatial and temporal gradients of the particles inside the interrogation window can be determined:

$$\frac{\partial u_i}{\partial x} = a2\,; \quad \frac{\partial u_i}{\partial y} = a3\,; \quad \frac{\partial u_i}{\partial z} = a4\,; \quad \frac{\partial u_i}{\partial t} = a5\,; \tag{5.9}$$

Besides, the standard deviation of the predicted velocity components is expressed as:

$$\sigma_{u_i} = \sqrt{\frac{1}{N_p - 1} \sum_{n=1}^{N_p} \left(u_{i,n} - u_i\left(\Delta x_n, \Delta y_n, \Delta z_n, \Delta t_n\right)\right)^2} \tag{5.10}$$

Where N_p is the number of particles employed to perform the polynomial fit, Δx_n, Δy_n, Δz_n and Δt_n are the distances to the center of the interrogation window of the n^{th} inside the bin and $u_{i,n}$ is the mean velocity in the interrogation volume.

An example of the Eulerian velocity flowfield resulting from the implementation of such ensemble average procedures to Lagrangian particle data is given in Figure 5.16.

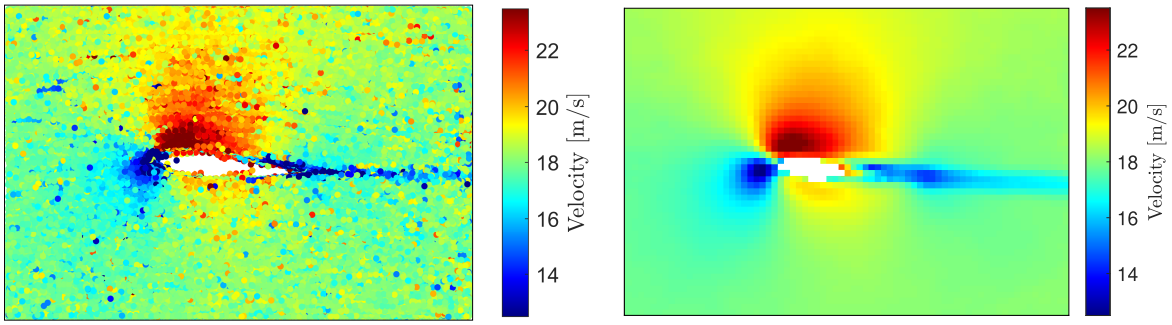

(a) Lagrangian flowfield.

(b) Eulerian flowfield.

Figure 5.16: Lagrangian (left) and Eulerian (right) 2D velocity fields. Flowfields corresponding to Static Case 1 $(\alpha_0 = 5°)$ at $z = 225$ mm.

5.3.4. Eulerian flowfield post-processing

The implementation of the aforementioned ensemble average algorithms results in Eulerian velocity data of the flow surrounding the test object. However, certain transformations are still needed before this information is suitable for the extraction of aerodynamic loads employing the methods described in Chapter 2. In this section, a brief description of the most relevant procedures required to achieve such objective is presented.

Determination of inflow conditions

The first step taken after Eulerian descriptions of the flowfield are obtained is the determination of the inflow velocity components of each experimental test case. Although it is assumed that the flow speed at the wind tunnel nozzle outlet is known, small changes in the flow velocity at the test section are expected due to changes in the experimental setup, long waits between acquisitions, etc.

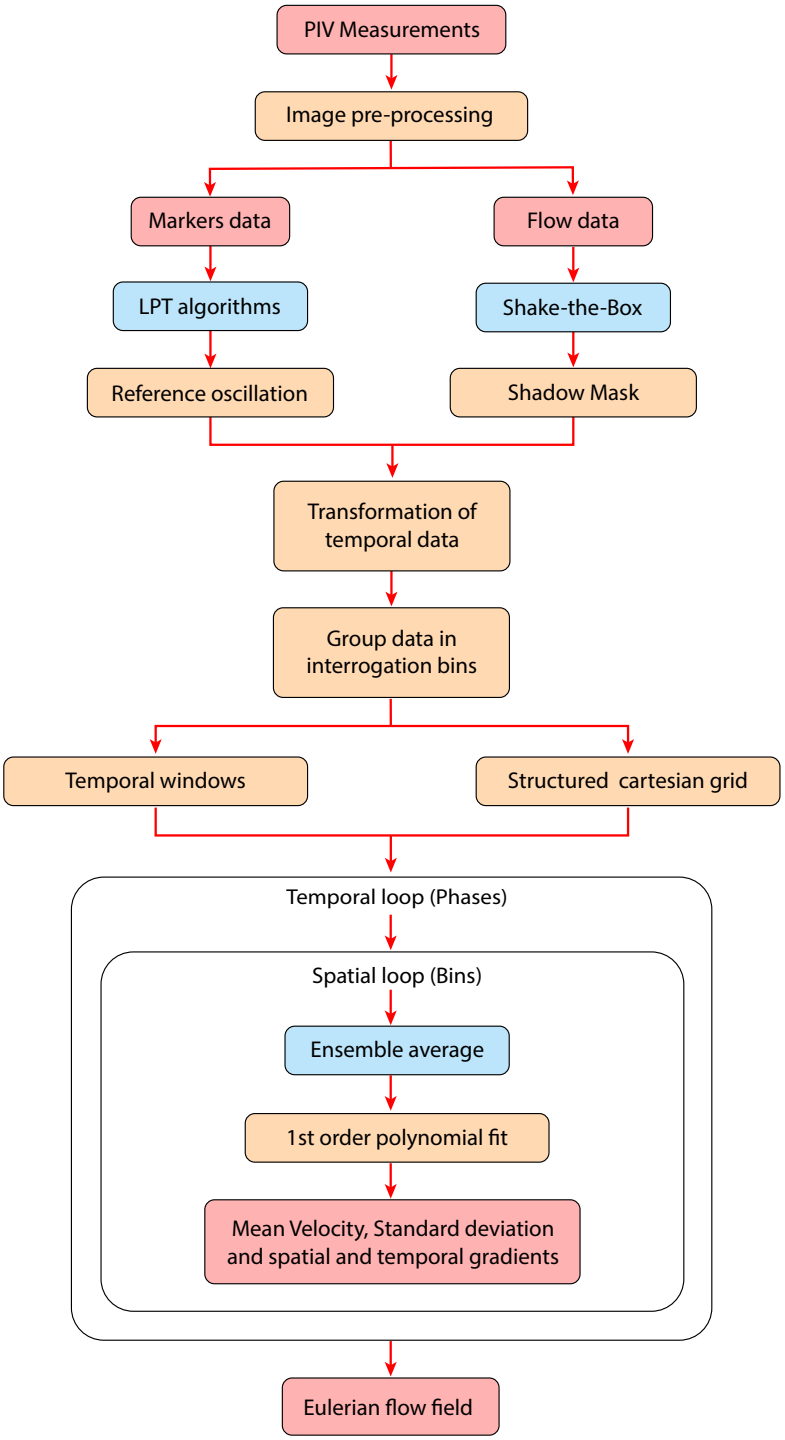

Figure 5.17: Flow particles processing flow chart.

In addition, in order to obtain a better understanding of the reconstructed aerodynamic loads, it is convenient to analyze the changes that this inflow velocity might experience over the entire cross-section upstream of the test model. However, such analysis cannot be performed if the flexible wing is mounted at the test section; as the measurement volume (Figure 5.16) does not extend sufficiently upstream to avoid the influence of the stagnation point in the velocity distribution across the foremost boundary of the measurement volume. For this reason, auxiliary measurements, where the test object is taken apart, are carried out after every change in the setup and at the beginning and the end of each day.

As seen in Figure 5.18, the freestream velocity measured at the test section does not present a constant behaviour. On the contrary, considerable gradients are appreciated both at the wing root region (up to ≈ 100 mm) and around the midspan section. The latter is caused by the employment of various measurement volumes during different days of the experimental campaign to analyze the bottom and top half of the test model (as explained in Section 4.7). The realization of such measurements on different days leads to small variations in the speed at the outlet of the wind tunnel nozzle and thus on the flow velocity at the test section. On the other hand, the gradient that is appreciated at the wing root region is attributed to the boundary layer of the splitting table (Figure 4.9). The influence of such gradients on the spanwise distribution of the aerodynamic loads will be analyzed in Chapter 6.

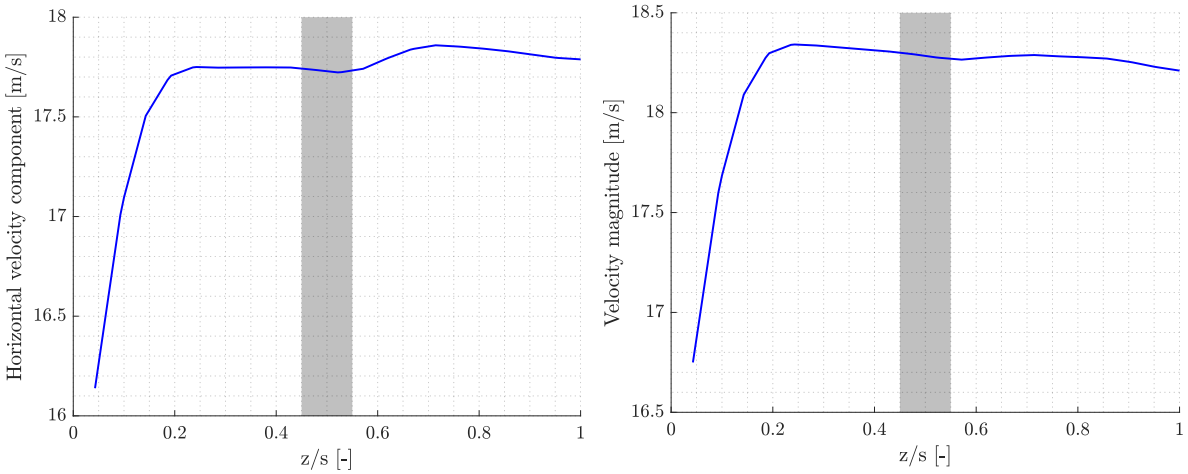

(a) Horizontal velocity component (u).

(b) Velocity magnitude $(\overline{U})$.

Figure 5.18: Vertical distribution of the mean inflow velocity in static test cases. Velocity (blue line); overlap region between top and bottom measurement volumes (grey area).

Wing shape masking

Even after Lagrangian particle data is masked to account for the optical inaccessibility of the flow tracers positioned behind the test object (shadow), certain interrogation windows that fall inside the region occupied by the flexible wing meet the requirements imposed to perform the ensemble average inside them ($N_p > N_{p,min}$). For this reason, it is necessary to transform the information of the cells that are occupied by the wing model. This transformation is performed by querying the relative position of each of the grid cells with respect to the wing surface. The mean velocity components inside the cells covered by the test object are defined as null ($u_i = 0$ m/s). An example of the implementation of such mask is given in Figure 5.19.

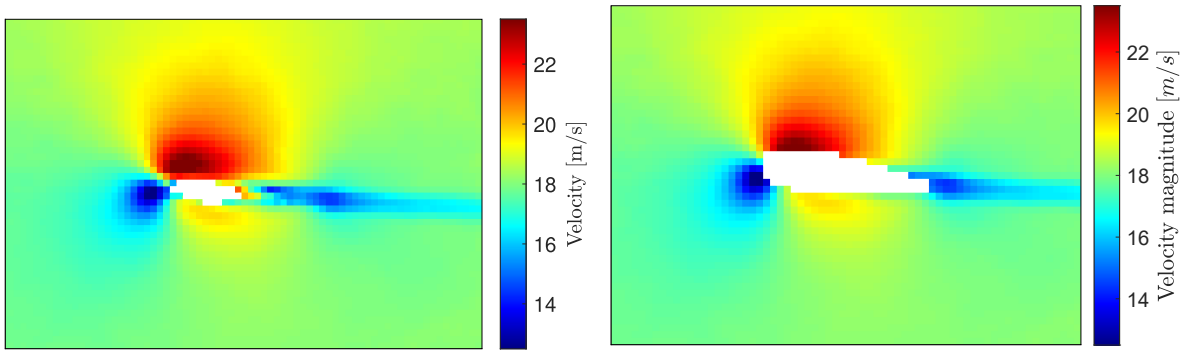

(a) Original.

(b) Masked.

Figure 5.19: Mask implementation in 2D Eulerian flowfields. Flowfields corresponding to Static Case 1 $(\alpha_0 = 5°)$ at $z = 225$ mm.

Interpolation of missing data

The last step in the preparation of the flowfield information, before load reconstruction strategies are implemented, is the interpolation of flow data at regions where the ensemble average could not be performed. The reason behind this lack of information at certain cells of the cartesian grid is their failure to fulfill the established concentration requirements ($N_p < N_{p,min}$). Nevertheless, few grid points require this reconstruction, as the minimum number of particles needed inside each interrogation window ($N_{p,min}$) is chosen considering both the need to minimize the ensemble average uncertainty and the mean particle concentration at the test section. Even so, regions with large accumulations of data gaps are avoided during the execution of the final load reconstruction algorithms in order to avoid a significant influence of numerical errors derived from this data interpolation.

Due to the strong gradients expected in the stream-flow and the cross-flow directions (x-axis and y-axis respectively), the vertical direction (z-axis) is selected as the preferred orientation of the interpolation path. However, the large deflections experienced by the test model limit the applicability of the interpolation algorithm along this line, as cells with the same planar coordinates (x, y) can show considerable deviations in their relative position to the wing surface even when small changes in the vertical coordinate (z) occur.

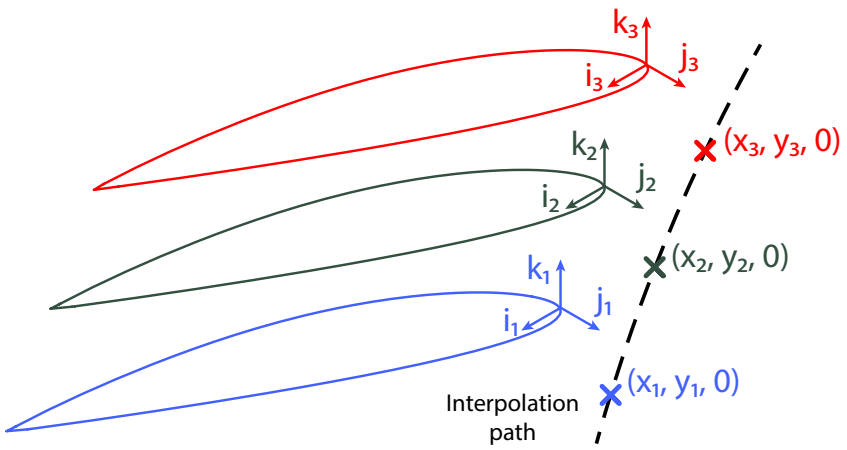

Figure 5.20: Schematic of the data interpolation path employed in deformed wing shapes.

Following this reasoning, the orientation of the interpolation path is modified so that the relative position of the data points employed to perform the calculations is identical to that of the data point to be interpolated (Figure 5.20). The known deformed shape of the flexible wing is employed to obtain the local coordinates of the cells being modified. Subsequently, equivalent cells (occupying the same local coordinates), located in planes above and below the data gap, are identified. Finally, the missing data point is interpolated fitting the values at the cells above and below the problematic grid point with a second-order polynomial.

5.4. Implementation of non-intrusive load determination methods

Once the last post-processing procedures are implemented to the ensemble average Eulerian flowfields, they are ready for the application of the load determination methods described in Chapter 2. In this section, a brief description of the techniques employed to implement such methods will be given.

The first step in the quantification of aerodynamic forces is the definition of control volumes and integration paths enclosing the test object, since the load determination methods described in Chapter 2 depend exclusively on the flow quantities at their boundaries. In this thesis, several volumes arranged in the spanwise direction are employed to retrieve sectional results, which are later integrated to obtain the overall aerodynamic forces acting over the flexible wing.

To simplify the obtainment of flow quantities at the boundaries of the control volumes, their location is chosen to be coincident with the nodes of the cartesian grid that describes the flowfield. In this way, the in-

terpolation of the flow quantities at the intersection points between the grid cells and the boundaries of the control volumes is prevented. In addition, in order to avoid data with noise levels above the acceptable limits, a region around the wing where no control volume boundaries can be established is defined. The distance between the limits of this safety region and the closest grid node to the wing surface at each spanwise location is fixed at $d_{gap} = 0.15 \cdot c$; being c the chord length of the flexible wing (c = 100 mm). Following these lines of reasoning, the distance of each of the sectional control volume boundaries (suction side, pressure side, upstream and downstream boundaries) to the limits of the safety zone is defined to be a multiple of the grid cell size (Δx). This distance is maintained across the entire wing span, which ensures that the relative position of every control volume to the airfoil section is the same for all spanwise positions. A schematic of the forenamed dimensions and strategies is given in Figure 5.21.

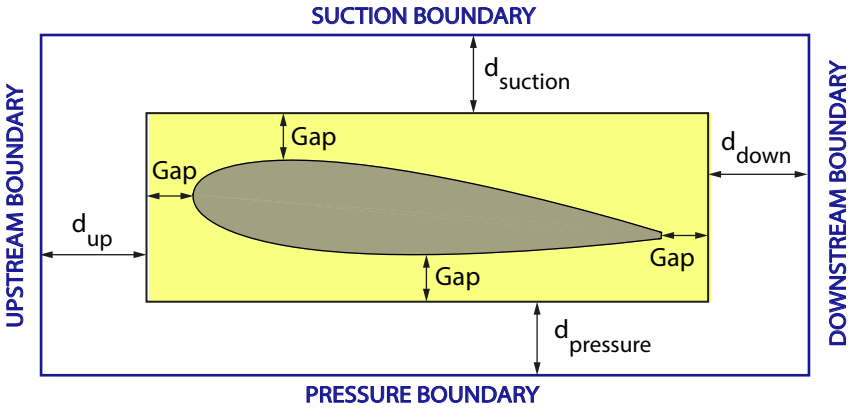

Figure 5.21: Schematic of the control volume definition strategy and the most relevant dimensions. "Safety" zone (yellow region) and airfoil section (green section).

Following a strategy similar to that chosen in other studies like Mertens et al. 2021b, the results obtained with various control volumes sizes and shapes are averaged to one single result to minimize the impact of random error in the Eulerian flowfield. Further steps in the analysis of the effects of the location of the control volume boundaries will be taken in Chapter 6.

After the size and shape of all the control volumes across the span are defined, the next step in the evaluation of aerodynamic loads over fluid-immersed bodies is the identification of the flow quantities that are required to implement the load determination strategies (Chapter 2) and their subsequent obtainment. As described in (Section 5.3.3), the ensemble average of Lagrangian tracks through first-order polynomial fits permits the reconstruction of mean velocity components and velocity spatio-temporal gradients at the center of each cell of the cartesian grid and thus of other velocity related quantities as the vorticity vector (ω) or the viscous stress tensor (T). However, in order to assess the impact of the precision of these gradients in the accuracy of the reconstructed loads, these gradients have also been obtained employing second degree first-order finite differences of the mean velocity flowfield:

$$\frac{\partial u_i}{\partial x_j} = \frac{1}{2}\frac{u_{i,k+1} - u_{i,k-1}}{\Delta x_j} \; ; \quad \frac{\partial u_i}{\partial t} = \frac{1}{2}\frac{u_{i,l+1} - u_{i,l-1}}{\Delta t} \tag{5.11}$$

Where subscript i corresponds to the velocity component being analyzed; subscript j resembles the gradient direction; subscript k corresponds to the bin position; subscript l relates to the phase being analyzed; Δx_j is the distance between the centers of neighbouring cells in the gradient direction and Δt is equal to the time difference between consecutive phase centers.

The decision on whether to use spatio-temporal gradients obtained through ensemble averaging processes (polynomial fits) or by finite differences calculations of Eulerian velocity data is made based on the noise level of the flowfields resulting from their employment. The presence of such numerical errors is assessed through the evaluation of the flow divergence, which given the experimental conditions is expected to be null, with the velocity gradients obtained with such techniques. Examples of the resultant divergence fields are given in Figure 5.22.

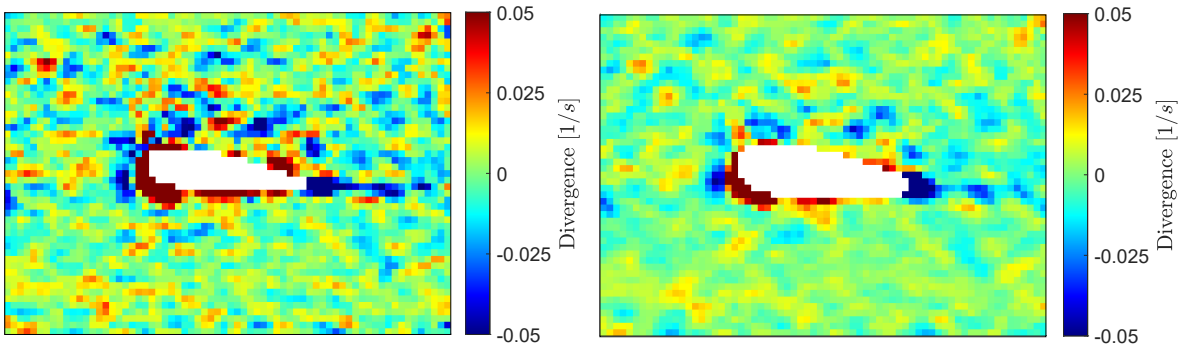

(a) Ensemble averaged (Equation 5.9).

(b) Finite Differences (Equation 5.4).

Figure 5.22: Comparison divergence fields obtained through various gradient determination techniques. Flowfields corresponding to Static Case 1 ($\alpha_0 = 5°$) at $z = 225$ mm.

As seen in Figure 5.22, with the reference binning parameters employed in this thesis (l_B = 75mm and 75% overlap between neighbouring interrogation windows), numerical errors encountered in velocity gradients acquired with polynomial fits (Figure 5.22a) are greater than those existing in gradients obtained through finite differences calculations of the mean velocity vectors (Figure 5.22b). The mean values of the divergence error magnitudes are $\epsilon_{div} \approx 14 \cdot 10^{-3}$ and $\epsilon_{div} \approx 9 \cdot 10^{-3}$ for the divergence fields obtained with polynomial fits and finite differences respectively. Although noise levels described in terms of flow divergence are low for both methods, velocity gradients are calculated implementing the numerical methods described in this section (Equation 5.4) throughout this thesis, as certain improvements with respect to ensemble-averaged quantities are appreciated and the added computational efforts are assumable.

Conversely, as described in Chapter 2, the static pressure at the control volume boundaries is found employing a mixed strategy, similar to that followed in Guissart et al. 2017: the pressure over non-rotational inviscid regions is obtained with an extended formulation of Bernoulli's equation (Equation 2.6) and the pressure at the wake region in the downstream boundary is retrieved through the linear integration of the pressure gradient (Equation 2.2). In order to identify the section of the downstream boundary that is occupied by the wake of the wing, a vorticity threshold equal to $0.3 \cdot \omega_{max}$ is used; where ω_{max} corresponds to the maximum vorticity in the flowfield enclosed by the control volume out of the "safety" zone (Figure 5.21). As shown in Figure 5.23, this threshold value exhibits good results in the recognition of the rotational wake region.

As it can be appreciated in Figure 5.24, Bernoulli's equation fails to capture the total pressure losses due to viscous effects, thus overestimating the static pressure across the wake region. This limitation is overcome with the integration of the pressure gradient in this rotational zone. In addition, a linear weighting over the wake region is applied to account for the error of the pressure at the viscous-inviscid interface.

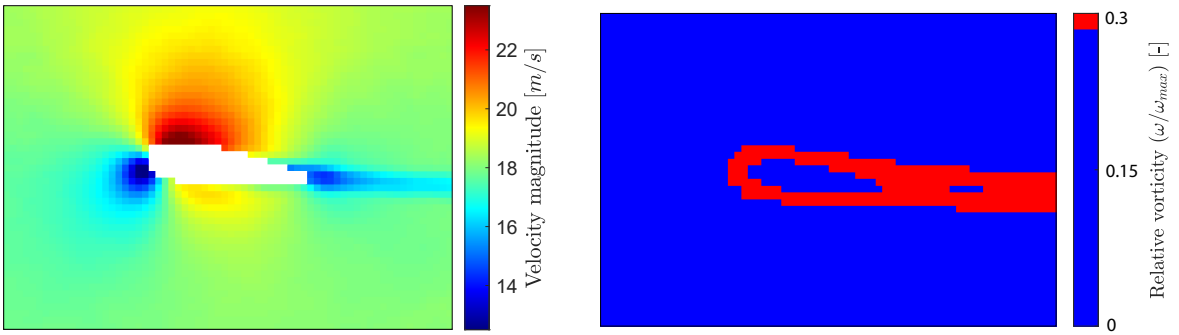

(a) Velocity field.

(b) Relative vorticity field.

Figure 5.23: Wake region identification with a relative vorticity threshold of $0.3 \cdot \omega_{max}$. Flowfields corresponding to Static Case 1 ($\alpha_0 = 5°$) at $z = 225$ mm.

Finally, the last step in the implementation of load determination methods, apart from the obvious execution of the mathematical operations formulated in Chapter 2, is the determination of the origin defining the displacement vector (**x**) in Equation 2.8 and Equation 2.10. Although the resultant aerodynamic forces should be independent of the location of such origins, they depend quite strongly on them in practice. Assuming that the greatest numerical errors appear in regions with strong gradients like the wake, the optimal location of the origin is the closest to these critical zones, as the reduction of the distance $|\mathbf{x}|$ minimizes the contribution of these regions and thus reduces the overall error in the reconstructed forces (Guissart et al. 2017). For this reason, the location of the origin at each spanwise location where sectional loads are retrieved is established at the point inside the control volume and outside the "safety" zone where the vorticity is maximum.

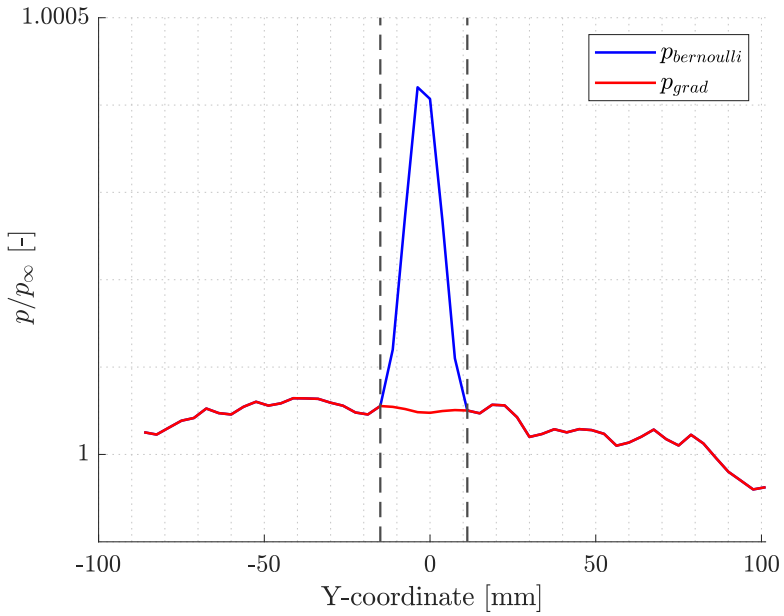

Figure 5.24: Pressure distribution over a control volume downstream boundary. Wake pressure reconstructed through Bernoulli's theorem (blue) and pressure gradient integration (red).

5.5. Force balance data processing

Two different approaches are considered, depending on the inflow conditions (either steady or unsteady), for the processing of the raw balance data.

Regarding static experiments involving steady inflow conditions, four data sets are acquired for every test case (one for each optical measurement volume, as depicted in subsection 4.7.2). This data is merged into a unique data set, which is then processed to obtain the mean aerodynamic forces and moments acting on the test object (Equation 5.12) and their related standard deviations (Equation 5.13).

$$\overline{F_j} = \frac{\sum_{i=1}^{N} F_{j,i}}{N} \tag{5.12}$$

Where $F_{j,i}$ are the force and moment data samples and N the number of data samples.

$$\sigma_{\overline{F_j}} = \frac{\sigma_{F_j}}{\sqrt{n}} = \frac{\sqrt{\frac{\Sigma\left(F_i-\overline{F}\right)^2}{N-1}}}{\sqrt{n}} \tag{5.13}$$

Where σ_{F_j} is the standard deviation of the data sample and n is the number of non-correlated samples included in the data set, which is determined comparing the sampling period t_s (inverse of the sampling frequency f_s) and the flexible wing time scale (t_w) that is established as the time needed by an eddy to travel over the wing surface (one chord length distance).

Considering the freestream velocity at which static test cases are performed in the current experimental investigation (U_∞ = 18.3 m/s), the flexible wing chord (c = 100 mm) and the force balance sampling frequency (f_s = 100 Hz); it is concluded that all force balance data samples are uncorrelated ($n = N$), as $t_w < t_s$ (Equation 5.14), and no further actions should be addressed.

$$t_w = \frac{c}{U_\infty} = \frac{0.1}{18.3} \approx 0.005s < 0.01s = \frac{1}{100} = \frac{1}{f_s} = t_s \tag{5.14}$$

Data outliers in these data samples are identified defining a 95% confidence interval around the mean ($\bar{x} \pm 2 \cdot \sigma$) following an iterative process.

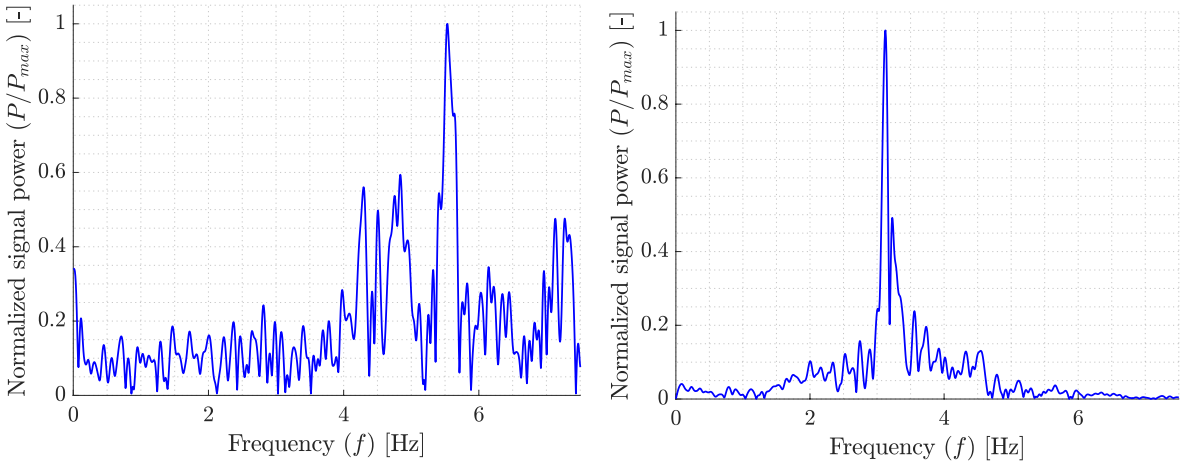

(a) Dynamic Case 1 ($\alpha_0 = 5°$; $\beta = 5°$; f = 5.7 Hz).

(b) Dynamic Case 1 ($\alpha_0 = 10°$; $\beta = 5°$; f = 3.2 Hz).

Figure 5.25: FFT analysis of force balance raw data samples.

On the other hand, concerning test cases involving unsteady inflow conditions in form of controlled gust profiles, several processing stages need to be implemented to define the force signals that are taken as a reference during the assessment of the validity of the aforementioned non-intrusive load determination methods.

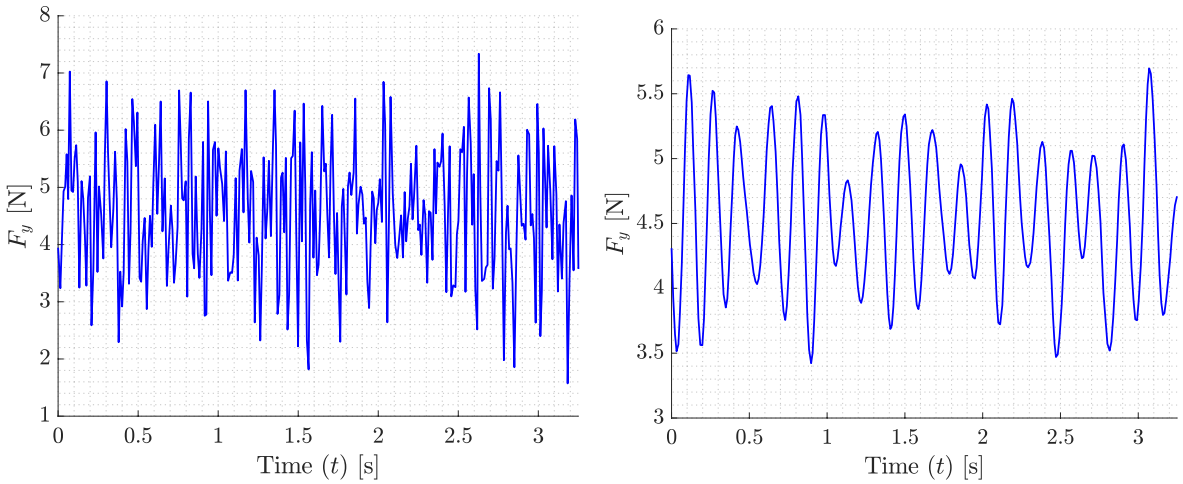

(a) Raw signal.

(b) Low-pass filtered signal.

Figure 5.26: Balance signal filtering. Results corresponding to Dynamic Case 1 ($\alpha_0 = 5°$; $\beta = 5°$; f = 5.7 Hz).

First, all data files acquired during the wind tunnel experimental campaign; 10 for each optical measurement volume with a total number of 20 measurements, as described in Section 4.7.2; must be properly merged into a single sample. To do so, flag signals, which are activated when the optical measurement system (PIV) starts

recording, must be properly identified and isolated. However further preprocessing steps must be taken to minimize the impact of undesired noise in the final reference signal.

The first of such preprocessing steps is the execution of a Fast Fourier Transform (FFT) analysis on the raw data to identify the most dominant frequencies in the spectrum and discard those irrelevant for the current experimental investigation.

As seen in Figure 5.25, the relative weight of the signal power at the vicinity of the excitation frequencies (f = 5.7 Hz and f = 3.2 Hz for Dynamic Case 1 and 2 respectively) with respect to the remaining signal powers is greater in Dynamic Case 2, where the excitation frequency is closer to the frequency of the first bending mode of the flexible wing, than it is in Dynamic Case 1, where the influence of this dominant structural frequency (f_{1st} = 3.2 Hz) in the balance signal can be appreciated.

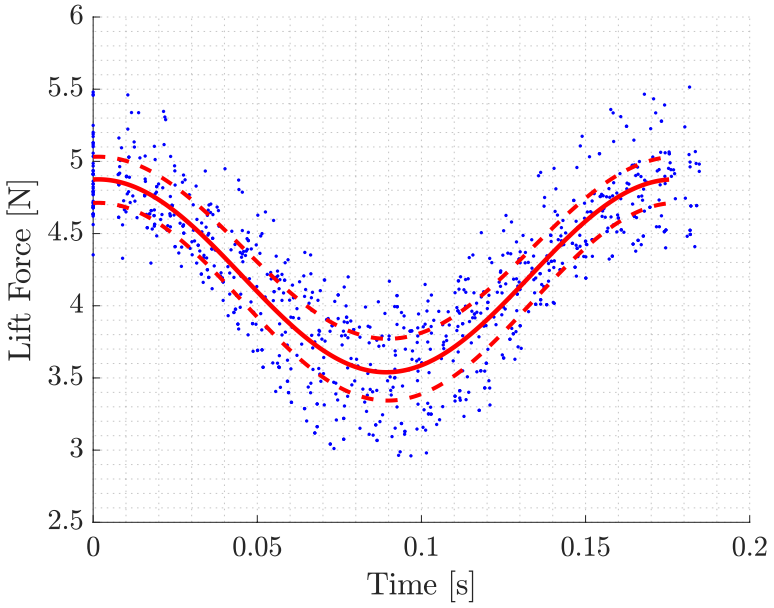

Figure 5.27: Reconstructed reference balance signal. Results corresponding to Dynamic Case 1 ($\alpha_0 = 5°$; $\beta = 5°$; f = 5.7 Hz).

Once the FFT analysis is performed, high-frequency components of the raw data are removed through low-pass filters, in both unsteady test cases, establishing a cutoff frequency 1.5 times greater than the most dominant frequency of the spectrum, which in both cases matches the excitation frequencies. As a result, the balance signal presents appreciable oscillations that were not easily recognizable prior to the implementation of these filters with periods close to those of the gust generator ($T = 1/f_{exc}$), as it can be seen in Figure 5.26.

Finally, the resultant merged and filtered data samples are processed following a similar approach to that implemented during the assessment of the wing motion periodicity and the reconstruction of its motion (Section 5.3.2): samples from consecutive cycles (periods) are merged into a single cycle which is then used to derive the balance force and moment reference signals through non-linear least square regressions, following Equation 5.15.

$$F_{ref}(t) = F_0 + \overline{F}\sin(\omega t + \phi) \tag{5.15}$$

The confidence interval of such fitted reference balance signal, shown in Figure 5.27 as dashed lines, is determined employing Wald's method (Phillips et al. 1988) for statistical parameters with a 95% confidence ($\gamma = 5$). The 95% confidence intervals for the least-square regression coefficients can be expressed as:

$$b_i \pm t_{(0.95/2,n-p)} SE(b_i) \tag{5.16}$$

Where b_i is the coefficient estimate; $SE(b_i)$ its standard error and $t_{(0.95/2,n-p)}$ the 97.5% percentile of t-distribution with $n-p$ DOF, being n the number of observations and p the number of coefficients in the non-linear regression.

On the other hand, relevant changes can also be perceived between the amplitudes of the reference balance measurements and the non-intrusively determined lift loads. The origin of these discrepancies in the force amplitude can be attributed to the influence of inertial loads in the force balance measurements. It is then required to determine the magnitude of these terms to carry out a proper assessment of the accuracy of the load determination methods.

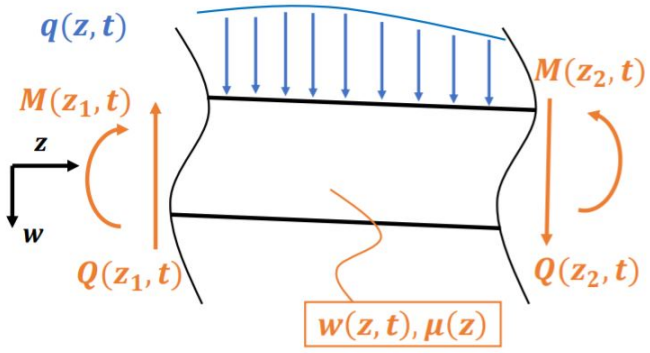

Figure 5.28: Free body diagram of a wing segment. Reproduced from Mertens et al. 2021a

In the present aeroelastic investigation, the dominant motion degree of freedom of the test object is its displacement w in the direction perpendicular to the wing chord line (y-axis). For this reason, the remaining degrees of freedom are neglected and a simplified 1-DOF wing model is employed to determine the contribution of the inertial load. As a result, the sectional inertial loading (f_{in}) can be expressed as the product of the mass density (μ) and the 1-DOF acceleration at each spanwise location z:

$$f_{in}(t) = \mu(z) \cdot \ddot{w}(z,t) \rightarrow F_{in} = \int_0^s \mu(z)\ddot{w}(z,t) \tag{5.17}$$

Where $\mu(z)$ is the spanwise distribution of the model mass density (mass per unit span) and $w(z,t)$ the temporal evolution of its structural deflection along the span in the perpendicular direction.

In order to simplify the processing efforts, a constant mass distribution along the span of the flexible wing is considered $\mu(z) \approx \mu_0$. The weight and height of the bottom solid cylinder (Section 5.3) are not included in the calculation of such mass distribution. The resultant mass per unit span of the highly flexible wing results in:

$$\mu(z) \approx \mu_0 = \frac{m_{wing}}{s} = \frac{0.321}{0.550} = 0.584 kg/m$$

As described previously in Table 4.3 Section 5.3, the periodic inflow conditions employed in these test cases result in sinusoidal structural dynamics that follow Equation 5.2 (wing displacement). Thus, the second temporal derivative of the wing displacement (wing acceleration) is expressed as:

$$\ddot{y}(t) = -A \cdot \omega^2 \sin(\omega t + \phi) \rightarrow \ddot{w}(z,t) = -A(z) \cdot \omega^2 \sin(\omega t + \phi) \tag{5.18}$$

The temporal evolution of the spanwise wing acceleration given by Equation 5.18 is obtained performing a sinusoidal fit of the markers location, as depicted in Section 5.3. The magnitude of the sectional inertial load $f_{in}(t)$ is then easily obtained following Equation 5.17.

Once the magnitude of the inertial loading over the flexible wing span due to its acceleration is determined, the force balance measurements can be corrected to isolate the reference aerodynamic lift signal and perform an appropriate comparison with those obtained through the proposed non-intrusive load determina-

tion methods. According to Collar 1946, the aerodynamic (F_{aero}), elastic (F_{el}) and inertial (F_{in}) loads experienced by the test object define an equilibrium condition formulated in Equation 5.19. A free body diagram (Figure 5.28) is employed to illustrate the equilibrium of forces in a given wing segment.

$$\int_{z_1}^{z_2} \mu(z)\ddot{w}(z,t)dz = \int_{z_1}^{z_2} q(z,t)dz + (-Q(z_1,t) + Q(z_2,t)) \rightarrow F_{aero} + F_{el} - F_{in} = 0 \rightarrow F_{aero} = -F_{el} + F_{in} \tag{5.19}$$

Following Equation 5.19, corrected balance measurements (aerodynamic loads), which are employed to assess the performance of the load determination methods, can be obtained from the correction of the original force balance measurements as:

$$F_{aero} = -F_{el} + F_{in} = -F_{el} + \int_0^s \mu(z)\ddot{w}(z,t) \tag{5.20}$$

The reference signals (balance measurements) of each of the 3 force contributors involved in the aeroelastic phenomena being investigated (Figure 1.2) are shown in Figure 5.29. As expected due to the lightness of the test model, the contribution of the aerodynamic forces (F_{aero}) to the aeroelastic phenomena is greater than that of the inertial loading (F_{in}). Nevertheless, its impact in the original force balance measurement is considerable, as it can be clearly seen in Figure 5.29.

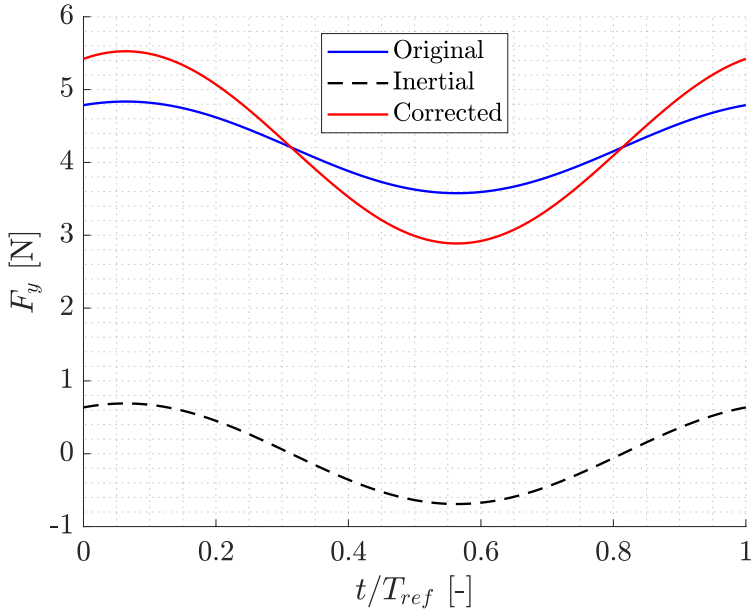

Figure 5.29: Original balance force; reconstructed inertial load and corrected balance force signals. Results corresponding to Dynamic Case 1 ($\alpha_0 = 5°$; $\beta = 5°$; f = 5.7 Hz).

6

Results

This chapter presents the results obtained implementing the mathematical expressions enumerated in Chapter 2 and the processing strategies described in Chapter 5 to raw LPT data acquired with the experimental procedures depicted in Chapter 4. These results provide the basis to answer the research questions formulated in Section 3.5.

The discussion of the results begins by analyzing the impact of different setup parameters, such as the spatial discretization of the Eulerian flowfield, the location of control volume boundaries, the presence of random numerical error (noise) or the particle concentration; in the forces reconstructed at certain spanwise locations (Section 6.1). Then, in Section 6.2.2, the spanwise evolution of aerodynamic loads over the test object is analyzed and compared to theoretical lift distributions in unswept rigid wings. In addition, integral results are compared to reference force balance readings to assess the validity of the load determination methods under steady inflow conditions. Finally, in Section 6.3.2, the temporal evolution of phase-averaged sectional loads is compared to theoretical models to investigate the capability of the proposed load determination methods to account for the impact of unsteady effects. Moreover, integral phase-averaged forces across the period are compared to reference force balance measurements.

6.1. Sensitivity analysis

In this section, an analysis of the sensitivity of the load determination methods to various parameters is performed. Such study is conducted on sectional data obtained with the processing steps described in previous chapters.

6.1.1. Control volume shape and size

Concerning the sensitivity of the proposed load determination methods to the shape and size of the control volumes employed during their implementation, its analysis is focused on the changes that the reconstructed sectional lift forces suffer when certain boundaries are displaced from their reference position. These changes are studied in terms of load magnitude differences in static test cases and amplitude and phase deviations in test cases involving gust encounters (dynamic test cases). The position of the control volume limits used throughout the study is defined by means of their distance to the surface of the flexible wing (similar to Figure 5.21). The distance to the wing surface from every boundary of the reference control volume is established at $d_{CV} = 0.4{\cdot}c$ during test cases involving steady inflow conditions (static test cases) and at $d_{CV} = 0.5{\cdot}c$ for analysis including gust encounters (dynamic test cases). Reference results from where comparisons are executed are defined for each load determination method at this reference control volume configuration ($d_{CV} = 0.4 \cdot c$).

In order to reduce the processing efforts, this sensitivity analysis is only conducted on one static test case (Static Case 2, Table 4.3) and on one dynamic test case (Dynamic Case 1, Table 4.3). The latter is chosen due to its greater flow unsteadiness ($k \approx 0.1$), compared to Dynamic Case 2 (Table 4.3). The control volume boundaries used for the study are located at a distance within 5 mm and 85 mm from the airfoil surface. The distance between neighbouring control volume boundaries is fixed at 3.75 mm (one grid cell).

Five different situations are analyzed for each inflow state (static and dynamic): all boundaries moving away from the wing surface at the same time and a single boundary (upstream, downstream, pressure and suction sides) being modified while the others remain fixed at their reference position ($d_{CV} = 0.4 \cdot c$ in static test cases and $d_{CV} = 0.5 \cdot c$ in dynamic test cases). An example of the distribution of these control volume boundaries is given in Figure 6.1.

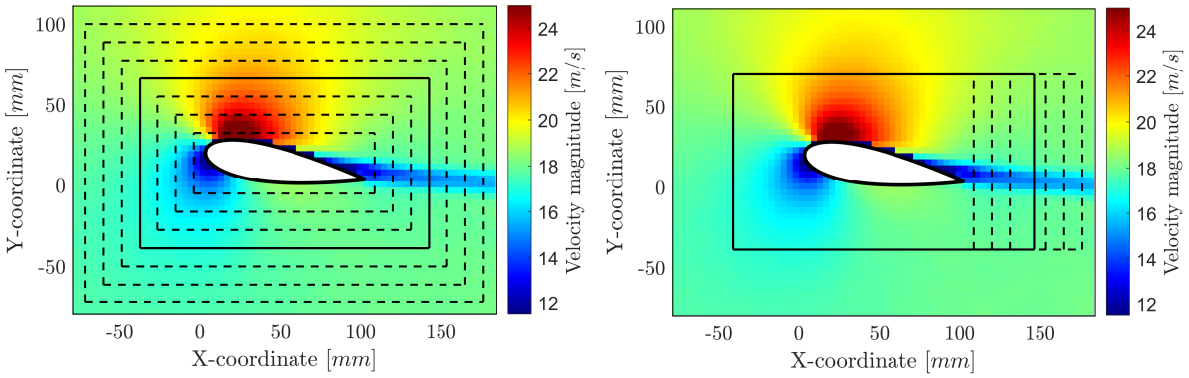

(a) Displacement of all boundaries.

(b) Displacement of downstream boundary.

Figure 6.1: Control volume configurations during the sensitivity analysis of their size and shape. Flowfields corresponding to Static Case 2 ($\alpha_0 = 10°$) at $z = 150$ mm. Reference control volume (black line); alternative control volumes (black dashed-line).

Static cases

Regarding the influence of the relative position of the control volume limits on the reconstructed aerodynamic loads in test cases involving steady inflow conditions, similar trends can be recognized in Figure 6.2 for all control volume modifications and load determination methods.

The first phenomenon that can be appreciated in Figure 6.2 is the growth in the deviation of the magnitude of the reconstructed sectional lift force as the boundaries of the control volumes are brought closer to the wing surface. This behaviour can be attributed to increases in flow data error at the vicinity of the test object due to limitations in the experimental setup and the flowfield reconstruction procedures. However, it can also be perceived that these disparities dissipate once the distance of the control volume limits to the test object surface reaches a certain value. From the results observed in Figure 6.2, this minimum distance required to assume a negligible impact of the position of the control volume boundaries is established at $d_{min} = 0.2 \cdot c$. Sectional lift forces obtained through control volumes whose boundaries are distanced more than d_{min} show deviations to the reference force below a 1% of its magnitude.

In addition, it is also appreciable that the reconstructed sectional lift forces are more affected when control volume boundaries at the pressure and suction sides (Figure 6.2c and Figure 6.2d) are modified than when upstream and downstream limits change their position (Figure 6.2a and Figure 6.2b). This greater impact is more visible at the closest region to the wing surface ($d_{min} < 0.2 \cdot c$), where greater deviations in the aerodynamic loads appear. This conduct is explained by the fact that flow quantities at the pressure and suction boundaries of the control volume have a prominent contribution to the overall sectional lift force, arising from the orientation of the unitary vectors in the mathematical expressions described in Chapter 2.

From these results, the following conclusions on the sensitivity of the load determination methods to the location of the control volume boundaries during static test cases can be extracted:

- All load determination methods show the same reaction to the positioning of the control volume limits.
- Control volume limits should not be closer than $d_{min} = 0.2 \cdot c$ to any point in the wing surface.
- As sectional lift forces show negligible variations ($\epsilon_{cl} < 0.01 \cdot cl_{ref}$) when $d > d_{min}$; loads resulting from all control volumes are averaged to minimize the impact of random error in the Eulerian flowfield.

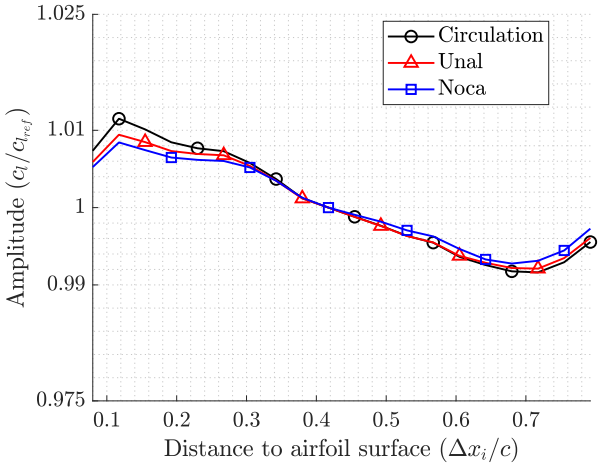

(a) Upstream boundaries.

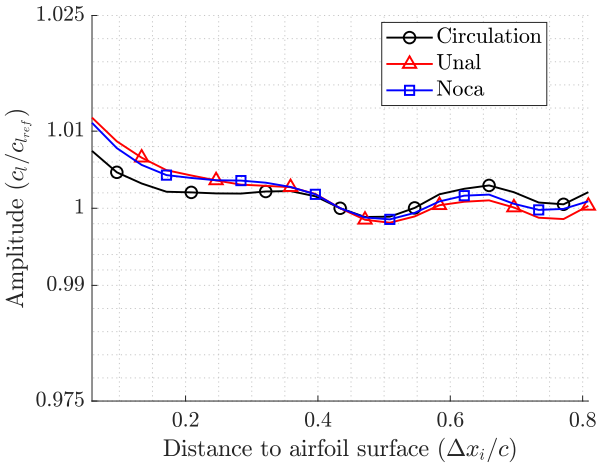

(b) Downstream boundaries.

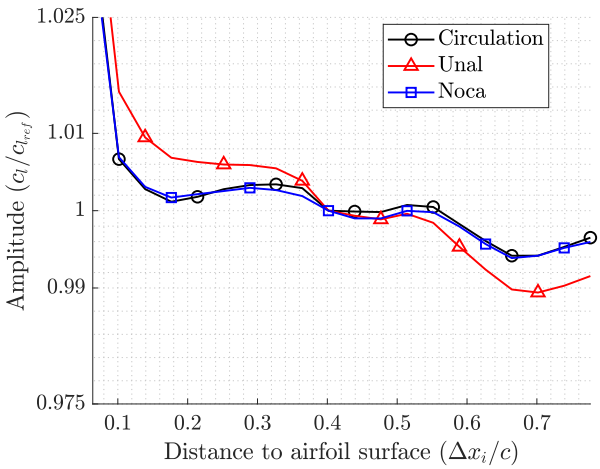

(c) Pressure side boundaries.

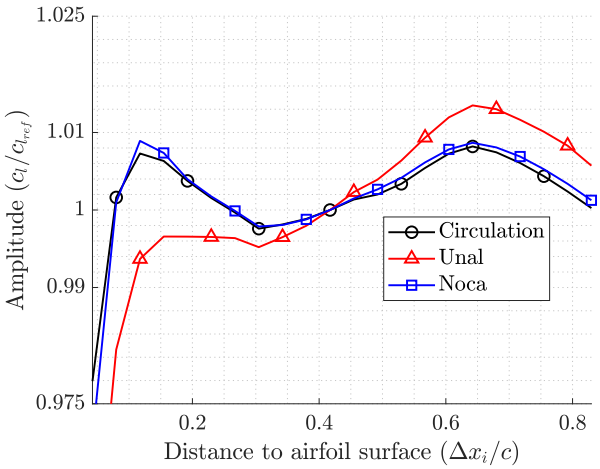

(d) Suction side boundaries.

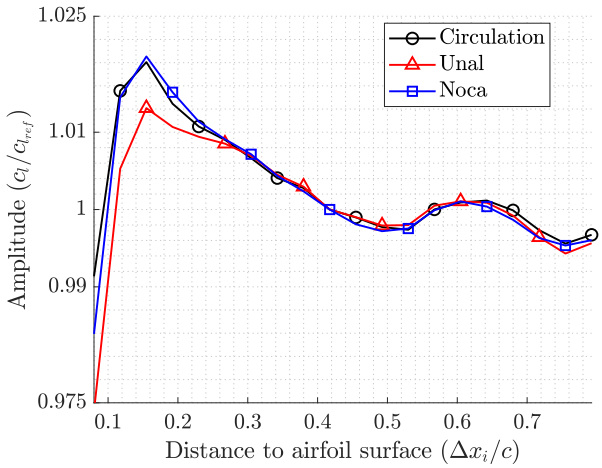

(e) All boundaries.

Figure 6.2: Sensitivity of the load determination methods to the location of control volume boundaries. Results corresponding to Static Case 2 ($\alpha_0 = 10°$) at $z = 150$ mm.

Up to this point, the analysis has focused on the variation of sectional lift forces employing an integral perspective. However, to complement this information, the evolution of the different terms involved in the obtainment of integral loads with the displacement of control volume boundaries is examined below. The aim of this analysis is the assessment of the impact of possible numerical errors associated with the obtainment of aerodynamic loads in the final solution. Neither unsteady terms nor viscous contributions in Equation 2.1 and Equation 2.10 are considered during this experimental investigation, as flow steadiness is assumed during all static test cases (Table 4.3) and viscous terms are neglected in the implementation of the aforementioned load determination methods, as stated in Chapter 2, due to the weight of their contribution to the overall lift force.

In order to reduce the amount of information shown in this document, the terms corresponding to the classical formulation of the integral momentum conservation equation (Equation 2.1) are the only ones shown. Nevertheless, the trends observed in these terms (convective and pressure) are equivalent to those recognized in the terms (convective and vorticity moment) of the alternative formulation of the momentum conservation equation (Noca's/vorticity formulation, Equation 2.10). Results corresponding to modifications in single control volume boundaries (upstream, downstream, suction and pressure control volume limits) are provided.

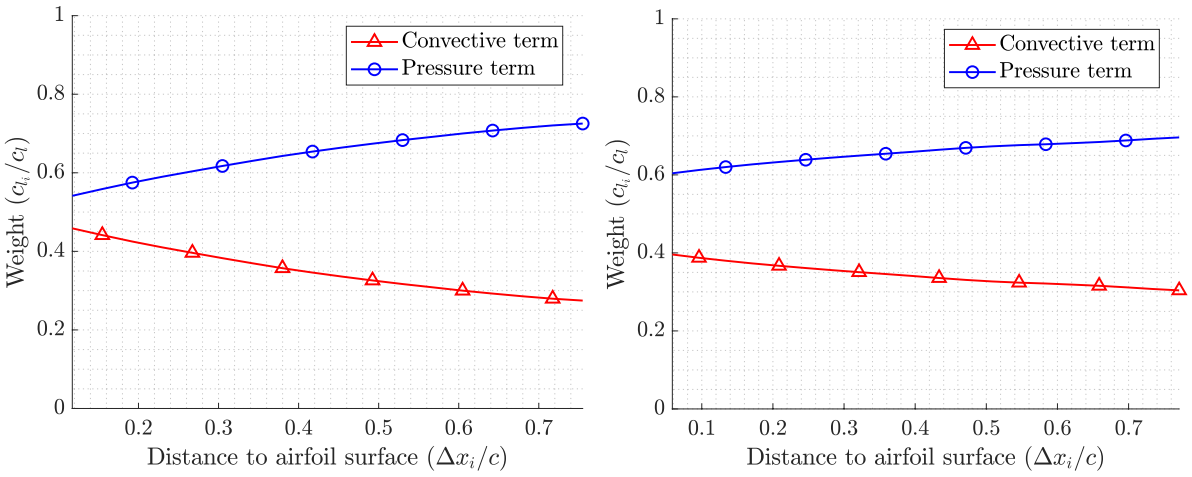

(a) Upstream boundary.

(b) Downstream side boundary.

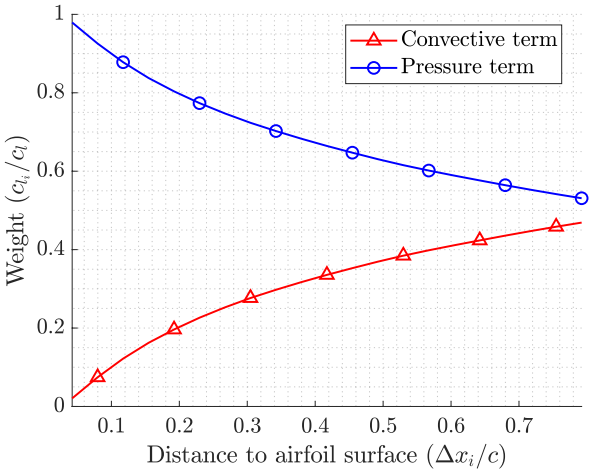

(c) Suction boundary.

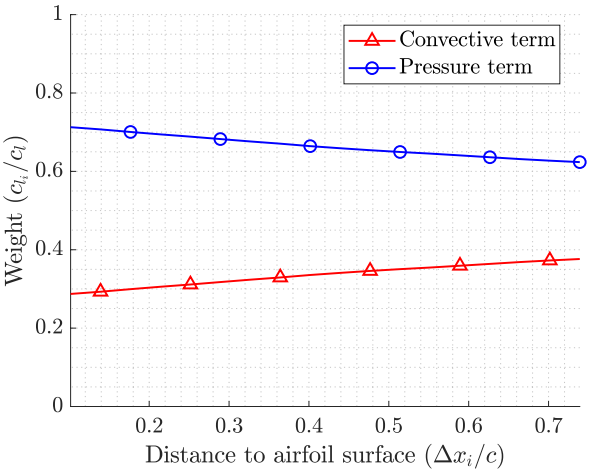

(d) Pressure side boundary.

Figure 6.3: Analysis of the contribution of each term in the momentum conservation methods for different shape and sizes of the control volumes employed in their implementation. Results corresponding to Static Case 2 ($\alpha_0 = 10°$) at $z = 150$ mm.

As seen in Figure 6.3, pressure and convective (vorticity moment) terms in Equation 2.1 and Equation 2.10 follow opposite trends when upstream/downstream and suction/pressure control volume boundaries are modified. On the one hand, regarding displacements in the upstream/downstream limits (Figure 6.3a), the weight of the convective term decreases, while the importance of the pressure term increases, as the distance of the control volume boundary to the wing surface grows. On the contrary, when suction/pressure boundaries are moved away from the test object, the contribution of convective terms rises, whereas pressure terms decrease. Besides, as also observed in Figure 6.3, displacements in the suction control volume boundary provide the greatest alterations in the weight of each of the terms in the momentum conservation equation. The trends observed in the evolution of the weight of each term due to modifications in the location of the control volume boundaries resemble those observed in previous studies like Mohebbian et al. 2012.

Dynamic cases

Concerning the impact of the relative location of the control volume boundaries on the reconstructed lift forces during test cases implying gust encounters (Dynamic Cases Table 4.3), two main aspects are analyzed: On the one hand, variations in the amplitude of the lift oscillations caused by modifications in the control volume limits. On the other hand, phase lag differences between sectional lift coefficients resulting from various control volume configurations. Both phenomena are studied through sinusoidal fits of the phased-averaged results. In addition, the distance from every boundary of the reference control volume to the surface of the test model is established at $d_{CV} = 0.5 \cdot c$. A reference lift force is defined at this control volume configuration for each load determination method. Results of this analysis are given in Figure 6.4.

With regard to the changes detected in the amplitude of the sinusoidal signal (left column in Figure 6.4) when control volume boundaries are modified, trends similar to those encountered during the sensitivity analysis of the shape and size of the control volumes during static test cases are appreciated: A clear growth in the deviation to the baseline measurement of the lift signal amplitude is recognized as the distance from the control volume boundaries to the wing surface decreases. This phenomenon occurs for all load determination methods independently of the control volume limit being displaced. Nevertheless, as happened for static test cases, such deviations are bounded and show small magnitudes until boundaries are brought closer than $d_{min} \approx 0.2 \cdot c$. There, errors in the amplitudes of the sinusoidal fitted lift signals reach values of more than 5% for all load determination methods, exhibiting the greatest deviations for changes in the streamwise (upstream/downstream) control volume boundaries (up to 7.5% at $d_{CV} \approx 0.05 \cdot c$). However, results obtained with control volume boundaries with $d_{CV} > d_{min}$ show discrepancies to the reference force amplitude below 2.5% of its magnitude, independently of the boundary being modified and the load determination technique employed. Although this value if greater than that attained during the sensitivity analysis of static test cases ($\epsilon < 1\%$), it is still acceptable for the purposes of this thesis.

Besides, modifications in the phase of the sinusoidal lift signal, which are expressed in terms of the non-dimensionalized time lag to the baseline lift coefficient ($\tau' = \tau / T$), are also shown in Figure 6.4 (right column). Linear fits (solid lines) of the measured time lags and their expected theoretical values (dashed lines) are included to obtain a better understanding of the trends of the results. These theoretical values are equal to zero for all methods and control volume configurations except for the circulation (Kutta) theorem when changes in the downstream limit of the integration path occur. The unsteady wake of the wing contains the history of the shed vorticity, so that a shift in the phase of the reconstructed lift force appears if the size of the wake region enclosed by the control volume changes. For this reason, the magnitude of the theoretical time lag for the Kutta-Joukowski theorem during downstream boundary displacements is $\tau = (x - x_0)/U_\infty$; where x is the position of the downstream boundary, x_0 the location of the reference downstream limit and U_∞ is the freestream velocity at which the vorticity in the wake is shed.

Various systematic effects of the position of the control volume boundaries in the signal of the sectional lift are appreciated when the linear fit of the results is analyzed: First, it is observed that the greatest differences in the phase of the signal appear when the limits being modified pertain to regions with greater spatio-temporal gradients (downstream and suction boundaries). Secondly, it is detected that the lowest deviations to the theoretical lag are obtained when the Kutta-Joukowski theorem is employed to reconstruct the phase-averaged sectional lift coefficient for all control volume modifications. On the contrary, temporal information in load determination methods involving evaluations of the momentum conservation equation, show greater sensitivity to the location of the control volume boundaries, reaching errors of about 3%.

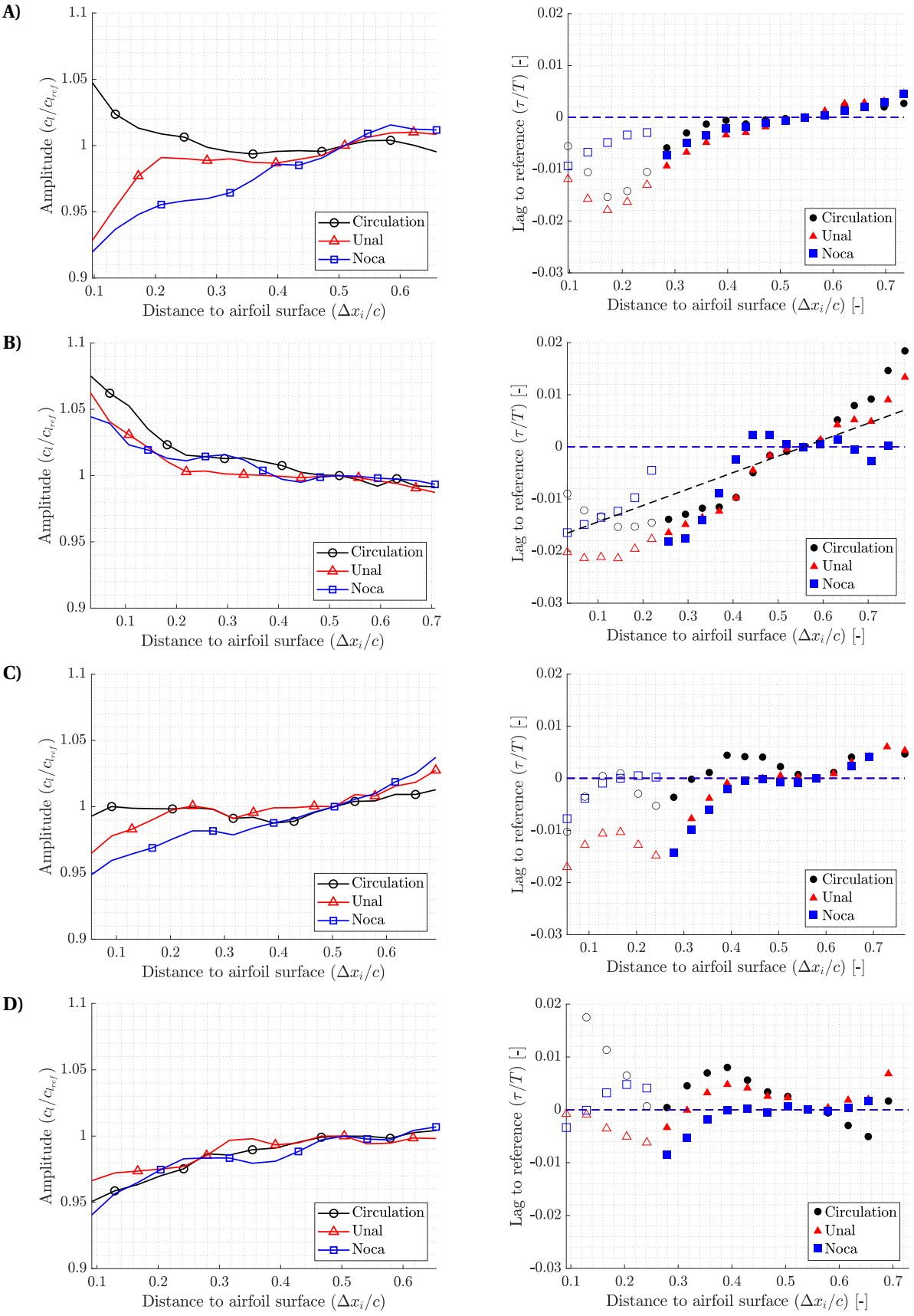

Figure 6.4: Sensitivity of the reconstructed sectional lift coefficient to the position of the (**A**) upstream, (**B**) downstream, (**C**) suction side and (**D**) pressure side boundaries of the control volume. *Right column*: Sensitivity of the signal amplitude; *Left column*: Sensitivity of the signal phase (Dashed lines representing expected values). Results corresponding to Dynamic Case 1 ($\alpha_0 = 5°$; $\beta = 5°$; f = 5.7 Hz) at $z = 150$ mm.

These differences in the sensitivity of the load determination methods might be attributed to numerical errors included in the determination of flow acceleration fields ($\partial u/\partial t$) from the mean velocity data.

Nevertheless, if discrete time-lag measurements (non-fitted results) are considered, it can be observed that the greatest difference in the signal phase of results pertaining to the same control volume modification (upstream, downstream, suction side or pressure side) is less than 2.5% of the signal period, which approximately corresponds to a 1.5% time lag with respect to the results obtained with the reference control volume setup.

Taking both the amplitude variation and the time lag results under consideration, the following conclusions on the sensitivity of the load determination methods to the location of the control volume boundaries during dynamic test cases can be extracted:

- Control volume limits should not be closer than $d_{min} = 0.2 \cdot c$ to any point in the wing surface to avoid undesired variations in the signal amplitude.
- Momentum conservation approaches (both Unal and Noca formulations) show greater sensitivity to the location of the control volume limits when the temporal character of the results (time-lag, right column in Figure 6.4) is considered.
- It is advisable to average the resultant lift coefficients to minimize the impact of random numerical data errors.

6.1.2. Spatial discretization

The sensitivity of the sectional lift force to the spatial discretization of the reconstructed flowfield is assessed on experimental test cases involving steady inflow conditions (Table 4.3) where structural staticity is assumed. This decision is made based on the greater particle concentrations that can be achieved in time-averaged flowfields (static cases) compared to those attained in phase-averaged ones (dynamic cases). This greater information density permits the ensemble average of Lagrangian particle data employing very small interrogation windows while maintaining the minimum concentration requirements established in Section 5.3.3 ($N_{p,min} = 35$). Throughout the spatial discretization analysis, the overlap between neighbouring bins is fixed at 75%, while the size of the interrogation windows covers from $l_B = 5$ mm to $l_B = 20$ mm (5 – 20% of the chord-length), resulting in grid cell sizes ranging from $l_C = 1.25$ mm to $l_C = 5$ mm. The velocity fields resulting from the polynomial fit of particle tracks employing these limit bin sizes are shown in Figure 6.5.

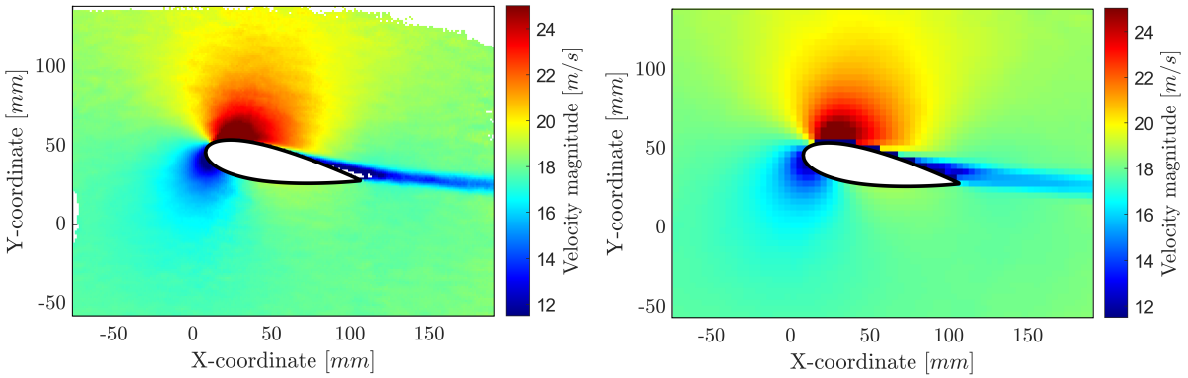

(a) Bin size $l_B = 5$ mm.

(b) Bin size $l_B = 15$ mm (Reference).

Figure 6.5: Velocity fields corresponding to Static Case 2 ($\alpha_0 = 10°$) at $z = 300$ mm for different spatial discretizations.

The achievement of greater spatial discretizations supposes the ensemble average of particles in smaller interrogation windows, which minimizes the diffusion of velocity deviations and uncertainties arising from measurement and numerical errors. This increase in the noise level of the velocity data across the entire measurement volume in flowfields with high spatial discretizations (small interrogation windows) can be appreciated in Figure 6.5.

In addition, as described in Section 5.4, spatial gradients are obtained through second-degree first-order finite-difference methods (Equation 5.4) in this thesis. These gradients are computed within shorter distances in cartesian grids with a larger number of cells, which magnifies the effect of the aforementioned velocity deviations in the resultant gradients, than in Eulerian grids with larger cell sizes. As a consequence, the numerical errors in velocity gradients on highly discretized flowfields are greater than that attained in Eulerian data sets employing larger bin sizes.

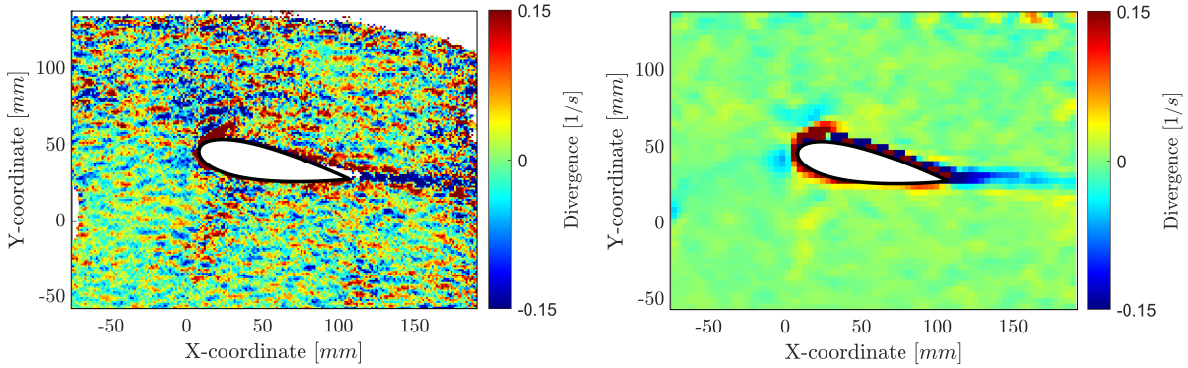

(a) Bin size l_B = 5 mm.

(b) Bin size l_B = 15 mm (Reference).

Figure 6.6: Divergence fields corresponding to Static Case 2 ($\alpha_0 = 10°$) at z = 300 mm for various bin sizes.

This raise in the data noise is clearly recognized when the flow divergence is assessed: although the freestream velocity employed during the experimental campaign ($U_\infty \approx 18.3$ m/s) supposes the obtainment of incompressible conditions at the test section, the actual divergence of the reconstructed Eulerian flowfields is non-null at regions where deviations in the velocity gradients appear ($\nabla u = \partial_i u_i \neq 0$). As seen in Figure 6.6, the presence of gradients data noise displayed in terms of the flow divergence is greater at the highly discretized flowfield (Figure 6.6a) than at the Eulerian field obtained with bigger interrogation windows (Figure 6.6b).

However, non-divergence free regions can still be found around the wing surface (inside the "safety" region described in Section 5.4) when larger bin sizes are employed. For this reason, this zone is avoided in all the calculations performed in this thesis, as already described in the preceding sections.

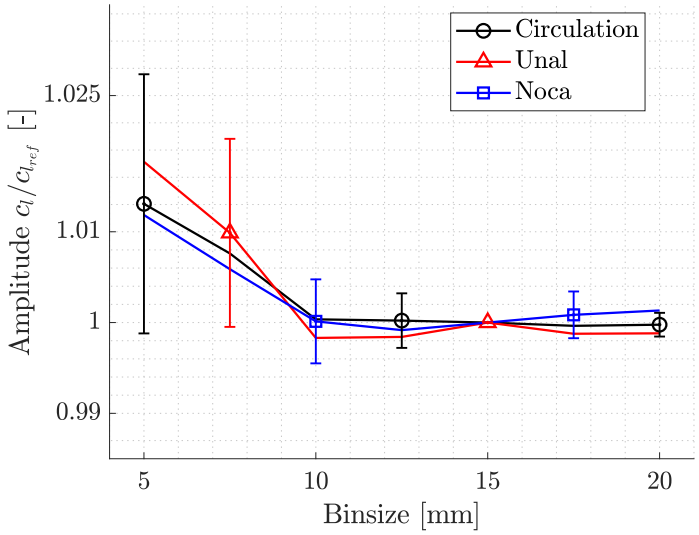

Figure 6.7: Sensitivity of the load determination methods to the flowfield spatial discretization in terms of the sectional lift force variation. Results corresponding to Static Case 2 ($\alpha_0 = 10°$) at z = 300 mm.

As mentioned previously, the analysis of the sensitivity of the proposed load determination methods (Chapter 2) to the spatial discretization of the flowfield is performed through the comparison of aerodynamic loads resulting from flowfields obtained with various bin sizes. These forces arise from the averaging of loads acquired with control volumes with different shapes and sizes. The boundaries of the control volumes employed for the obtainment of averaged forces are distributed in every direction from the limits of the "safety" region ($d_{gap} = 0.15 \cdot c$, Figure 5.21) to the limits of the sectional Field of View. The spacing between consecutive control volume boundaries is fixed at $\Delta x = 3.75$ mm, which corresponds to the size of the cells at cartesian grids obtained with interrogation windows of $l_B = 15$mm (reference bin size during this experimental investigation). A schematic of the distribution of these control volume boundaries is given in Figure 6.1a.

As seen in Figure 6.7, the mean value of the sectional lift, which results from the averaging of aerodynamic forces obtained through different control volumes, shows small deviations to the reference results (one for each load determination method; $l_B = 15$ mm) when changes in the size of cartesian grid cells occur. These deviations to the baseline force remain below a 1.5% of its magnitude for all load determination methods and bin sizes, reaching their maximum at $l_B = 5$ mm. Nevertheless, although the mean values of the lift force present limited sensitivity to the spatial discretization of the flowfield, its standard deviation exhibits an increasing trend as the interrogation windows employed in the ensemble averaging process become smaller. This increment in the standard deviation of the reconstructed loads leads to confidence intervals in the relative magnitude of the lift coefficient (cl_i/cl_{ref}) of more than a 2.5% of the reference lift force when interrogation windows of less than $l_B = 7.5$ mm are employed.

From these results, it can be concluded that all proposed load determination methods show similar sensitivities to the spatial discretization of the flowfield. Moreover, it is deducted that small bins ($l_B < 7.5$ mm) should be avoided in order to minimize the impact of data error and noise in the resultant aerodynamic loads.
Apart from the trends observed in Figure 6.7 concerning the sensitivity of the methods to the spatial discretization of the flowfield, other phenomena have to be considered to select an adequate size of the interrogation windows employed during the ensemble averaging process. Among these additional limitations, the most relevant is the presence of data gaps resulting from the incapability of certain interrogation windows to meet the concentration requirements ($N_{p,min} = 35$) stated in Section 5.3.3. In order to minimize the number of data gaps present in the reconstructed flowfield while maintaining acceptable spatial discretizations during all cases of study (Table 4.3), the size of the interrogation windows employed in this thesis for the ensemble averaging of the Lagrangian data is established at $l_B = 15$ mm.

6.1.3. Random noise

Regarding the sensitivity of the load determination methods to random numerical errors distributed across the measurement volume, the analysis focuses on the changes that sectional lift experiences with various data noise levels. The inclusion of these modifications is conducted on ensemble-averaged velocity fields after Lagrangian particle tracks are transformed into Eulerian descriptions over cartesian grids. Such velocity deviations are distributed following a continuous uniform probability distribution. The resultant velocity vector field is obtained at each of the nodes of the cartesian grid through the expression $u_i' = u_i \pm \epsilon$.

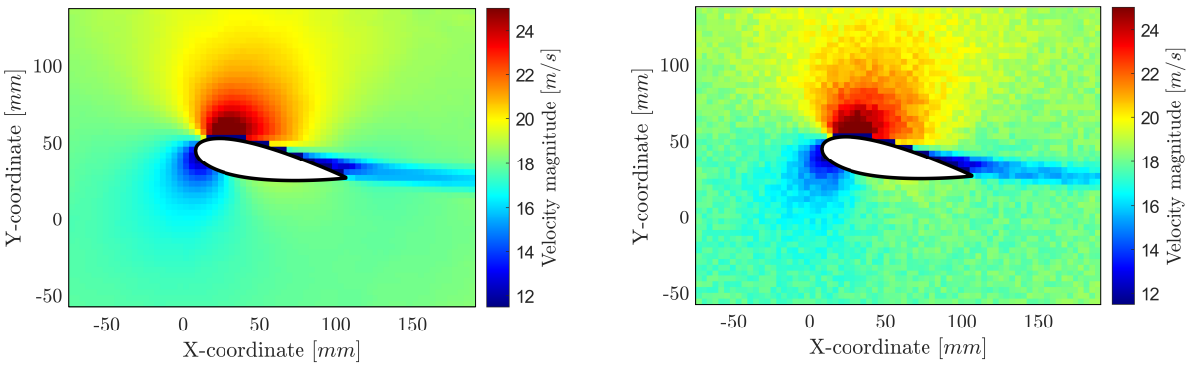

(a) Noise level $\sigma_u = 0$ (Reference).

(b) Noise level $\sigma_u = 5$.

Figure 6.8: Velocity fields corresponding to Static Case 2 ($\alpha_0 = 10°$) at $z = 300$ mm with different noise levels.

The magnitude of the numerical error (ϵ) at each grid node can reach values up to $\sigma_u \cdot u_{i_{mean}}$; where σ_u is the noise level (percentage) employed during the modifications of the original data and $u_{i_{mean}}$ is the mean value of each freestream velocity component at a given spanwise location. In the present sensitivity analysis, the noise level goes from σ_u = 0% (original velocity data) to σ_u = 5%. An example of the velocity flowfields resulting from the addition of random numerical errors to the original Eulerian data is given in Figure 6.8, while the corresponding divergence fields are shown in Figure 6.9.

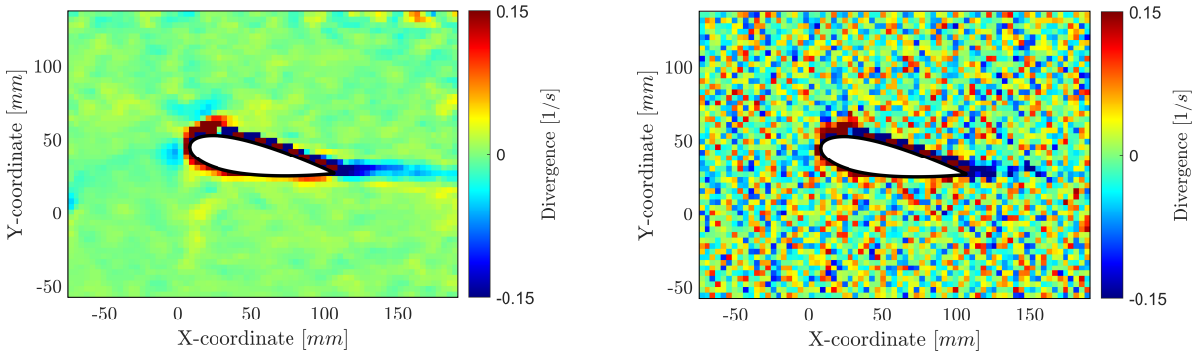

(a) Noise level σ_u = 0 (Reference).

(b) Noise level σ_u = 5.

Figure 6.9: Divergence fields corresponding to Static Case 2 ($\alpha_0 = 10°$) at z = 300 mm with different noise levels.

In addition, once the original velocity fields are modified by including random numerical errors at each node of the cartesian grid, the remaining flow quantities needed in the implementation of the load determination methods (spatio-temporal velocity gradients, vorticity, pressure...) are recalculated to account for the deviation with respect to their original magnitudes in the final reconstructed force. Once again, the execution of this sensitivity analysis is limited to test cases involving steady inflow conditions, specifically Static Case 2, where greater structural deflections are expected (Table 4.3).

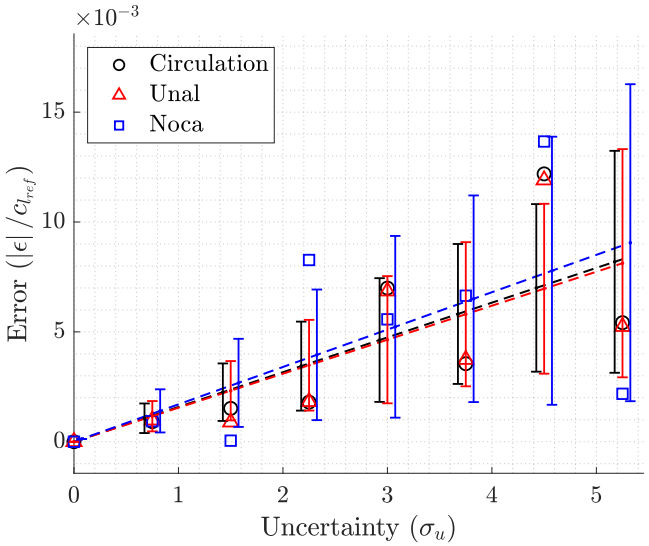

Figure 6.10: Sensitivity of the load determination methods to the flowfield noise level in terms of the sectional lift force variation. Results corresponding to Static Case 2 ($\alpha_0 = 10°$) at z = 300 mm.

The final value of the sectional lift force employed to analyze the sensitivity to the data noise level results from the averaging of loads acquired with various control volumes. The location of the boundaries of these control volumes is similar to that employed during the analysis of the sensitivity to the spatial discretization of the flow (Section 6.1.2): they are allocated between the limits of the "safety" region ($d_{gap} = 0.15 \cdot c$) and the limits of the sectional FOV with a constant spacing of Δx = 3.75 mm between neighbouring boundaries (Fig-

ure 6.1a). Furthermore, the noise implementation procedures and the subsequent reconstruction of loads is repeated iteratively 250 times to guarantee the randomness in the distribution of the data noise. These forces are also included in the averaging process to obtain the final sectional lift employed in the sensitivity analysis.

It can be noticed, in Figure 6.10, that none of the sectional lift forces presents strong deviations to the baseline lift ($\sigma_u = 0\%$) when random numerical errors are introduced into the original velocity data. In addition, it is also appreciated that this behaviour of the reconstructed loads is independent of the technique employed in their obtainment. The reason why these deviations are so small (< 1%), indistinctly of the data noise level, lies in the fact that the proposed load reconstruction techniques employ integral operations, which tend to cancel the deviations introduced by randomly distributed random numerical errors. Although it might seem that these findings oppose those encountered during the analysis of the spatial discretization sensitivity, the distribution of the data noise arising from spatial discretization issues is not completely random, so the changes in sectional lift forces when very small interrogations windows are employed have to be considered.

6.1.4. Particle concentration

In this section, the sensitivity of the load reconstruction techniques to the concentration of particles is assessed employing PIV data from Static Case 2 (Table 4.3). The objective of such analysis is the identification of the capabilities of these methods to acquire instantaneous aerodynamic forces when experimental setups similar to that used in this thesis are employed. For this purpose, the original number of images contained in the PIV measurements (5457 images) is reduced gradually until a minimum of 50 images is reached. Moreover, the concentration requirements established in Section 5.3.3 are reduced to $N_{p,min} = 5$ to avoid an exponential increase in the number of data gaps.

Nevertheless, with the aim of providing information that can be generalized and employed in future investigations, this shortening in the acquisition time is expressed by means of the particle concentration attained at the section under study. The particle concentrations corresponding to the entire acquisition time (5457 images) and to ≈ 1% of it (50 images) during Static Case 2 at z = 300 mm are 3600 particles/cm^3 and 40 particles/cm^3 respectively. Velocity and divergence fields corresponding to both limit particle concentrations are shown in Figure 6.12.

Contrary to what it is observed when numerical errors are randomly distributed across the measurement volume (Figure 6.8), velocity fluctuations caused by a reduction in the number of particles tend to concentrate in small areas where the noise intensity is similar, as it can be appreciated in Figure 6.12c. This lack of randomness in the arrangement of the numerical error is what causes the differences in the reconstructed lift forces when very low particle concentrations are employed, similarly to what occurs when small interrogation windows are used to obtain Eulerian descriptions of the flow (see Section 6.1.2).

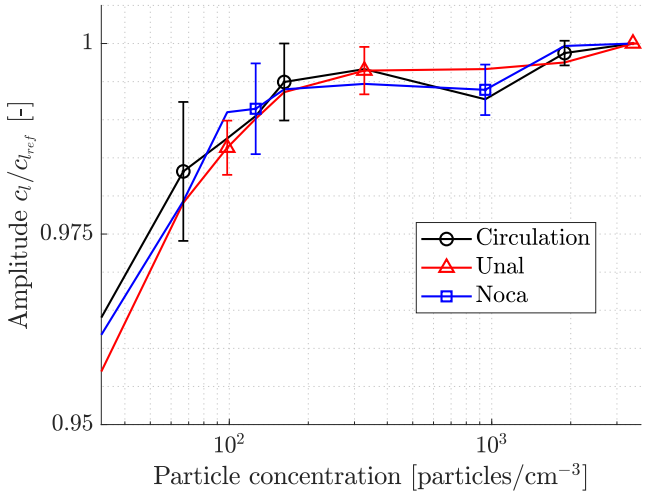

Figure 6.11: Sensitivity of the load determination methods to the particles concentration in terms of the sectional lift force variation. Results corresponding to Static Case 2 ($\alpha_0 = 10°$) at $z = 300$ mm.

This impact of the data noise arising from low particle concentrations is clearly reflected in Figure 6.11. In this figure, it can be easily perceived that sectional lift forces obtained through the implementation of the proposed load determination methods show negligible deviations to the baseline (< 1.5% of its magnitude) when concentrations greater than 100 particles/cm^3 are used, suffering considerable changes once lower concentrations are employed. Under the conditions set in this experimental investigation (Chapter 4), this particle concentration (100 particles/cm^3) is reached for acquisition times of around 3% of the reference measurement period, which corresponds to 0.025 s.

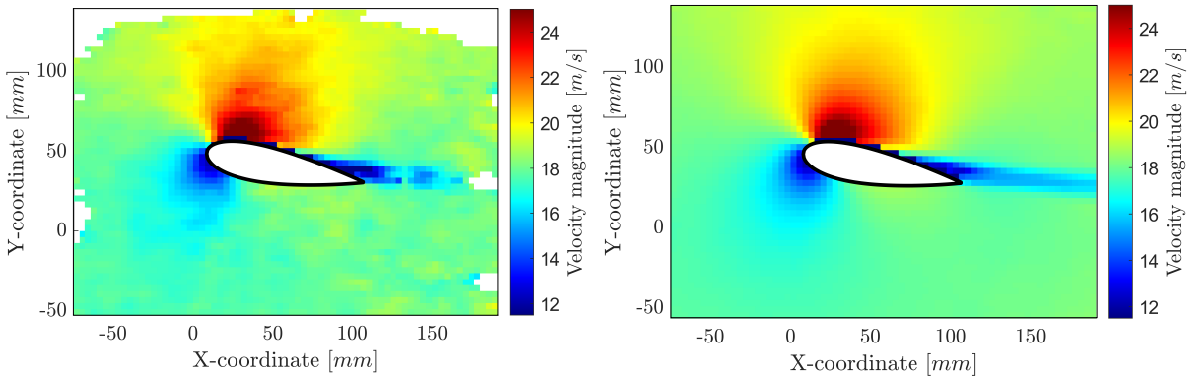

(a) Velocity field for 40 particles/cm^3.

(b) Velocity field for 3600 particles/cm^3 (Reference).

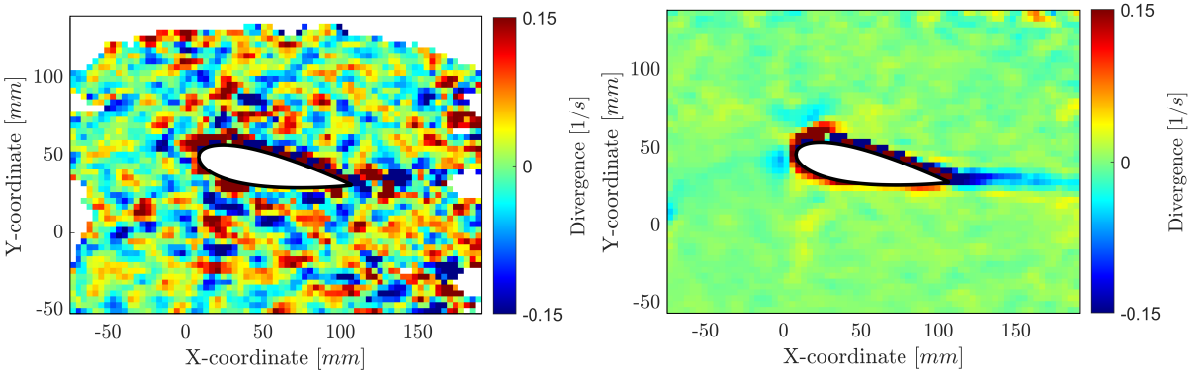

(c) Divergence field for 40 particles/cm^3.

(d) Divergence field for 3600 particles/cm^3 (Reference).

Figure 6.12: Flowfields corresponding to Static Case 2 ($\alpha_0 = 10°$) at $z = 300$ mm with various concentrations.

6.2. Static results

In this section, results corresponding to experimental test cases involving steady inflow conditions are analyzed. The findings of Section 6.1 are taken under consideration during the implementation of the non-intrusive load determination procedures to maximize the accuracy and precision of the reconstructed lift forces. Force balance measurements, described in Section 5.5, are taken as a reference to assess the validity of the proposed force reconstruction methods.

6.2.1. Sectional results

The spanwise distribution of sectional lift coefficients obtained non-intrusively through the proposed methods is analyzed and compared to that expected in unswept rigid wings throughout this section.

The first step in the obtainment of such arrangements is the evaluation of sectional lift forces at every sectional XY-plane along the span of the flexible wing. As described in Section 6.1, control volumes and integration paths with different shapes and sizes are desired to minimize the influence of random errors in the final reconstructed lift forces. Taking this information under consideration and accounting for the results found in Section 6.1, several control volume configurations are established and employed in the recovery of the lift distribution.

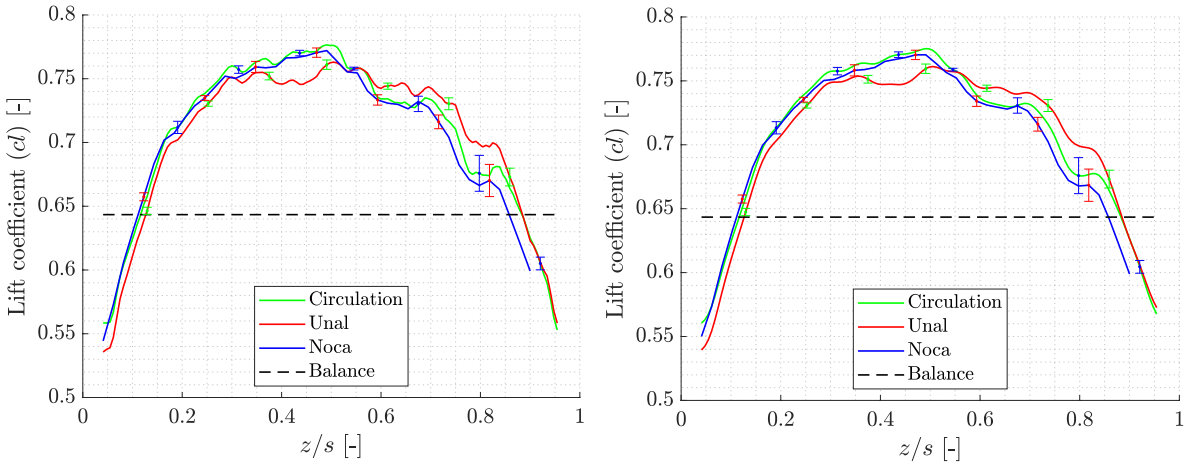

(a) Non-filtered.

(b) Filtered.

Figure 6.13: Spanwise distribution of the sectional lift coefficient before and after filtering processes are implemented. Results corresponding to Static Case 2 ($\alpha_0 = 10°$).

Nevertheless, some fundamental adjustments are incorporated to the original processes followed in Section 6.1 to determine the sectional lift forces for the sensitivity analysis of the load reconstruction techniques. In this case, data outliers are recognized not only by employing results at a fixed spanwise location, but also by including information from neighbouring sectional planes, with the objective of achieving a smoother lift distribution along the span. Intervals of 30 mm ($\approx$ 5% of the wing span) are employed to define closed data sets where such outliers are identified and where moving averages in form of low-pass filters with coefficients equal to the reciprocal of the span are implemented. A comparison between the distributions of sectional forces obtained from the direct calculation of the average sectional lift coefficient and that achieved after filtering the results is given in Figure 6.13, where a clear filtering of the small scale fluctuations is appreciated.

With regard to the resultant spanwise lift distributions shown in Figure 6.14, it is easily observed that some information is missing at regions close to wing root (from 0mm to 25 mm) and the wingtip (from 525mm to 550mm). The reason why the lift coefficient is not calculated in these sections lies in the reduced particle concentration that they present: as the minimum concentration requirements established in Section 5.3.3 ($N_{p,min} = 35$) are not met in a large number of interrogation windows, the resultant Eulerian flowfield presents an unmanageable number of data gaps, thus preventing the reconstruction of aerodynamic loads.

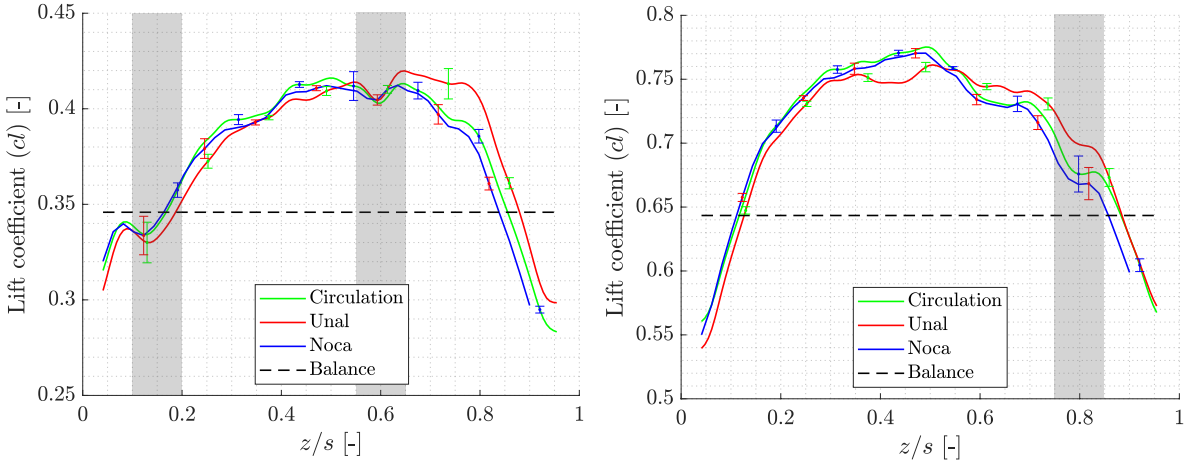

(a) Static Case 1 ($\alpha_0 = 5°$).

(b) Static Case 2 ($\alpha_0 = 10°$).

Figure 6.14: Spanwise distribution of the sectional lift coefficient in test cases involving steady inflow conditions.

Certain differences can be observed when this arrangement of the lift coefficient along the span of the flexible wing (Figure 6.14) is compared to theoretical distributions over rectangular rigid wings, similar to those shown in Figure 6.15. The most evident disagreement between both occurs at the root region of the test model: while circulation, and thus lift, reaches its maximum at the wing root when theoretical distributions are considered; minimum magnitudes of the lift coefficient are observed for the reconstructed ones. This decrease in the lift coefficient as the root of the model is approached is caused by the presence of the boundary layer of the splitting table, where the mean flow velocity is lower than expected ($U_{BL} < U_\infty = 18.3$ m/s). The region influenced by this reduction of the mean flow velocity and the sectional lift coefficient extends until $z \approx 150$ mm for both static test cases, which corresponds to the 25% of the wing span approximately. This distance is in good agreement with the boundary layer thickness observed in Figure 5.18 during the analysis of the inflow velocity (Section 5.3.4).

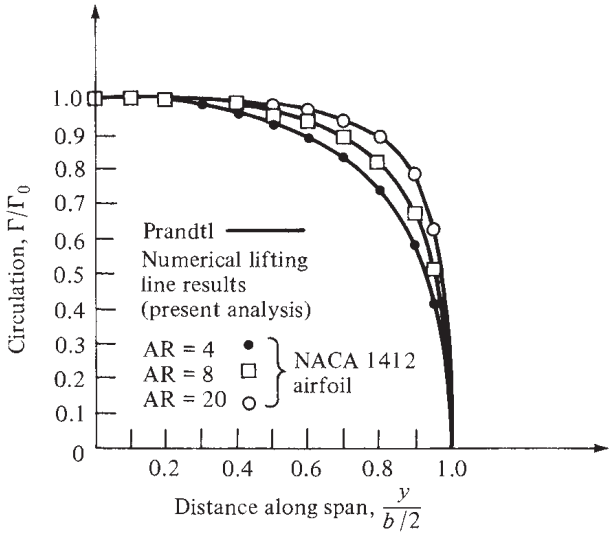

Figure 6.15: Theoretical lift distribution over a rectangular rigid unswept wing; comparison between Prandtls classical theory and the numerical lifting-line method. Reconstructed from Anderson Jr 2017.

Aside from these differences concentrated in the wing root region, no other deviations can be appreciated between the general trends of the experimental and theoretical lift distributions. Nevertheless, some fluctuations (marked with shadows in Figure 6.14) are observed for all load determination methods at certain locations along the span. There, the standard deviation of the sectional lift forces increases considerably with respect to other points along the span due to a greater dispersion of the reconstructed loads. Such deviations are mainly caused by great concentrations of numerical errors (Figure 6.16) at these spanwise locations arising from uncontrolled phenomena like big Helium-Filled Soap Bubbless not matching the buoyancy requirements or surface reflections not cancelled in the pre-processing steps (Section 5.1).

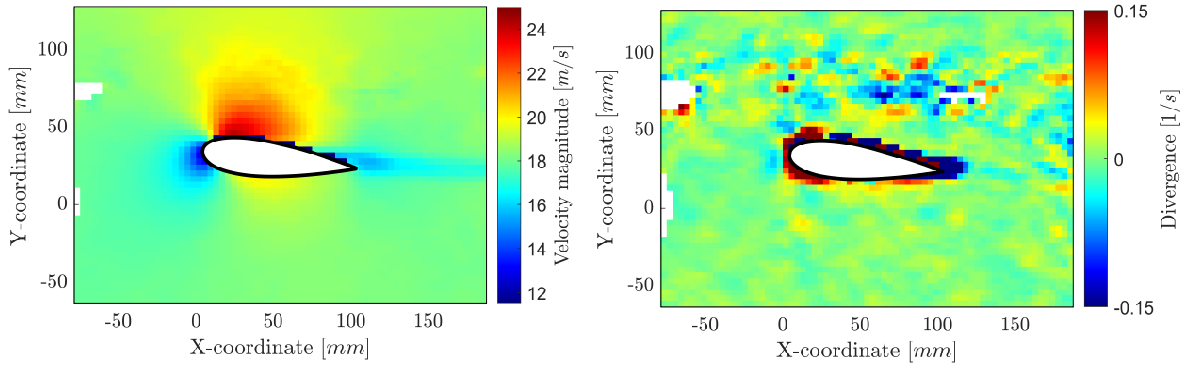

(a) Velocity field.

(b) Divergence field.

Figure 6.16: High data noise level section. Flowfields corresponding to Static Case 1 ($\alpha_0 = 5°$) at $z = 330$ mm.

6.2.2. Integral results

First, integral lift loads and other derived quantities are compared to baseline force balance measurements to assess the accuracy and precision of the proposed load reconstruction methods under steady inflow conditions. As described in Section 4.7, two static test cases are proposed for this purpose: a first case with limited structural deflections (Static Case 1, Table 4.3) and a second test case showing greater structural displacements and non-linear aerodynamic effects due to higher wing incidence angles (Static Case 2, Table 4.3).

Lift force

Concerning the lift forces experienced by the flexible wing under the established test conditions (Table 4.3), their magnitude is obtained through the integration of their sectional distribution across the span of the test object (Figure 6.14) for each of the control volume configurations. These results are then averaged to obtain the final value of the mean integral lift and its confidence interval (CI = 95%), similarly to what was done in Section 6.1. This process is repeated for each load determination method.

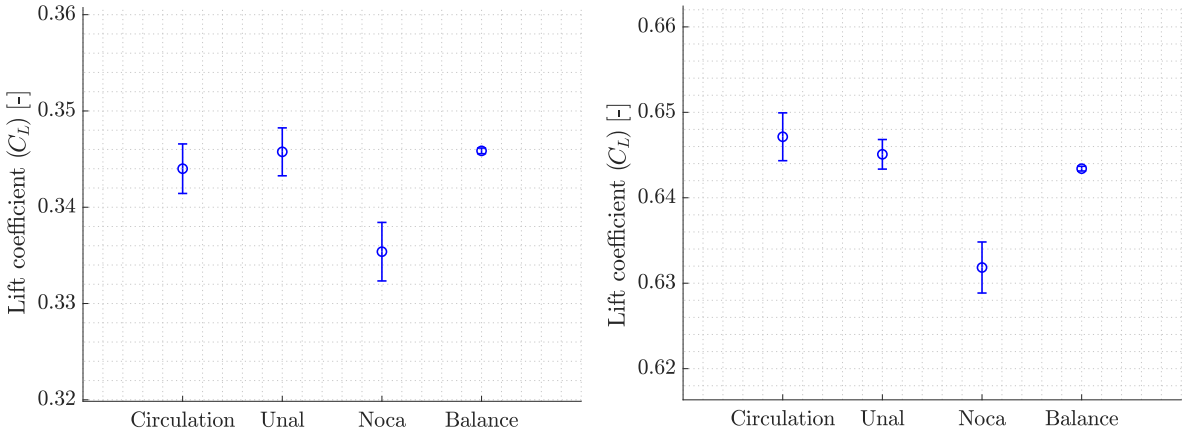

(a) Static Case 1 ($\alpha_0 = 5°$).

(b) Static Case 2 ($\alpha_0 = 10°$).

Figure 6.17: Integral lift coefficient in Static test cases.

Regarding the reference value of the lift force, it is obtained from four different balance measurements (one for each of the PIV acquisitions required to characterize the complete test model, Section 4.7.2), which are then merged and processed. The processing of the force balance data consists of two simple steps: On the one hand, raw measurements are projected onto the laboratory reference frame, accounting for the displacements experienced by the balance system when the rotating table is actuated. The rotation angle employed during these projections is equivalent to the incidence angle of the test object in every static test case. On the other hand, data outliers are removed from the raw data sets to prevent their influence on the final baseline loads. The number of uncorrelated data samples, employed to obtain the standard deviation of the mean balance lift force, is equal to the total number of samples in the balance measurements, as the characteristic time of the flow (time needed by a particle to travel along the airfoil chord, $\tau \approx 0.005s$) is smaller than that of the balance acquisition system (f = 100 Hz), as already described in Section 5.5.

	Balance (ref.)		**Kutta-Joukowski**		**Unal**		**Noca**	
	C_L [-]	ϵ	**C_L [-]**	ϵ	**C_L [-]**	ϵ	**C_L [-]**	ϵ
Case 1	0.346	-	0.344	0.55%	0.346	0.02%	0.336	2.92%
Case 2	0.644	-	0.648	0.58%	0.646	0.27%	0.632	1.83%

Table 6.1: Lift coefficient magnitude and deviation to the reference balance results in steady inflow test cases

As seen in Figure 6.17, the maximum deviations encountered between the mean value of the integral lift coefficients obtained through various force reconstruction techniques correspond to those calculated with the vorticity formulation of the momentum conservation equation (Noca, Equation 2.10) in both static test cases. These differences reach values of about 3% and 2% of the average lift coefficient of the reference force

balance results during Static Case 1 and Static Case 2 respectively. However, the weight of such error decreases if the confidence intervals of each result are considered (from 3% to 1.25% in Static Case 1 and from 2.5% to 1.5% in Static Case 2). An overview of these numerical results is given in Table 6.1.

Center of Pressure

After the accuracy of the load determination methods in test cases involving steady inflow conditions has been assessed by comparing the lift forces resulting from their implementation to baseline values coming from balance measurements, their capability to determine the spanwise location of the aerodynamic center of pressure is analyzed. The reason why this alternative variable is considered in this thesis lies in the fact that it provides information of interest for the characterization of aeroelastic phenomena.

Once more, force balance measurements corresponding to both static test cases are employed to determine the reference spanwise coordinate of the aerodynamic center of pressure. These coordinates are found employing readings of the vertical force (F_y) and the longitudinal moment (M_x) in the balance reference frame before they are projected to the laboratory coordinate system for the obtainment of the integral lift experienced by the wing. Finally, the resultant distance is corrected to account for the separation between the balance center and the wing root (d_{root} = 213.5 mm). The spanwise location of the center of pressure retrieved non-intrusively with the proposed optical measurement system (PIV) is obtained following a similar strategy to that employed with the reference force balance measurements.

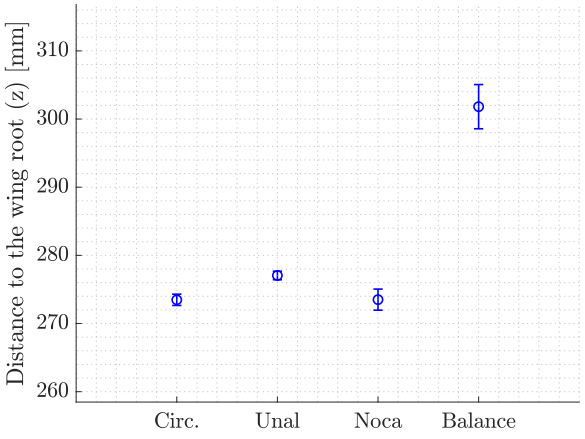

(a) Static Case 1 ($\alpha_0 = 5^\circ$). Numerical comparison.

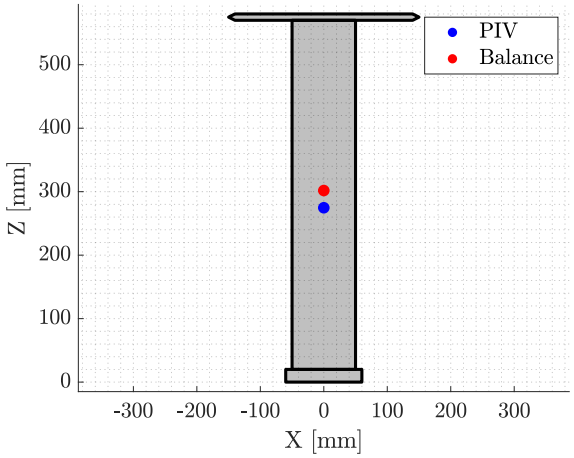

(b) Static Case 1 ($\alpha_0 = 5^\circ$). Graphical comparison.

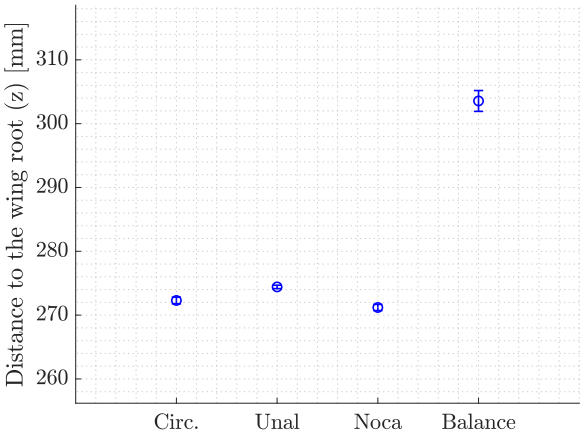

(c) Static Case 2 ($\alpha_0 = 10^\circ$). Numerical comparison.

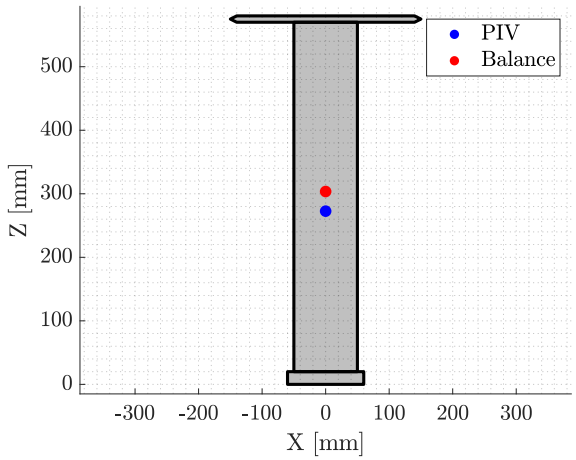

(d) Static Case 2 ($\alpha_0 = 10^\circ$). Graphical comparison.

Figure 6.18: Spanwise location of the Center of Pressure in Static test cases.

As seen in Figure 6.18, differences of about 30 mm are encountered between the spanwise position of the center of pressure reconstructed through non-intrusive load determination methods and the baseline coordinate established with force balance measurements, which correspond to a 5.5% of the total wing span. The source of such deviations might be attributed to two contributors: On the one hand, sectional drag forces are not considered during the obtainment of the spanwise coordinate of the center of pressure, although they are expected to be relevant at the wingtip rod (Figure 4.3), where the moment arm is the greatest (555 mm). On the other hand, as previously explained in Section 6.2.1, two regions of 25 mm at the root and the tip of the flexible model present particle concentrations that are so low that no sectional lift forces can be determined. Although sectional lift forces close to the wingtip are expected to be small (Figure 6.14), their distance to the wing root (moment arm) is much larger than that of sections with greater lift magnitudes, which is why their contribution to the longitudinal aerodynamic moment (M_x) needs to be considered.

6.3. Gust encounter results

In this section, results corresponding to experimental test cases involving unsteady inflow conditions in form of controlled gust profiles are analyzed. The findings of Section 6.1 are taken under consideration during the implementation of the non-intrusive load determination procedures to maximize the accuracy and precision of the reconstructed lift forces.

6.3.1. Sectional results

Sectional lift coefficients obtained non-intrusively through the proposed load determination methods are analyzed following two different approaches: On the one hand, the temporal evolution of the lift force at various sections of the wing along the span is presented (Figure 6.24 and Figure 6.31) and examined with the help of the available flowfield and structural information. On the other hand, the spanwise distribution of the lift coefficient obtained with each of the suggested force reconstruction methods at several time instants is shown and discussed briefly (Figure 6.32 and Figure 6.33).

Temporal evolution of the lift force at different sections

With regards to the temporal change of the lift coefficient along the span of the flexible wing in Dynamic Case 1 (Table 4.3), results are fitted employing non-linear regression models (sinusoidal fit) similar to those described in Section 5.3.2. This approach shows acceptable correlations with reference discrete values, irrespectively of the spanwise location being analyzed (Figure 6.19).

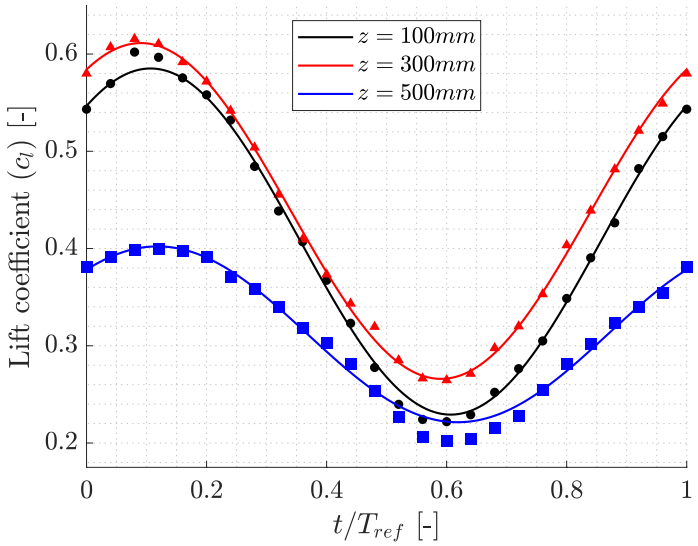

Figure 6.19: Sectional lift coefficient fitting. Results corresponding to Dynamic Case 1 ($\alpha_0 = 5°$; $\beta = 5°$; f = 5.7 Hz).

The suitability of this method can also be argued after examining the evolution in time of the velocity field around the test object at various spanwise locations (Figure 6.20 and Figure 6.21), as there are no signs of the

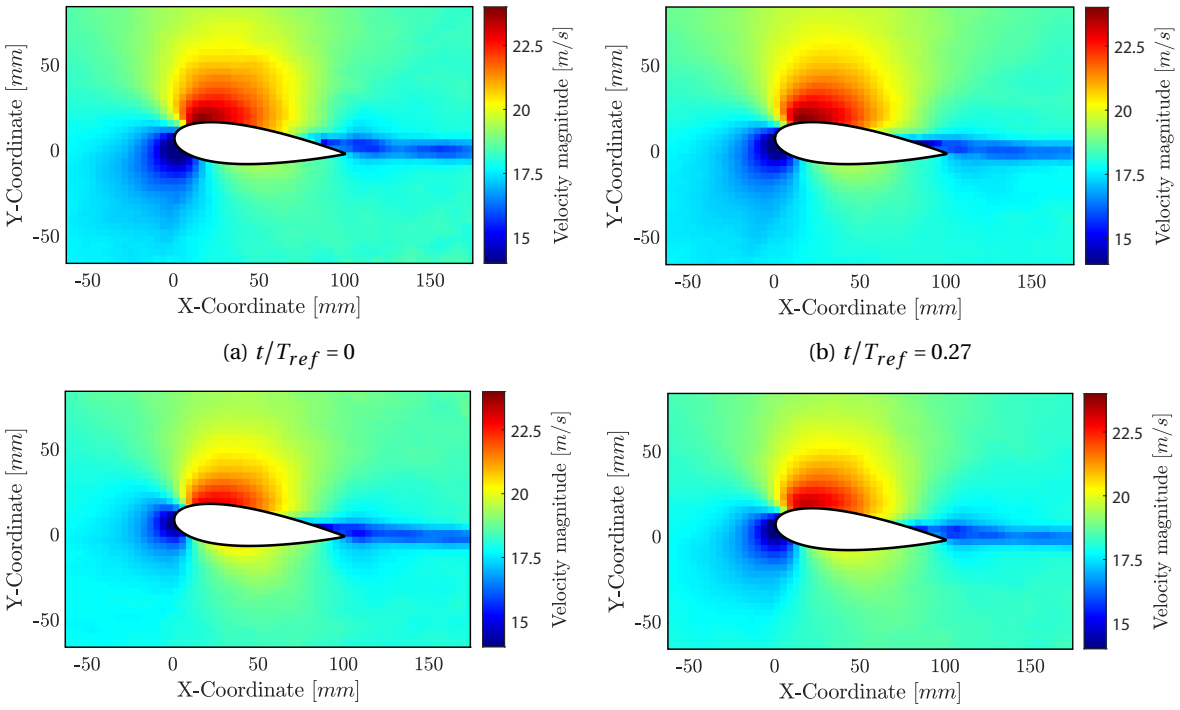

(a) $t/T_{ref} = 0$ (b) $t/T_{ref} = 0.27$

(c) $t/T_{ref} = 0.54$ (d) $t/T_{ref} = 0.81$

Figure 6.20: Velocity fields at various time instants. Results corresponding to Dynamic Case 1 ($\alpha_0 = 5°$; $\beta = 5°$; f = 5.7 Hz) at z = 100 mm.

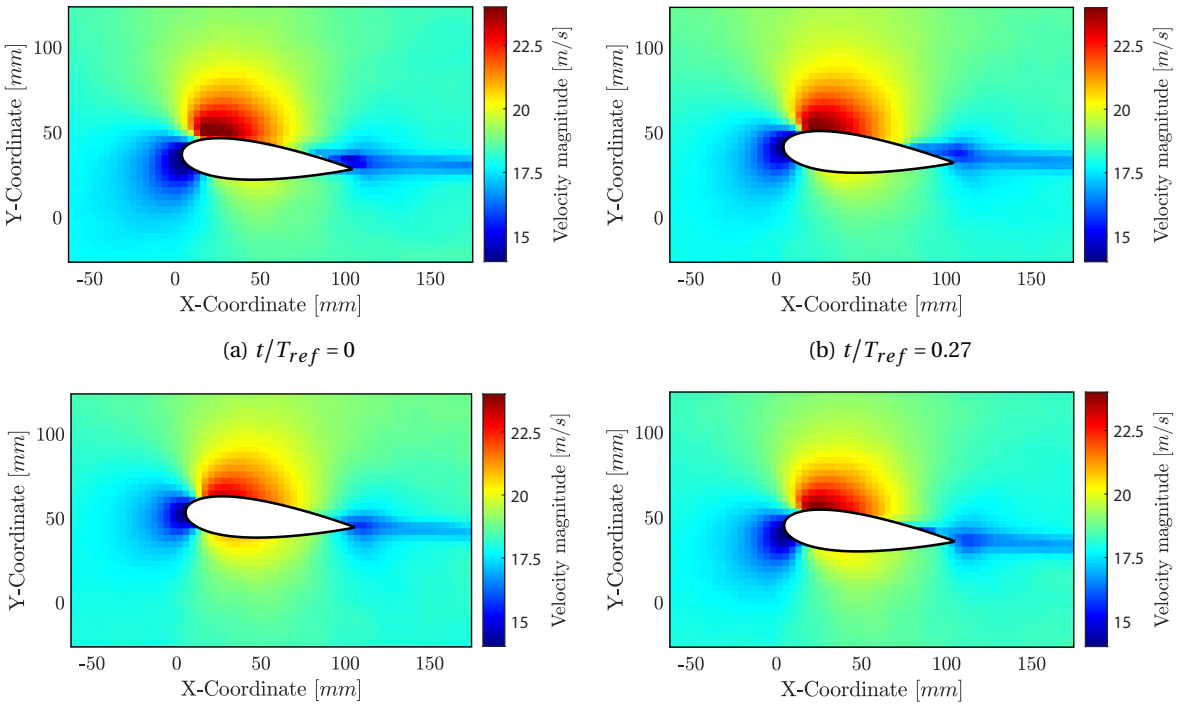

(a) $t/T_{ref} = 0$ (b) $t/T_{ref} = 0.27$

(c) $t/T_{ref} = 0.54$ (d) $t/T_{ref} = 0.81$

Figure 6.21: Velocity fields at various time instants. Results corresponding to Dynamic Case 1 ($\alpha_0 = 5°$; $\beta = 5°$; f = 5.7 Hz) at z = 500 mm.

appearance of non-linear aerodynamic phenomena (massive boundary layer detachment, wake thickness growth, vortical structures shedding, etc.).

This information can be complemented with the analysis of the evolution of the effective angle of attack that each spanwise section of the wing experiences during the test (Figure 6.23). Three different contributors, whose value is determined from the available structural data, are considered in the present study for this purpose: geometric (static) angle of attack (α_0), whose value is fixed depending on the test case being considered (5° and 10° in Dynamic Case 1 and 2 respectively, Table 4.3); angle of attack induced by the presence of the crossflow velocity (α_G), which is considered to be constant along the wing chord given the wavelength of the gust profile ($\lambda_G \ll c$); and the angle of attack changes arising from the plunging motion of the flexible wing (α_P). Other phenomena that might impact the effective angle of attack of the wing, like 3D effects, are out of the scope of the present inquiry, thus not considered in the obtainment of the section effective angle of attack.

The angle of attack induced by the traverse velocity profile (gust) is defined from the foremost information in the field of view (measurement volume) to minimize the influence of the leading-edge stagnation point in the measured flow velocity. This variation in the angle of attack can be expressed as:

$$\alpha_G = \arctan\left(\frac{v_G}{u_G}\right) \tag{6.1}$$

Where v_G is the crossflow velocity component induced by the gust generator and u_G the velocity at which the gust profile is advected ($u_G \approx U_\infty$).

Similarly, the angle of attack variation introduced by the plunge motion of the test object is defined from its velocity displacement information, which is obtained following the procedure described in (Section 5.3), as:

$$\alpha_P = -\arctan\left(\frac{v_P}{U_\infty}\right) \tag{6.2}$$

Being v_P the mean (along the span) wing surface velocity in the direction perpendicular to the flow stream (y-axis) and U_∞ the freestream velocity.

Following this reasoning, the effective angle of attack experienced by each wing section can be formulated as:

$$\alpha_{eff} = \alpha_0 + \alpha_G + \alpha_P = \alpha_0 + \arctan\left(\frac{v_G}{u_G}\right) - \arctan\left(\frac{v_P}{U_\infty}\right) \tag{6.3}$$

The magnitude of each of these contributors at various spanwise locations in Dynamic Case 1 is presented in Figure 6.22.

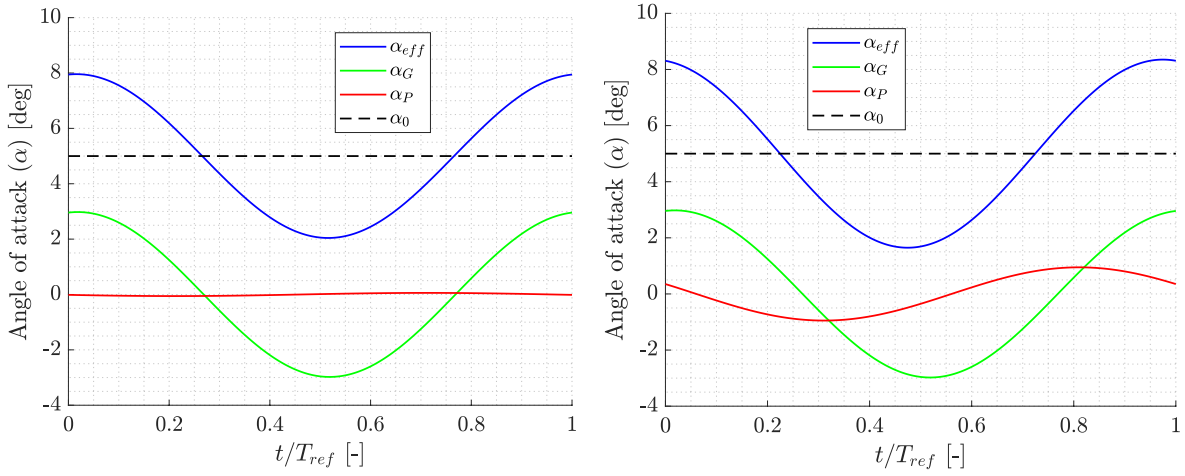

(a) z = 100 mm (b) z = 500 mm

Figure 6.22: Effective angle of attack contributors at various spanwise locations. Results corresponding to Dynamic Case 1 ($\alpha_0 = 5°$; $\beta = 5°$; f = 5.7 Hz).

As seen in Figure 6.22, the influence of the plunge-induced angle of attack in the overall effective angle of attack grows as the distance to the tip of the flexible wing model decreases, as so does its structural deflection and velocity. In addition, it can also be appreciated that the magnitude of such induced angle is always smaller than that of the angle variation introduced by the incidence of the gust.

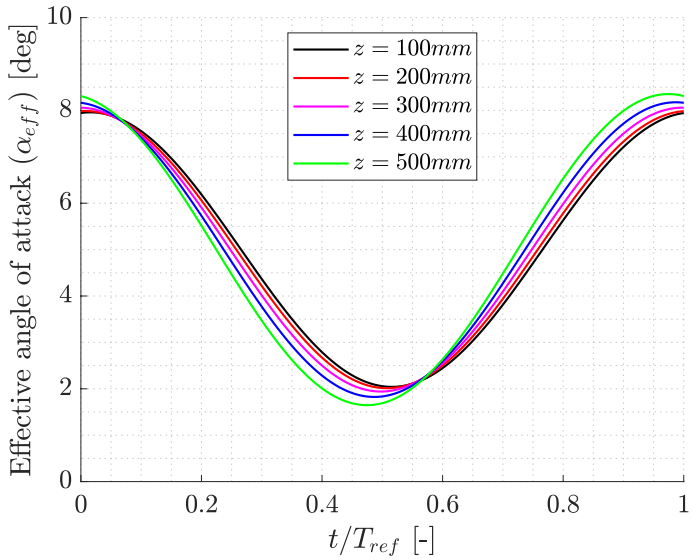

Figure 6.23: Effective angle of attack variation along the span of the test object. Results corresponding to Dynamic Case 1 ($\alpha_0 = 5°$; $\beta = 5°$; f = 5.7 Hz).

Going back to the purpose of this effective angle of attack analysis, Figure 6.23 shows that, during Dynamic Case 1 (Table 4.3), none of the spanwise sections of the flexible wing experiences effective angles of attack out of the region where linear aerodynamic phenomena are expected. These results, together with the analysis previously mentioned, contribute to the validation of the initial assumption of considering sinusoidal regression models as a viable fitting method (if 3D effects are considered to be sufficiently small to avoid the appearance of non-linear aerodynamics).

However, additional relevant information, which might be useful throughout the examination of the temporal evolution of the lift coefficient along the span (Figure 6.24), can be extracted from the examination of Figure 6.23. Two main factors of interest for such analysis can be pointed out from the results given in Figure 6.23: First, the advancing time-shift in the effective angle of attack as the wingtip region is approached. This shift is a direct consequence of the phase-lag between the gust-induced angle (α_G) and the plunge-induced angle (α_P) already observed in Figure 6.22, which gains importance as the magnitude of α_P increases. Secondly, the growth in the effective angle of attack amplitude at higher wing sections. Nevertheless, this effect will not be as relevant as the previous given the influence of wingtip effects in the lift magnitude (Figure 6.15) and the size of the observed effective angle of attack amplitude differences (very small).

Once the proposed method to analyze the time-signal of the lift coefficient at different sections in Dynamic Case 1 has been proven to be valid, the results obtained from its application (Figure 6.24) can be analyzed.

The first aspect that can be appreciated in such results, which is consistent independently of the load determination method employed for their obtainment (Chapter 2), is the evolution across the wing span of the mean value of the lift coefficient and of the amplitude of its signal. A growth in the mean value and the amplitude of the lift coefficient exists between the sections closest to the wing root (z = 100 mm) and those closer to the test object midspan (z = 200 mm & z = 300 mm). The growing trend of both parameters is reversed (they decrease) once the distance to the wingtip is sufficiently small (z = 400 mm), reaching differences of about 26.5% in the mean value and 35.4% in the signal amplitude (if compared to midspan results) at the highest section analyzed (z = 500 mm). The reasoning behind these tendencies is similar to that presented in Section 6.2.1 as justification of the results given in Figure 6.14: On the one hand, the presence of the boundary layer of the splitting table (Figure 5.18) causes a drop in the lift force of the wing in regions lower than z ≈ 150

mm. On the other hand, wingtip (3D) effects have a negative impact on the effective angle experienced by the wing reducing the magnitude and amplitude of the lift force temporal evolution.

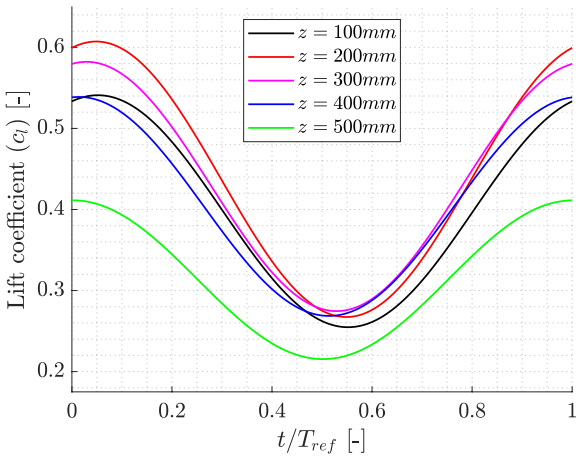

(a) Circulation

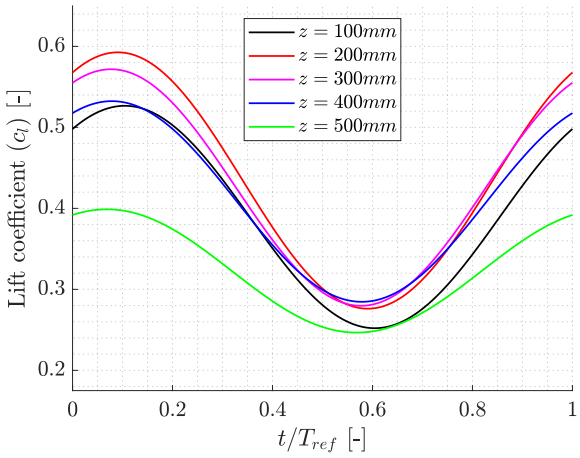

(b) Unal

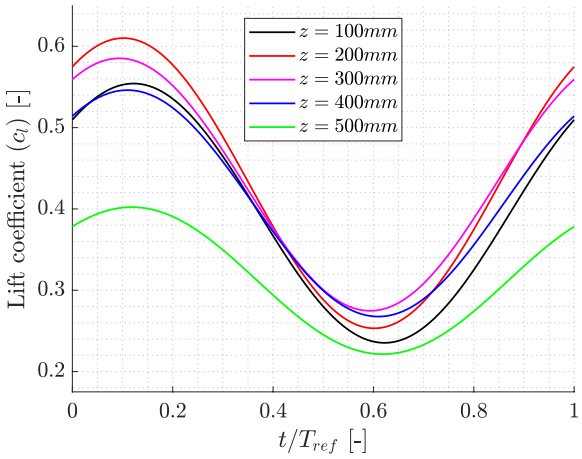

(c) Noca

Figure 6.24: Time-dependent sectional lift coefficient signal at various spanwise locations. Results corresponding to Dynamic Case 1 ($\alpha_0 = 5°$; $\beta = 5°$; f = 5.7 Hz).

Besides, the second aspect that can be easily observed in Figure 6.24 are the phase differences between the fitted lift coefficient signals at various spanwise locations. The origin of such discrepancies lies in the aforementioned time-shift in the effective angle of attack (Figure 6.23), as well as in the influence of the flow unsteadiness ($k \approx 0.1$ in Dynamic Case 1, Table 4.3) in the force experienced by the wing. By examining the results given in Figure 6.24, it can be argued that the change in the temporal character of the force has an advancing time-shift trend as the tip of the model is approached.

Nonetheless, deeper and more complete examinations can be performed if the information obtained from the sinusoidal fitting of discrete results is employed, as one of the coefficients that define the non-linear regressions employed for this purpose (Equation 5.15) is the phase-lag of the reconstructed signal.

Furthermore, these analyses can be complemented with results from analytical models that aim to characterize the influence of flow unsteadiness in lift forces experienced by 2D airfoils. Such analytical models rely on theories and hypotheses like potential flow theory (inviscid, irrotational and incompressible flow), thin airfoil theory or small perturbations theory that are not valid for real applications. Nevertheless, the influence of the deviations introduced by these assumptions is considered to be sufficiently small for the purpose of this study.

The first step in the implementation of these analytical models is the identification of the sources of unsteadiness in the phenomenon being analyzed. As mentioned previously, the aeroelastic problem considered in the present experimental investigation (wing-gust encounter) combines two main effects:

- Effective angle of attack variations induced by the periodic plunging motion of the flexible wing (α_P).
- Effective angle of attack variations caused by gust-induced traverse flow velocity profiles impinging on the flexible wing (α_G).

Nevertheless, if linear aerodynamics across the entire wing span are considered (validity of the principle of superposition) and constant gust profiles are assumed irrespectively of the spanwise location, the effects of the effective angle of attack variations caused by the gust incidence in the evolution of the time-shift in the lift coefficient signal across the span of the test object can be neglected, thus reducing the analysis to the examination of the plunging motion effects in the lift force.

The analytical model proposed in the present study to quantify the effects of periodic plunging motions in the lift coefficient of oscillating airfoils is Theodorsen's theory (Theodorsen 1934). This theory states that the lift coefficient of an harmonically oscillating airfoil can be expressed as:

$$c_l = c_{l_\alpha} \cdot \alpha + \left(c_{l_\alpha} k i C(k) - \pi k^2 \right) \cdot \frac{2}{c} \cdot y(t) \tag{6.4}$$

Where $c_{l_\alpha} \cdot \alpha$ is the mean lift coefficient; k the reduced frequency of the plunging motion; c the airfoil chord; c_{l_α} the steady lift coefficient slope; $y(t) = y_0 e^{i\omega t}$ the formula that characterises the harmonic plunging motion of the airfoil; and $C(k)$ the Theodorsen's function, which is formulated as:

$$C(k) = F(k) + iG(k) = \frac{H_1^{(2)}(k)}{H_1^{(2)}(k) + iH_0^{(2)}(k)} \tag{6.5}$$

Being $H_n^{(2)}$ the nth-order Hankel functions of the second kind (Harris 2014).

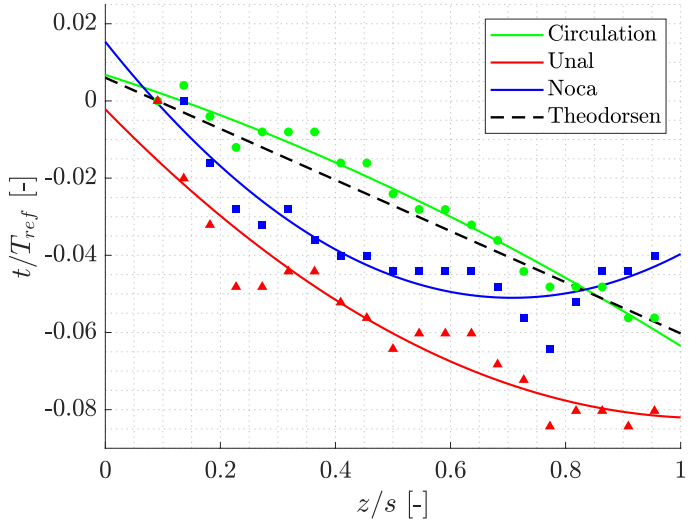

Figure 6.25: Spanwise lift coefficient time-shift. Results corresponding to Dynamic Case 1 ($\alpha_0 = 5°$; $\beta = 5°$; f = 5.7 Hz).

The spanwise distribution of the lift coefficient time-shift obtained from the implementation of Theodorsen's theory is presented in Figure 6.25, together with the time-shift results acquired through the implementation of the proposed load determination methods. These results, both analytical and experimental, are fitted employing second-order polynomial regression models. Time-shift values are obtained taking the $z' = z/s \approx 0.1$ section, where the first row of surface markers is located, as reference. A consistent advancing trend can be appreciated in all methods. This result could already be expected considering the effective angle of attack variation shown previously in Figure 6.23. In addition, these trends also show an almost linear behaviour

with the spanwise coordinate of the section being analyzed irrespectively of the method employed. However, Kutta-Joukowski theorem (circulation method) seems to provide results in closer agreement with the analytical values (Theodorsen) than those obtained with the momentum conservation methods, independently of the employed formulation (Unal, Equation 2.1 & Noca, Equation 2.10).

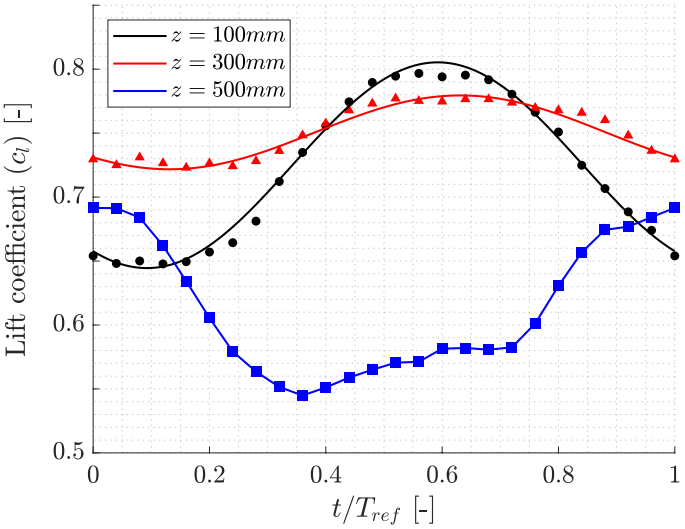

Figure 6.26: Sectional lift coefficient fitting. Results corresponding to Dynamic Case 2 ($\alpha_0 = 10°$; $\beta = 5°$; f = 3.2 Hz).

Once the methodology employed to analyze the temporal evolution of the lift force at different sections of the flexible wing in Dynamic Case 1 (Table 4.3) has been presented, its appropriateness to perform similar examinations in Dynamic Case 2 (Table 4.3) is assessed.

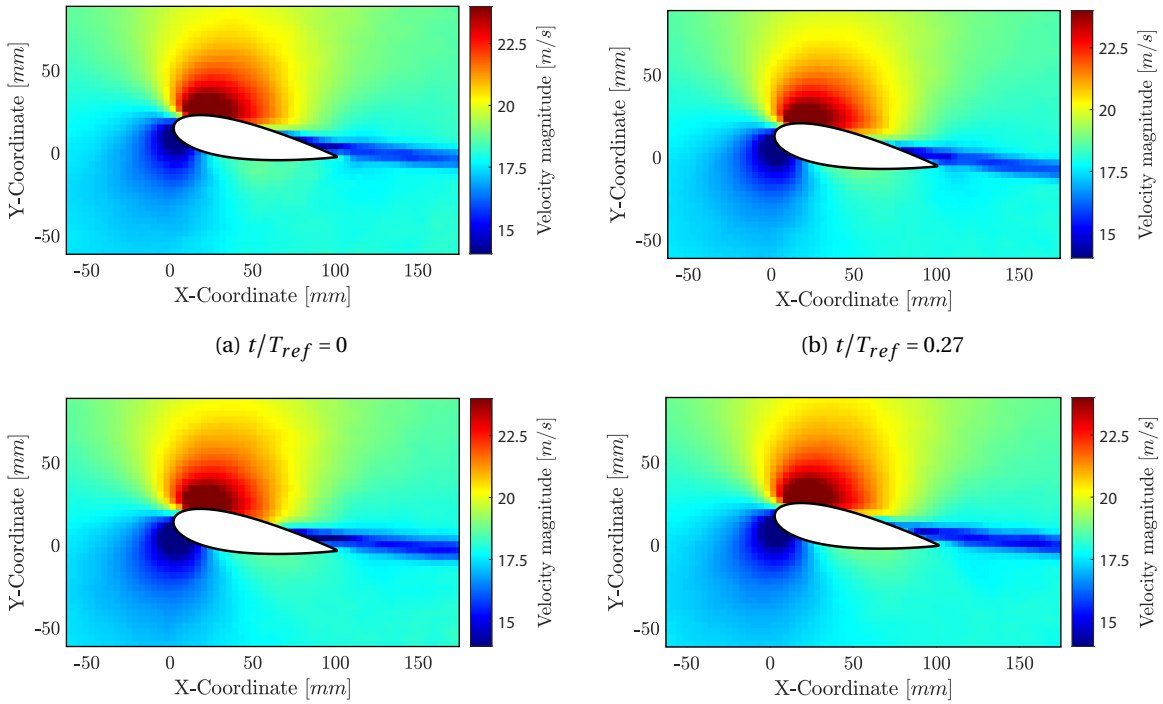

(a) $t/T_{ref} = 0$

(b) $t/T_{ref} = 0.27$

(c) $t/T_{ref} = 0.54$

(d) $t/T_{ref} = 0.81$

Figure 6.27: Velocity fields at various time instants. Results corresponding to Dynamic Case 2 ($\alpha_0 = 10°$; $\beta = 5°$; f = 3.2 Hz) at z = 100 mm.

The most relevant aspect of the proposed methodology of analysis is the employment of non-linear regression models, in form of sinusoidal fits, to obtain continuous descriptions of the temporal evolution of discrete lift coefficient results. However, as seen in Figure 6.26 and contrary to what is observed in Dynamic Case 1 (Figure 6.19), results pertaining to the upper region of the test model ($z \gtrsim 300$ mm) do not follow harmonic sinusoidal distributions, thus impeding the implementation of such procedures and the studies derived from them (time-shift analysis of lift coefficient across the span, Figure 6.25). For the shake of consistency, such non-linear sinusoidal fits will not be employed in the remaining Dynamic Case 2 aerodynamic force results, independently of the spanwise section being analyzed.

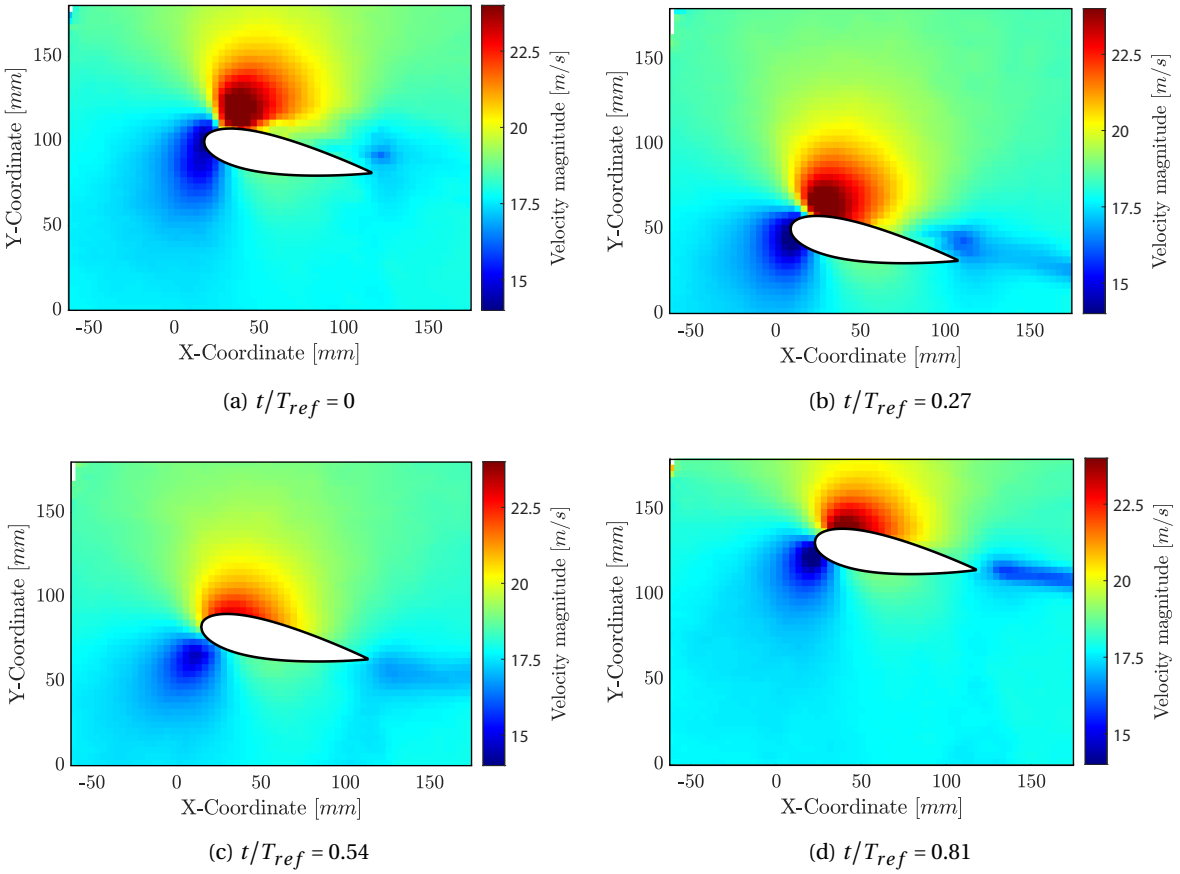

(a) $t/T_{ref} = 0$ (b) $t/T_{ref} = 0.27$

(c) $t/T_{ref} = 0.54$ (d) $t/T_{ref} = 0.81$

Figure 6.28: Velocity fields at various time instants. Results corresponding to Dynamic Case 2 ($\alpha_0 = 10°$; $\beta = 5°$; f = 3.2 Hz) at z = 500 mm.

Certain efforts are made in this section to examine the available information (flowfield and structural) and to clarify the observed behaviour of the aerodynamic forces at the top part of the flexible wing.

First, velocity fields at different time instants and spanwise sections are presented in Figure 6.27 and Figure 6.28. Clear differences can be appreciated between the temporal evolution of the flow at sections close to the wing root (Figure 6.27) and the flow development at regions where greater structural deformations are accomplished (Figure 6.28). Some of the most relevant disagreements appear in the flow structures shed in the wing wake: while the morphology (thickness and location) of the wake in Figure 6.27 seems to be almost constant in time, radical changes manifest in Figure 6.28 as a consequence of the shedding of big vortical structures. Similarly, strong differences in the temporal evolution of the velocity at the airfoil suction peak (up to a 21% of the inflow velocity magnitude), which are not present in sections with limited structural deflections (Figure 6.27), are also observed at the upper region of the model (Figure 6.28).

The presence of such shed vortical structures in the wake region of the upper part of the wing is an indicative of the presence of non-linear aerodynamics effects; contrary to what is observed in Dynamic Case 1, where linear aerodynamics are assumed across the entire span of the test model. These non-linear phenomena

affect the expected harmonic evolution of the lift force, resulting in temporal signals (Figure 6.26) that cannot be fitted employing the same strategies (non-linear sinusoidal regressions) followed in Dynamic Case 1.

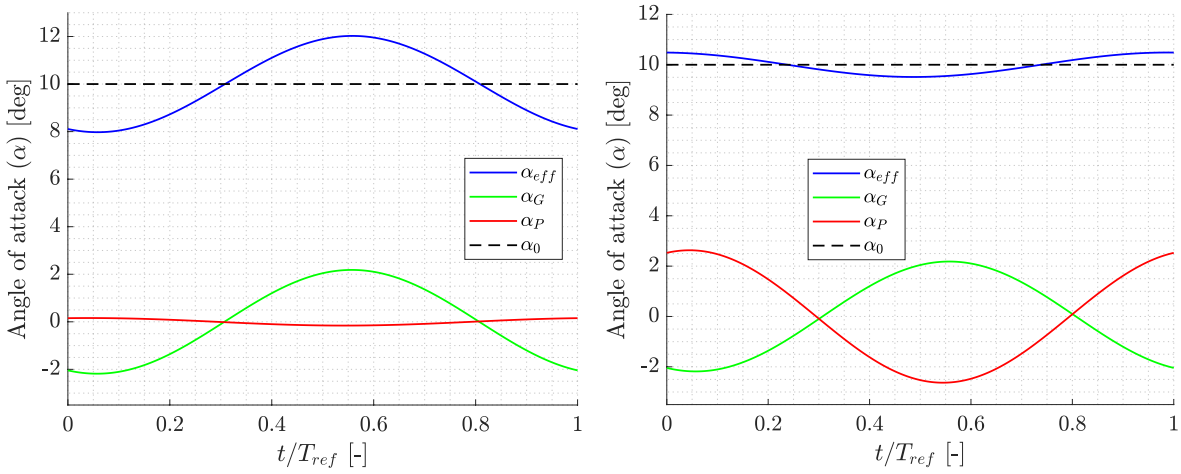

(a) z = 100 mm (b) z = 500 mm

Figure 6.29: Effective angle of attack contributors at various spanwise locations. Results corresponding to Dynamic Case 2 (α_0 = 10° ; β = 5° ; f = 3.2 Hz).

Once more, the flowfield information shown in Figure 6.27 and Figure 6.28 can be complemented with the analysis of the evolution of the effective angle of attack at various spanwise sections during Dynamic Case 2. The contributors to the effective angle of attack, as well as their formulations, have been previously presented and explained with data from Dynamic Case 1 (Equation 6.3). The magnitude of such terms at different sections in Dynamic Case 2 is shown in Figure 6.29, while the temporal evolution of the resultant effective angle at several spanwise locations is given in Figure 6.30.

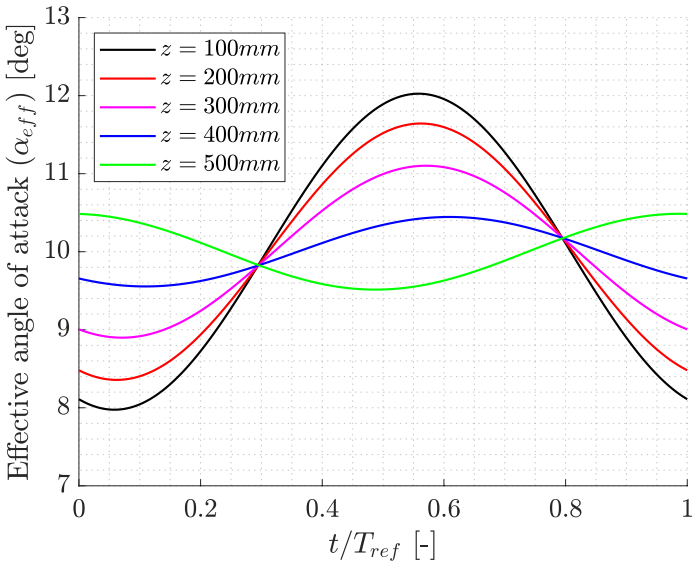

Figure 6.30: Effective angle of attack variation along the span of the test object. Results corresponding to Dynamic Case 2 (α_0 = 10° ; β = 5° ; f = 3.2 Hz).

As it can be seen in Figure 6.30, the effective angle of attack experienced by the wing in Dynamic Case 2 is strongly dependent on the spanwise section being analyzed. These expected differences, which are not observed during Dynamic Case 1 (Figure 6.23), are mainly caused by the scale of the structural displacements of the test model at the wingtip region compared to those attained closer to the wing root. In addition, the

phase-lag between the plunge-induced angle (α_P) and that introduced by the gust profile (α_G), which can be observed in Figure 6.29, also contribute to the time-shift trends in the effective angle of attack that the results in Figure 6.30 present.

Besides, other contributors to the effective angle of attack, aside from those considered in this analysis (gust α_G and plunge α_P), are expected in Dynamic Case 2 (although they cannot be quantified with the available structural information). Such alternative contributors to the effective angle of attack are mainly caused by the presence of 3D phenomena due to wingtip effects and spanwise velocity gradients arising from large structural displacements. Nonetheless, in spite of these limitations, this information can still be employed to extract meaningful conclusions for the purpose of this inquiry.

First, Figure 6.30 shows how the reconstructed effective angles of attack reach high values (up to 12°) that lay inside the region in the airfoil polar where non-linear aerodynamics are expected. Moreover, a major shift in the temporal character of the angles signal can be appreciated at heights above z = 400 mm as a consequence of the growth of the plunge-induced angle (α_P) magnitude above that of the gust-induced angle (α_G). Finally, a decrease in the effective angle of attack signal amplitude is observed as the distance of the analyzed section to the wing root is increased (z-coordinate). This last phenomenon appears as a result of the phase-lag between α_G and α_P (about 180°, Figure 6.29) and the increased importance of the latter in higher wing regions.

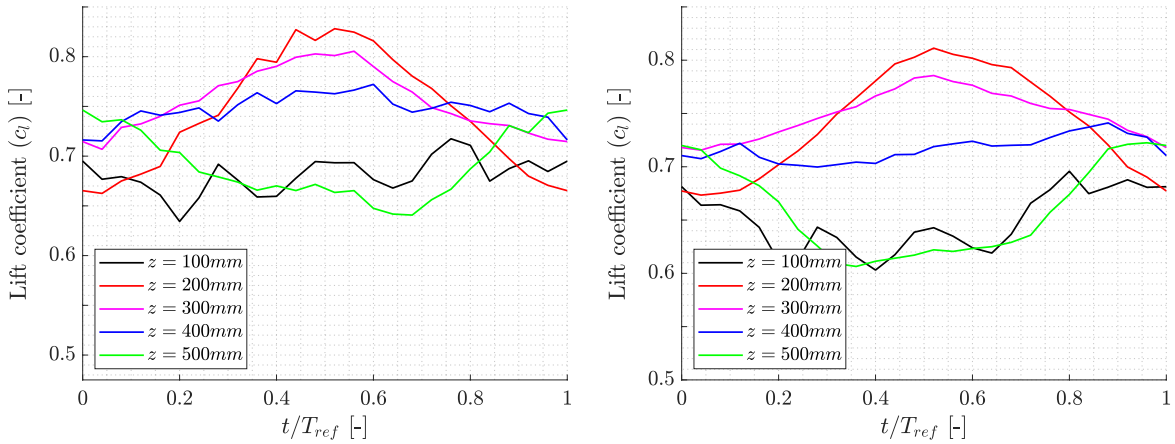

(a) Circulation

(b) Unal

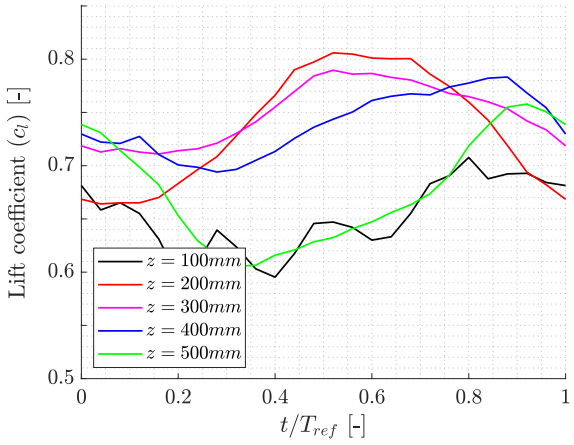

(c) Noca

Figure 6.31: Time-dependent sectional lift coefficient signal at various spanwise locations. Results corresponding to Dynamic Case 2 (α_0 = 10° ; β = 5° ; f = 3.2 Hz).

After the causes of the non-harmonic behaviour (temporal) of the reconstructed loads at the top part of the wing have been discussed with the available structural and flowfield information, the trends in the spanwise distribution of the temporal evolution of such loads are presented and examined (Figure 6.31), comparing the different methods employed in their obtainment.

The first aspect that can be appreciated in the results of all load determination methods is the growth in the mean lift value as sections closer to the wing root (z = 100 mm) are outdistanced and midspan sections are approached (z = 300 mm). However, as expected from the effective angle of attack spanwise variation (Figure 6.30), the amplitude of the reconstructed sinusoidal lift signal decreases in this same region, contrary to the increase in the amplitude observed during Dynamic Case 1 at the lower half of the test object. On the other hand, advancing temporal shifts are also appreciated in the results of this region of the flexible wing, irrespectively of the load reconstruction method used in the process, similarly to Dynamic Case 1 (Figure 6.25).

Some trends can also be distinguished in the results corresponding to the upper half of the wing, despite the inability to implement sinusoidal fits to the discrete lift values due to the appearance of aerodynamic and structural non-linear in this region of the measurement volume. The most relevant is the decrease in the mean lift force at the uppermost sections of the wing due to the influence of wingtip 3D phenomena (Figure 6.15), as happened in Dynamic Case 1 (Figure 6.24) and in both Static test cases (Figure 6.14). In addition, Figure 6.31 also shows how the load determination methods based on the momentum conservation equation (Unal, Figure 6.31b & Noca, Figure 6.31c) provide similar results, while Kutta-Joukowski theorem (circulation method) in this region provide results that differ from the previous. No further comments can be made on these discrepancies, as the measurement systems employed as a reference in the experimental campaign are not capable to provide sectional information to compare with.

Spanwise distribution of the lift coefficient

Concerning the spanwise distribution of the lift coefficient at various time instants during test cases involving unsteady inflow conditions, a strategy similar to that followed during the analysis of the spanwise distribution of the sectional lift coefficient in Static test cases is employed: First, sectional lift forces are evaluated at each XY-plane along the span of the flexible wing employing various control volume configurations that are defined accounting for the results found in Section 6.1. Then, the resultant lift distributions are smoothed employing 30 mm moving windows where data outliers are filtered and removed.

Some general comments can be made respecting all test cases involving unsteady inflow conditions (Dynamic Cases 1 & 2, Table 4.3) and their similarities. First, the influence of the boundary layer of the splitting table ($U_{BL} < U_\infty$ = 18.3 m/s) is observed at the lowermost region of the flexible wing (z ≈ 150 mm) in the results corresponding to both test cases. Secondly, wingtip (3D) effects are also appreciated in both cases at every time instant in all load determination methods, in agreement with the theoretical lift distribution in a finite span wing (Figure 6.15) and with the results obtained in Static test cases (Figure 6.14). Furthermore, certain deviations between the instantaneous mean lift coefficient of different load determination methods can be noticed in both Dynamic test cases (Figure 6.32 & Figure 6.33). These differences can be attributed to the inconsistencies in the temporal information (phase-lag) of the reconstructed lift force signals of the employed force reconstruction procedures observed both in sectional results (Figure 6.24 & Figure 6.31) and in integral results (Figure 6.35).

Focusing on the discrepancies encountered between the results in Dynamic Case 1 (Figure 6.24) and in Dynamic Case 2 (Figure 6.31), the most relevant relate to the changes in time experience by such distributions: while spanwise lift distributions corresponding to Dynamic Case 1 encounter significant changes in time of the mean lift coefficient and the maximum spanwise lift force; such temporal evolution is not observed in Dynamic Case 2 results. These trends have been already encountered and commented in the previous section, where the temporal evolution at various spanwise locations was analyzed.

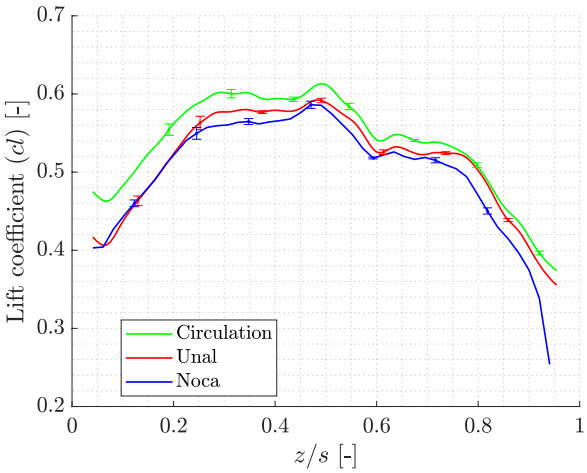

(a) $t/T_{ref} = 0$

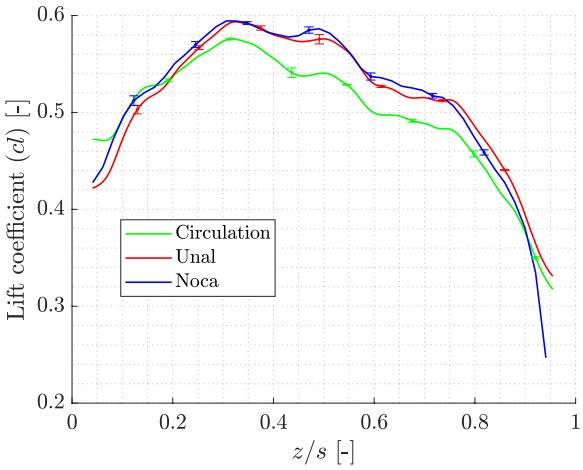

(b) $t/T_{ref} = 0.16$

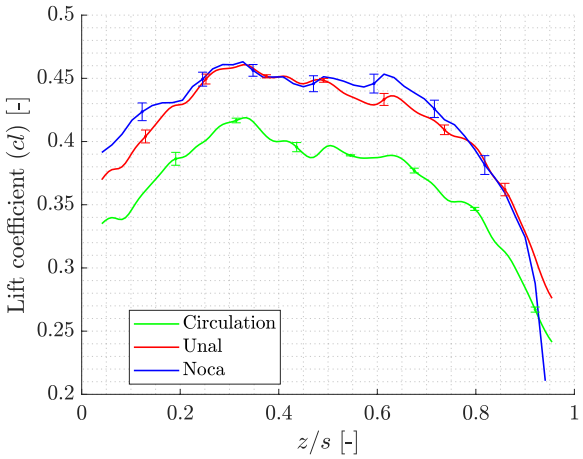

(c) $t/T_{ref} = 0.32$

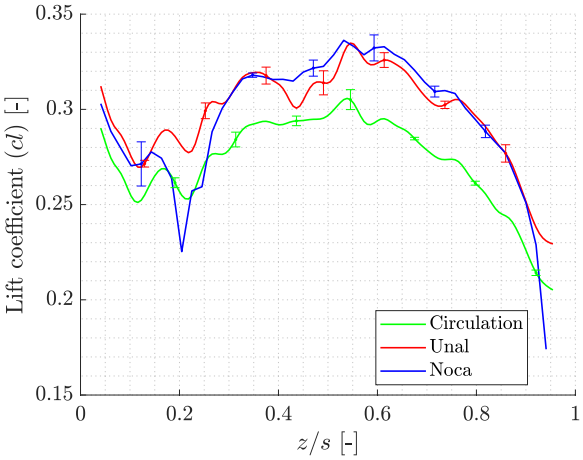

(d) $t/T_{ref} = 0.48$

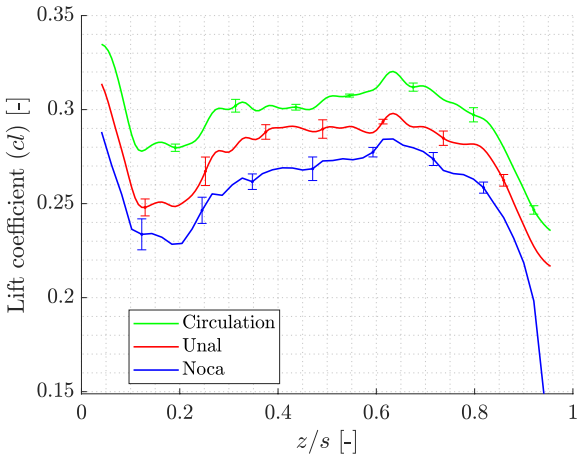

(e) $t/T_{ref} = 0.64$

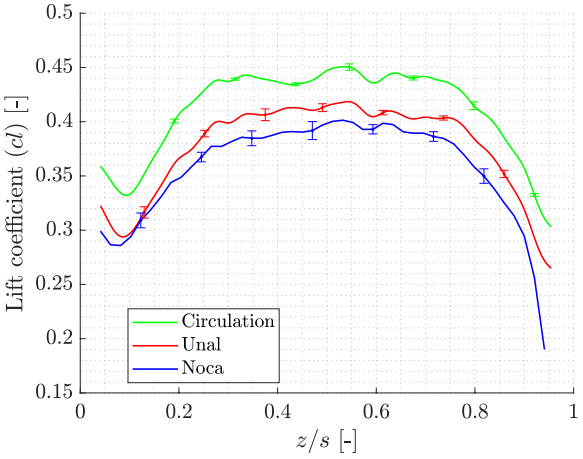

(f) $t/T_{ref} = 0.80$

Figure 6.32: Spanwise distribution of the sectional lift coefficient at various time-instant. Results corresponding to Dynamic Case 1 ($\alpha_0 = 5°$; $\beta = 5°$; f = 5.7 Hz).

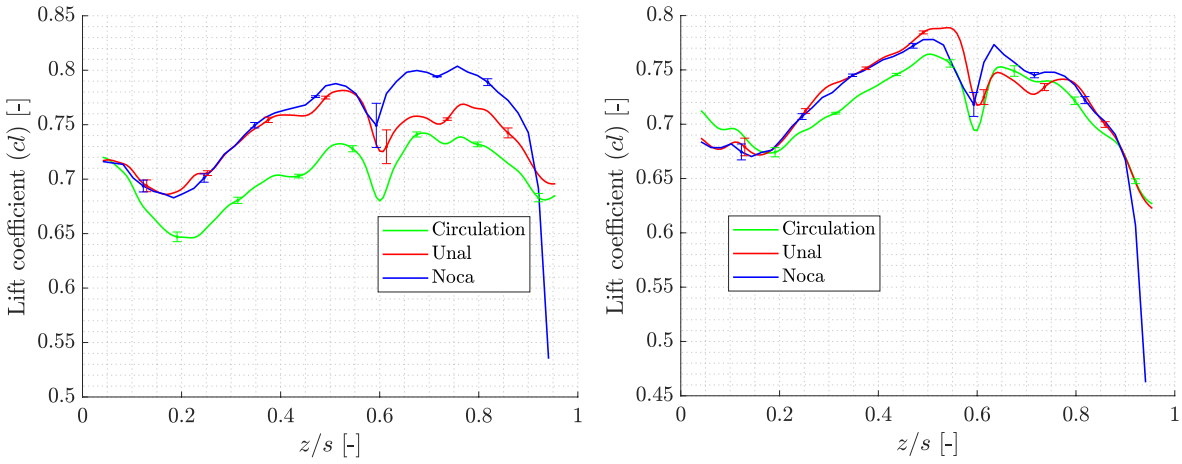

(a) $t/T_{ref} = 0$ (b) $t/T_{ref} = 0.16$

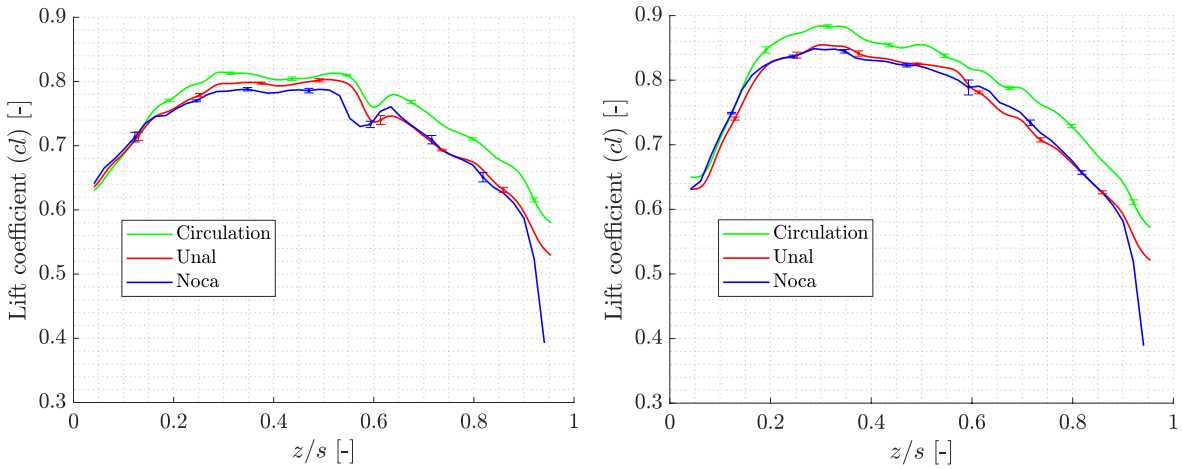

(c) $t/T_{ref} = 0.32$ (d) $t/T_{ref} = 0.48$

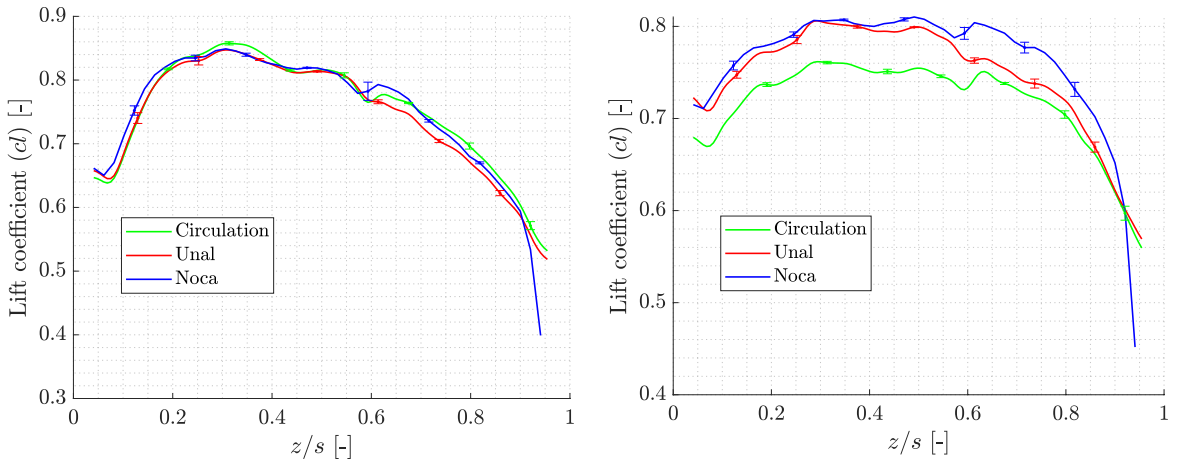

(e) $t/T_{ref} = 0.64$ (f) $t/T_{ref} = 0.80$

Figure 6.33: Spanwise distribution of the sectional lift coefficient at various time-instant. Results corresponding to Dynamic Case 2 ($\alpha_0 = 10°$; $\beta = 5°$; f = 3.2 Hz).

6.3.2. Integral results

Integral lift loads are compared to baseline force balance measurements to assess the accuracy and precision of the proposed load determination methods under dynamic inflow conditions. As described in Section 4.7, two dynamic test cases are proposed for this purpose: a first case with limited structural deformations where the attention is pointed towards the flow unsteadiness and its effects on the proposed methods (Dynamic Case 1, Table 4.3) and a second test case showing large structural displacements and non-linear structural and aerodynamic effects with lower interest in the effects of flow unsteadiness (Dynamic Case 2, Table 4.3).

Time-dependent lift force signal

Concerning lift forces experienced by the flexible wing under the established test conditions (Table 4.3), the temporal evolution of their magnitude is obtained implementing methods similar to those followed in previous sections (Section 6.3.1) during the analysis of sectional aerodynamic forces.

First, as done in Static test cases (Section 6.2.2), lift forces are evaluated in each control volume configuration at every time-instant (phase) considered for the analysis (N_{phases} = 25) through the numerical integration of the spanwise distribution of the lift coefficient. Once these discrete temporal values are recognized, non-linear regression models (sinusoidal fits) are used to define continuous force signals comparable to the reference force balance results (Section 5.5). However, as shown in Section 6.3.1, the presence of non-linear aerodynamic and structural phenomena preclude the employment of such sinusoidal fits in the uppermost region of the flexible wing. For this reason, this approach is limited to Dynamic Case 1 (Table 4.3), while linear interpolations between phase results are chosen to obtain a continuous description of the integral lift forces in Dynamic Case 2 (Table 4.3).

On the other hand, extra processing efforts should be taken when the circulation approach is employed to reconstruct the time-dependent lift force through sinusoidal fits in Dynamic Case 1. As already stated in Section 6.1, Kutta-Joukowski's theorem in its unsteady formulation (Equation 2.12) presents dependence on the location of the downstream control volume boundary, as the unsteady wake of the wing contains the history of the shed vorticity that produces a shift in the resultant lift force. Consequently, the lift force values obtained at each phase for every control volume configuration must be corrected before the sinusoidal fit is executed on the discrete results of Dynamic Case 1. The theoretical magnitude of the time-shift induced by the distance of the downstream control volume boundary to the wing trailing-edge is $\tau = (\Delta x)/U_\infty$; where Δx is the distance to the wing trailing edge and U_∞ is the freestream velocity at which the vorticity in the wake is shed. The corrected and fitted signal of the lift force reconstructed through Kutta-Joukowski's theorem is shown in Figure 6.34.

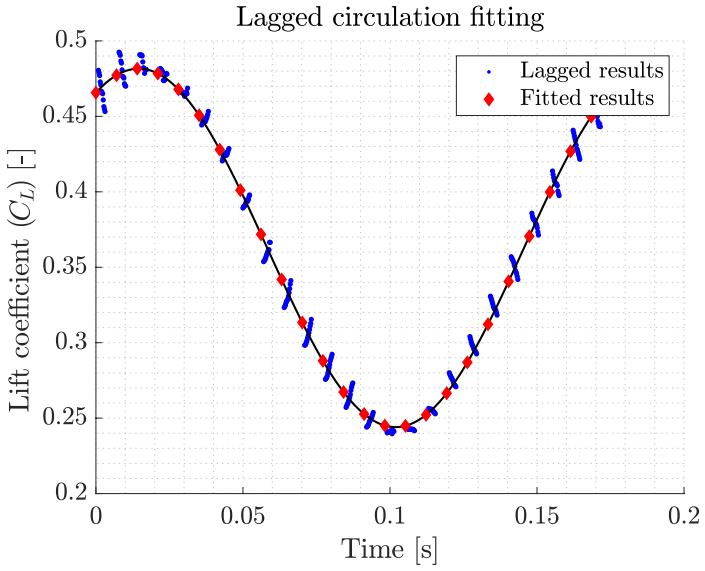

Figure 6.34: Reconstructed Kutta-Joukowski lift force signal. Results corresponding to Dynamic Case 1 (α_0 = 5° ; β = 5° ; f = 5.7 Hz).

Alternatively, to minimize the impact of the wake-induced time-lag associated to the Kutta-Joukowski theorem in Dynamic Case 2, the location of the downstream control volume boundary is fixed at the closest location to the wing trailing-edge ($d_{min} \approx 0.2 \cdot c$ according to the results observed in Section 6.1.1), while the remaining control volume boundaries are displaced as done in the resting test cases.

The temporal evolution of the integral lift coefficient in both dynamic test cases is shown in Figure 6.35, together with the reference force balance signal employed to assess the accuracy and precision of the different load determination methods. The magnitude of the deviations in the mean lift force and in the amplitude and time-shift of its signal for both dynamic test cases is shown and discussed from Table 6.2 to Table 6.4.

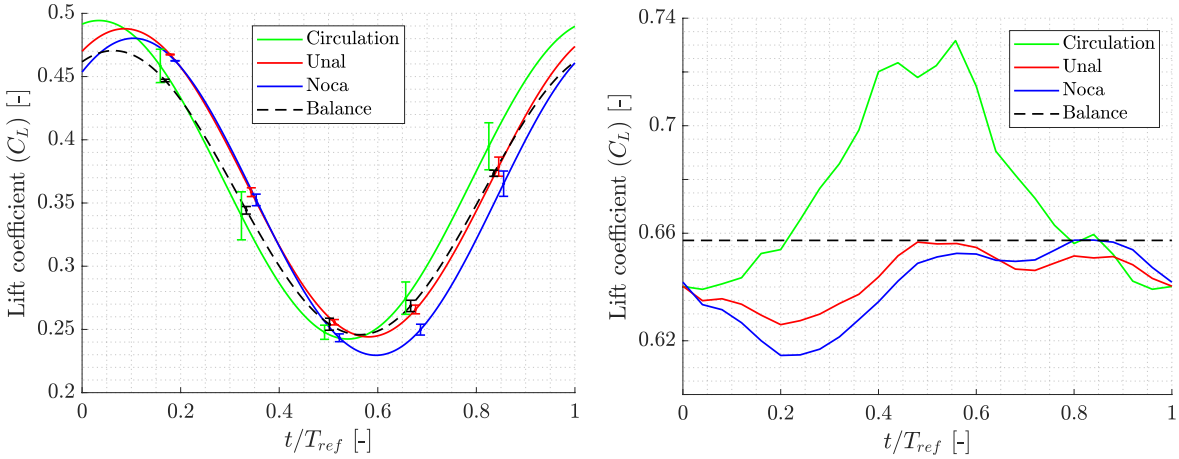

(a) Dynamic Case 1 ($\alpha_0 = 5°$; $\beta = 5°$; f = 5.7 Hz).

(b) Dynamic Case 2 ($\alpha_0 = 10°$; $\beta = 5°$; f = 3.2 Hz).

Figure 6.35: Time-dependent integral lift coefficient signal in Dynamic test cases.

With respect to the magnitude of the mean lift coefficient obtained with the proposed load determination methods, it can be easily appreciated; both in Figure 6.35 and in Table 6.2; that its value is very close to that of the reference force balance measurements independently of the load reconstruction method employed and of the test case being considered. Deviations between −3% and 3% of the reference mean lift coefficient are encountered for all methods in every test case; except for the circulation approach (Kutta-Joukowski theorem) in Dynamic case 2, where such deviation reaches a value of about 4.6% of the force balance mean lift coefficient. The magnitude of these errors is similar to that encountered in the analysis of the integral lift coefficient in Static Cases (Figure 6.17 and Table 6.1).

	Balance (ref.)		**Kutta-Joukowski**		**Unal**		**Noca**	
	$\overline{C_L}$ [-]	ϵ	$\overline{C_L}$ [-]	ϵ	$\overline{C_L}$ [-]	ϵ	$\overline{C_L}$ [-]	ϵ
Case 1	0.358	-	0.368	2.79%	0.366	2.23%	0.351	-1.96%
Case 2	0.657	-	0.687	4.57%	0.643	-2.13%	0.640	-2.59%

Table 6.2: Mean lift coefficient and deviation to the reference balance results in Dynamic test cases

Regarding the lift signal amplitude, its analysis is limited to Dynamic Case 1, as so is the sinusoidal fitting of the results due to the presence of non-linear effects in Dynamic Case 2 (Section 6.3.1). As seen in Figure 6.35a and Table 6.3, the deviation between the reconstructed signal amplitudes and the reference amplitude resembles about a 10% of the magnitude of the latter, which in absolute values corresponds to $\epsilon_{A_{C_L}} \approx 0.013$.

	Balance (ref.)		**Kutta-Joukowski**		**Unal**		**Noca**	
	A_{C_L} [-]	ϵ	A_{C_L} [-]	ϵ	A_{C_L} [-]	ϵ	A_{C_L} [-]	ϵ
Case 1	0.112	-	0.126	12.50%	0.122	8.93%	0.125	11.61%

Table 6.3: Lift coefficient amplitude and deviation to the reference balance results in Dynamic test cases

In relation to the temporal character of the lift coefficient signals and their comparison to the reference force balance measurements, the process is once again limited to Dynamic Case 1. The temporal character of the lift coefficient results is analyzed by means of the signal time-shift, which is directly obtained from the phase-lag coefficient obtained during the sinusoidal fit of the discrete results. As it can be clearly appreciated in Figure 6.35a and Table 6.4, the absolute value of the deviations between the time-shift of the reconstructed lift forces and the reference balance measurements is similar in all load reconstruction approaches (about 2.5% of the reference signal period). Nevertheless, while the Kutta-Joukowski theorem (circulation approach) shows an advancing trend (negative sign in the error weight), both momentum conservation approaches (Unal and Noca) exhibit delaying behaviours with respect to the reference force balance measurements.

	Balance (ref.)		**Kutta-Joukowski**		**Unal**		**Noca**	
	$\tau/\mathbf{T}$ [-]	ϵ	$\tau/\mathbf{T}$ [-]	ϵ	$\tau/\mathbf{T}$ [-]	ϵ	$\tau/\mathbf{T}$ [-]	ϵ
Case 1	0.062	-	0.038	-2.40%	0.082	2.00%	0.094	3.20%

Table 6.4: Lift coefficient time-shift and deviation to the reference balance results in Dynamic test cases

7

Conclusions & Recommendations

In this chapter, the most relevant outcomes of the research conducted in this thesis are presented. The overall performance of Lagrangian Particle Tracking (LPT) to assess aerodynamic forces over flexible test objects will be discussed, followed by various recommendations and indications for future investigations.

7.1. Conclusions

Experimental wind tunnel campaigns are still needed to identify the most relevant phenomena involved in FSI and validate low-fidelity models employed to characterize complex aeroelastic problems. Such phenomena result from the combination of forces of different nature (inertial, elastic and aerodynamic). For this reason, both structural and flow quantities must be determined during such experimental campaigns. As described in the literature review, these quantities are typically acquired employing various measurement systems. Nevertheless, these measurement systems imply certain limitations and undesired effects, among which the most relevant are their spatial resolution, the density of the acquired information, their intrusiveness and the complexity of the needed experimental setup.

This thesis is part of the research effort to overcome the most relevant limitations of conventional measurements systems and define alternatives capable of providing full-field and simultaneous information of both flow and structural quantities during aeroelastic wind tunnel measurements in a non-intrusive way. The state-of-the-art technique for quantitative velocity flowfield measurements (PIV), has been recently proven to be capable of retrieving data of both structural and aerodynamic interfaces in wind tunnel investigations.

The aim of this research project is to take a step further and assess its capabilities to reconstruct the most relevant aerodynamic forces on such a relevant aeroelastic problem as a gust encounter by a highly flexible wing. To do so, the following research objective has been defined:

"Evaluate the capabilities of Lagrangian Particle Tracking to determine the aerodynamic loads acting on large-scale flexible bodies by means of the experimental investigation of a highly-flexible wing subjected to both steady and unsteady inflow conditions."

To reach this goal, a wind tunnel experimental campaign has been developed in the Open Jet Facility (OJF) at TU Delft. The test object consists of a highly-flexible wing mounted vertically on a force balance, whose measurements are taken as a reference to validate the optical results. The experimental model has been provided with a pattern of reflective markers distributed over its surface to permit the reconstruction and evaluation of its structural response. The test cases that have been employed in this experimental investigation to reach the defined research goal included both steady and unsteady (periodic) inflow conditions. The latter has been achieved through the operation of a gust generator mounted at the nozzle of the open-jet wind tunnel.

Once the experimental campaign has been conducted, raw PIV data has been treated and pre-processed following a well-defined methodology to extract significant information about the wing dynamics and the aerodynamic forces acting on it. First, structural markers and HFSB have been isolated employing filtering

operations. Then, surface reflective dots and flow particles have been traced independently. Afterwards, data from different measurement volumes has been merged into a single data set which includes information of the flow and the structure dynamics along the entire wing span. Subsequently, Lagrangian particle tracks have been transformed through ensemble averaging procedures. These procedures have been implemented trying to minimize the influence of measurement errors and noise in the final Eulerian description of the flowfield surrounding the wing.

Finally, the aerodynamic loads acting over the test object have been reconstructed from this pre-processed data employing three different approaches: the integral momentum conservation equation in its classical formulation (Unal et al. 1997); the integral momentum conservation equation with an alternative formulation based on vorticity that prevents the explicit determination of pressure (Noca et al. 1999); and Kutta-Joukowski theorem. The accuracy and precision of the forenamed methods have been assessed with reference force balance measurements.

The first analysis that has been conducted on the reconstructed aerodynamic loads is the examination of their sensitivity to several setup parameters like the spatial discretization of the Eulerian flowfield or the location of the control volume boundaries.

The most relevant observation encountered regarding the sensitivity of the proposed load determination methods to the spatial discretization of the Eulerian data, is that all procedures show similar sensitivities to this parameter. Moreover, it is deducted that very small bins ($l_B < 7.5$ mm) should be avoided to minimize the impact of numerical errors in the resultant aerodynamic loads. However, the size of the interrogation windows should be maintained at a moderate level ($l_B \approx 0.1 \cdot c$) to avoid an excessive dissipation of flow phenomena and structures (e.g. shed vortices or suction peak magnitude) that might alter the resultant forces.

Concerning the sensitivity of the described techniques to the shape and size of the control volume and integration paths (location of their boundaries), two different trends are appreciated in the results: On the one hand, all load determination methods show similar reactions to the positioning of the control volume boundaries when the lift force magnitude is considered. On the other hand, results show that momentum conservation methods (both Unal and Noca formulations) present greater sensitivity to the location of the control volume limits when the temporal character of the aerodynamic loads in dynamic test cases is considered. This increased sensitivity is more pronounced on the downstream (trailing-edge) control volume boundaries. From this analysis, it can be concluded that control volume limits should not be closer than $d_{min} = 0.2 \cdot c$ to any point in the wing surface to avoid the undesired influence of measurement errors and variations in the lift force magnitude. In addition, it is advisable to employ several control volume configurations and average their results to minimize the impact of random error present in the Eulerian flowfield.

With respect to the assessment of the accuracy and precision of the load determination methods in test cases involving steady inflow conditions (Static Cases, Table 4.3), all force reconstruction techniques show results in good agreement with reference balance measurements. Deviations in the integral wing lift coefficient reach maximums of a 3% of the reference lift in Noca's formulation, while they stay below a 1% of it for the remaining methods. Furthermore, the spanwise distribution of the reconstructed sectional lift forces resembles their theoretical disposal if external conditions, such as the presence of the splitting table boundary layer, are taken into account.

Additionally, the described procedures are proven capable of obtaining alternative information, like the spanwise location of the wing center of pressure, that is relevant for the characterization of aeroelastic problems. Such quantity is determined accurately in both Static Cases (deviations of about 5% of the wing span neglecting the effect of the wingtip rod) independently of the load reconstruction method employed in the process.

Regarding the assessment of the performance of the force reconstruction procedures in cases involving unsteady inflow conditions (Dynamic Cases, Table 4.3), several observations can be made from the results obtained. First, it is clear that all methods are capable of retrieving temporal information of both sectional and integral aerodynamic loads and combine them with structural data to analyze the complete FSI problem. In addition, it is possible to examine the load generation mechanisms to explain the aerodynamic and structural behaviour of the test model employed in the experimental aeroelastic investigation.

Finally, the complete analysis of the accuracy and precision of the force determination techniques is limited to Dynamic Case 1 (Table 4.3), where the structural deflections of the flexible wing are limited and the emphasis is made on the unsteady nature of the flow. The reason behind the limitations in the analysis of Dynamic Case 2 (Table 4.3) is the presence of non-linear aerodynamic and structural phenomena that prevent a periodic description of the wing behaviour and thus a proper comparison with the reference force balance measurements. Nevertheless, with the available information, it can be concluded that all methods perform similarly; being the greatest difference between them the temporal character of the reconstructed forces: while Kutta-Joukowski theorem tends to advance the reference signal, both momentum conservation methods (Unal & Noca) tend to shift their results in time after the force balance measurements. The absolute value of such temporal deviations to the reference means, approximately, a 2.5% of the oscillation period for all methods.

All in all, these results show the feasibility of optical non-intrusive measurement systems to characterize the aerodynamic loads in aeroelastic wind tunnel investigations with acceptable accuracy and precision. In addition, it has also been demonstrated that the range of information provided by these techniques is superior to that achievable with conventional measurement devices limited to pointwise and integral quantities: Results can be both local and integral, LPT data can be employed to analyze and identify the load generation mechanisms and the simultaneous tracking of surface reflective markers also permits the improvement of the overall FSI event characterization.

7.2. Recommendations

This last section presents a series of recommendations that have been formulated during the execution of this research project. These recommendations range from practical tips to take into account during the acquisition and processing of the experimental data to possible research gaps to consider in future projects.

In first place, although the proposed experimental setup has been proven effective to conduct large-scale measurements over the entire wing span of both structural and flow quantities, several processing steps are required to do so. The efforts taken could be drastically minimized if certain modifications in the experimental setup were considered and implemented. Such modifications mainly focus on expanding the available measurement volume while ensuring the accuracy of the LPT system. The proposed changes are the following:

- Increase the number of optical sensors (cameras) to allow the simultaneous measurement of both airfoil sides (suction and pressure) and of the complete wing span.
- Increase the size of the illumination system to adapt to the increased size of the measurement volume.
- Improve the seeding density and increase the size of the flow tracers stream to enclose the entire wing span.

Similarly, various changes can be included in the different processing steps taken throughout this project. Among them, the most relevant relate to the ensemble-averaging (binning) procedures: Taking advantage of the structure information, the shape of the interrogation windows at the vicinity of the wing surface could be adapted to accurately reproduce the reconstructed airfoil section. Besides, non-regular bin sizes could also be employed to account for the different discretization requirements across the entire measurement volume and binning directions; thus reducing the computational cost of the ensemble-averaging algorithms while maintaining the accuracy of the resultant Eulerian fields.

On another note, various modifications can also be implemented to the test object to facilitate the assessment of the non-intrusive load determination techniques. Due to its high flexibility, the wing model experiences some uncontrolled structural vibrations when large angles of attack are considered, even if the inflow conditions are steady. As a consequence, the evaluation of the force reconstruction procedures is limited to the linear region of the polar plot in static test cases. For this reason, it is recommended to employ stiffer test objects, with the consequent downturn of the aeroelastic phenomena arising in unsteady inflow conditions, if these flow regimes want to be analyzed in more detail.

Taking into account the results presented throughout this thesis, all load determination techniques (Kutta-Joukowski, Unal and Noca) seem to be valid to reconstruct the aerodynamic loads acting on flexible structures during aeroelastic wind tunnel experiments at the considered flow and structure regimes: steady inflow conditions with limited structural deformations and fully attached flows (Static Case 1); steady inflow conditions with greater structural deflections and limited flow viscous effects (Static Case 2); and unsteady inflow conditions with limited structural deflections and almost fully attached flow at moderate reduce frequencies that ensure unsteady aerodynamic phenomena (Dynamic Case 2).

For this reason, considering the processing efforts required for each of the described methods, the Kutta-Joukowski theorem is recommended as the preferred force reconstruction technique in the forenamed conditions. Nevertheless, further attempts should be made to obtain reference results under non-linear structural and aerodynamic regimes to assess the feasibility and the potential of each of the load determination methods in such conditions. Aside from the test object modifications mentioned previously, other changes in the experimental setup could be implemented to do so: One the one hand, adjustments in the experimental setup could be taken to attempt to analyze the instantaneous aerodynamic forces acting on the test object, thus preventing the use of phase-average approaches. Alternatively, reference measurement systems capable of obtaining sectional results to compare with could also be employed to improve the quality of the analysis in such complex test cases.

Finally, some possible lines of research that future work should explore to complement the present study are:

- Apply the described methodologies to test cases involving greater flow speeds to evaluate their validity at Reynolds numbers close to reality (free-flight conditions).
- Explore the capabilities of Lagrangian Particle Tracking to retrieve time-resolved forces in large-scale aeroelastic experiments. By doing so, relevant discrete aeroelastic problems could be analyzed.
- Re-assess the performance of the described procedures in non-linear aerodynamic and structural applications making use of improved reference measurement systems to validate them.
- Develop structural models that permit the determination of elastic structural forces from the processed position of the surface markers. Such results would permit the complete characterization of the Fluid-Structure Interaction problem single non-intrusive optical measurement system (Lagrangian Particle Tracking).

Bibliography

[1] N. Agüera, G. Cafiero, T. Astarita, and S. Discetti. "Ensemble 3D PTV for high resolution turbulent statistics". *Measurement Science and Technology* 27 (2016), p. 124011. DOI: 10.1088/0957-0233/27/12/124011.

[2] J. D. Anderson Jr. *Fundamentals of Aerodynamics*. 6th Edition. McGraw Hill Education, 2017. ISBN: 9780198520115.

[3] M. P. Arroyo and C. Greated. "Stereoscopic Particle Image Velocimetry". *Measurement Science and Technology* 2 (1991), pp. 1181–1186. DOI: 10.1088/0957-0233/2/12/012.

[4] High Level Group in Aviation Research. "Flightpath 2050 Europes Vision for Aviation". *European Comission and Directorate-General for Mobility and Transport and Directorate-General for Research and Innovation* (2011). DOI: 10.2777/50266.

[5] O. Avin, D. R. Raveh, A. Drachinsky, Y. Ben-Shmuel, and M. Tur. "An experimental benchmark of a very flexible wing". *AIAA Scitech 2021 Forum* (2021). DOI: 10.2514/6.2021-1709.

[6] G. K. Batchelor. *An Introduction to Fluid Dynamics*. 2nd Edition. Cambridge University Press, 1967. ISBN: 8185618240.

[7] T. Baur and J. Köngeter. "PIV with high temporal resolution for the determination of local pressure reductions from coherent turbulent phenomena". *3rd International Workshop on Particle Image Velocimetry* 29 (1999), pp. 101–106.

[8] J. Bosbach, M. Kühn, and C. Wagner. "Large scale particle image velocimetry with helium filled soap bubbles". *Experiments in Fluids* 46 (2009), pp. 539–547. DOI: 10.1007/s00348-016-2277-7.

[9] G. C. A. Caridi, D. Ragni, A. Sciachitano, and F. Scarano. "HFSB seeding for largescale tomographic PIV in wind tunnels". *Experiments in Fluids* 57 (2016), pp. 56–190. DOI: 10.1007/s00348-016-2277-7.

[10] C. Cierpka, B. Lütke, and C. J. Kähler. "Higher order multi-frame particle tracking velocimetry". *Experiments in Fluids* 54 (2013), p. 1533. DOI: 10.1007/s00348-013-1533-3.

[11] A. R. Collar. "The expanding domain of aeroelasticity". *Journal of the Royal Aeronautical Society* 50 (1946), pp. 613–636. DOI: 10.1017/S0368393100120358.

[12] L. David, T. Jardin, and A. Farcy. "On the non-intrusive evaluation of fluid forces with the momentum equation approach". *Measurement Science and Technology* 20 (2009), p. 095401. DOI: 10.1088/0957-0233/20/9/095401.

[13] G. Dietz, G. Schewe, F. Kiessling, and M. Sinapius. "Limit-Cycle-Oscillation experiments at a transport aircraft wing model". 2003.

[14] G. E. Elsinga, B. Scarano F. Wieneke, and B. W. van Oudheusden. "Tomographic particle image velocimetry". *Experiments in Fluids* 41 (2006), pp. 933–947. DOI: 10.1007/s00348-006-0212-z.

[15] C. J. S. Ferreira, G. J. W. van Bussel, G. A. M. van Kuik, and F. Scarano. "On the use of velocity data for load estimation of a VAWT in dynamic stall". *Journal of Solar Energy Engineering* 133 (2011), pp. 432–441. DOI: 10.1115/1.4003182.

[16] K. Gharali and D. A. Johnson. "PIV-based load investigation in dynamic stall for different reduced frequencies". *Experiments in Fluids* 55 (2014), pp. 1–12. DOI: 10.1007/s00348-014-1803-8.

[17] D. Giaquinta and A. Sciacchitano. "Investigation of the Ahmed body cross-wind flow topology by robotic volumetric PIV". *13th International Symposium on Particle Image Velocimetry ISPIV* (2019).

[18] D. Gkiolas, F. Mouzakis, and D. S. Mathioulakis. "Stall flutter measurements on a rectangular wing". *ASME 2018 5th Joint US-European Fluids Engineering Division Summer Meeting, FEDSM* 1 (2018). DOI: 10.1115/FEDSM2018-83162.

[19] A. Guissart, L. P. Bernal, G. Dimitriadis, and V. E. Terrapon. “PIV-based estimation of unsteady loads on a flat plate at high angle of attack using momentum equation approaches”. *Experiments in Fluids* 58 (2017), pp. 1–17. DOI: 10.1007/S00348-017-2335-9.

[20] F. E. Harris. *Mathematics for Physical Science and Engineering*. 1 st Edition. Academic Press, 2014. ISBN: 978-0128010006.

[21] T. Jardin, L. Chatellier, A. Farcy, and L. David. “Correlation between vortex structures and unsteady loads for flapping motion in hover”. *Experiments in Fluids* 47 (2009), pp. 655–664. DOI: 10.1007/s00348-009-0658-x.

[22] C. Jux, A. Sciacchitano, and J. F. G. Schneiders. “Robotic volumetric PIV of a full-scale cyclist”. *Experiments in Fluids* 59 (2018), p. 74. DOI: 10.1007/s00348-018-2524-1.

[23] C. J. Kähler and J. Kompenhans. “Fundamentals of multiple plane stereo particle image velocimetry”. *Experiments in Fluids* 29 (2000), pp. 70–77. DOI: 10.1007/S003480070009.

[24] D. F. Kurtulus, F. Scarano, and L. David. “Unsteady aerodynamic forces estimation on a square cylinder by TR-PIV”. *Experiments in Fluids* 42 (2006), pp. 185–196. DOI: 10.1007/s00348-006-0228-4.

[25] P. Lancelot, J. Sodja, N. Werter, and R. de Breuker. “Design and testing of a low subsonic wind tunnel gust generator”. *Advances in Aircraft and Spacecraft Science* 4 (2017), pp. 125–144. DOI: 10.12989/aas.2017.4.2.125.

[26] J. Lighthill. “Fundamentals concerning wave loading on offshore structures”. *Journal of Fluid Mechanics* 173 (1996), pp. 667–681. DOI: 10.1017/S0022112086001313.

[27] L. E. M. Lignarolo. “On The Turbulent Mixing in Horizontal Axis Wind Turbine Wakes”. *PhD thesis, Delft University of Technology* (2016).

[28] X. Liu and J. Katz. “Instantaneous pressure and material acceleration measurements using a four-exposure PIV system”. *Experiments in Fluids* 41 (2006), pp. 227–240. DOI: 10.1007/s00348-006-0152-7.

[29] R. van de Meerendonk, M. Percin, and B. W. van Oudheusden. “Three-dimensional flow and load characteristics of a flexible revolving wings”. *Experiments in Fluids* 59 (2018), p. 161. DOI: 10.1007/s00348-018-2613-1.

[30] A. Melling. “Tracer particles and seeding for particle image velocimetry”. *Measurements, Science and Technology* 8 (1997), pp. 1406–1416. DOI: 10.1088/0957-0233/8/12/005.

[31] C. Mertens, B.W. van Oudheusden, J. Sodja, and A. Sciacchitano. “Determination of Collars Triangle of Forces on a Flexible Wing based on Particle Tracking Velocimetry Measurements”. *(AIAA Scitech 2021 Forum). American Institute of Aeronautics and Astronautics Inc.* (2021), pp. 1–22. DOI: 10.2514/6.2021-0221.

[32] C. Mertens, A. Sciacchitano, B. W. van Oudheusden, and J. Sodja. “An integrated measurement approach for the determination of the aerodynamic loads and structural motion for unsteady airfoils”. *Journal of Fluids and Structures* 103 (2021), p. 103293. DOI: 10.1016/j.jfluidstructs.2021.103293.

[33] F. M. A. Mitrotta, J. Sodja, and A. Sciacchitano. “On the combined ow and structural measurements via Robotic Volumetric PTV”. *Measurement Science and Technology* 33 (Dec. 2021), p. 045201. DOI: 10.1088/1361-6501/ac41dd.

[34] A. Mohebbian and D. E. Rival. “Assessment of the derivative-moment transformation method for unsteady load estimations”. *Experiments in Fluids* 53 (2012), pp. 319–330. DOI: 10.11575/PRISM/4904.

[35] B. Moulin and M. Karpel. “Gust Loads Alleviation Using Special Control Surfaces”. *Journal of Aircraft* 44 (2007), pp. 17–25. DOI: 10.2514/1.19876.

[36] J. Mullin and W. J. A. Dahm. “Dual-plane stereo particle image velocimetry (DSPIV) for measuring velocity gradient fields at intermediate and small scales of turbulent flows”. *Experiments in Fluids* 38 (2005), pp. 185–196. DOI: 10.1063/1.2166447.

[37] K. Nishino, N. Kasagi, and M. Hirata. "Three-Dimensional Particle Tracking Velocimetry Based on Automated Digital Image Processing". *Trans. of the ASME J. Fluid Eng.* 111 (1989), pp. 384–389. DOI: 10.1115/1.3243657.

[38] F. Noca, D. Shiels, and D. Jeon. "A comparison of methods for evaluating time-dependent fluid dynamic forces on bodies, using only velocity fields and their derivatives". *Journal of Fluid and Structures* 13 (1999), pp. 551–578. DOI: 10.1006/jfls.1999.0219.

[39] B. W. van Oudheusden. "PIV-based pressure measurement". *Measurement Science and Technology* 24 (2013), p. 032001. DOI: 10.1088/0957-0233/24/3/032001.

[40] B. W. van Oudheusden, E. W. F. Casimiri, and F. Scarano. "Aerodynamic load characterisation of a low speed aerofoil using particle image velocimetry". *The Aeronautical Journal* 112 (2008), pp. 197–205. DOI: 10.1017/S000192400000213X.

[41] P. C. B. Phillips and J. Y. Park. "On the Formulation of Wald Tests of Nonlinear Restrictions". *Econometrica* 56 (1988), pp. 1065–1083. DOI: 10.2307/1911359.

[42] M. Raffel, C. E. Willert, S. T. Wereley, and J. Kompenhans. *Particle Image Velocimetry: A Practical Guide*. 2 nd Edition. Experimental Fluid Mechanics. Springer International Publishing, 2018. ISBN: 3540723072.

[43] D. Ragni, B. W. van Oudheusden, and F. Scarano. "Non-intrusive aerodynamic loads analysis of an aircraft propeller blade". *Experiments in Fluids* 51 (2011), pp. 361–371. DOI: 10.1007/s00348-011-1057-7.

[44] T. de Rojas. "Integrated Aerodynamic and Structural Measurements of the Gust Response of a Flexible Wing with Robotic PIV". *MSc thesis, Delft University of Technology* (2020).

[45] A. Savitzky and M. J. E. Golay. "Smoothing and Differentiation of Data by Simplified Least Squares Procedures". *Analytical Chemistry* 36 (1964), pp. 1627–1639. DOI: 10.1021/ac60214a047.

[46] F. Scarano. "Tomographic PIV: principles and practice". *Measurement Science and Technology* 24 (2013), p. 012001. DOI: 10.1088/0957-0233/24/1/012001.

[47] F. Scarano, K. Bryon, and D. Violato. "Time-resolved analysis of circular and chevron jets transition by tomo-PIV". *15th Int Symp on Applications of Laser Techniques to Fluid Mechanics* 23 (2010), p. 124104. DOI: 10.1063/1.3665141.

[48] F. Scarano, S. Ghaemi, G. C. A. Caridi, J. Bosbach, U. Dierksheide, and A. Sciacchitano. "On the use of heliumfilled soap bubbles for largescale tomographic PIV in wind tunnel experiments". *Experiments in Fluids* 56 (2015), p. 42. DOI: 10.1007/s00348-015-1909-7.

[49] F. Scarano and C. Poelma. "Three-dimensional vorticity patterns of cylinder wakes". *Experiments in Fluids* 47 (2009), pp. 69–83. DOI: 10.1007/s00348-009-0629-2.

[50] D. Schanz, S. Gesemann, and A. Schröder. "Shake-The-Box: Lagrangian particle tracking at high particle image densities". *Experiments in Fluids* 57 (2016), p. 70. DOI: 10.1007/s00348-016-2157-1.

[51] J. F. G. Schneiders, F. Scarano, C. Jux, and A. Sciacchitano. "Coaxial volumetric velocimetry". *Measurement Science and Technology* 29 (2018), p. 065201. DOI: 10.1088/1361-6501/aab07d.

[52] A. Sciacchitano and F. Scarano. "Elimination of PIV light reflections via a temporal high pass filter". *Measurement Science and Technology* 25 (2014), p. 084009. DOI: 10.1088/0957-0233/25/8/084009.

[53] W. R. Sears. "Some Aspects of Non-Stationary Airfoil Theory and Its Practical Application". *Journal of the Aeronautical Sciences* 8 (1941), pp. 104–108. DOI: 10.2514/8.10655.

[54] S. D. Sharma and P. J. Deshpande. "Kutta-Joukowski theorem in viscous and unsteady flows". *Experiments in Fluids* 52 (2012), pp. 1581–1591. DOI: 10.1007/s00348-012-1276-6.

[55] J. J. H. M. Sterenborg, R. C. J. Lindeboom, C. J. S. Ferreira, A. H. van Zuijlen, and H. Bijl. "Assessment of PIV-based unsteady load determination of an airfoil with actuated flap". *Journal of Fluids and Structures* 45 (2014), pp. 79–95. DOI: 10.1016/j.jfluidstructs.2013.12.001.

[56] T. Theodorsen. "General theory of aerodynamic instability and the mechanism of flutter". *NACA* TR No. 496 (1934), pp. 291–311. DOI: 2060/19800006788.

[57] T. Tronchin, L. David, and A. Farcy. “Loads and pressure evaluation of the flow around a flapping wing from instantaneous 3D velocity measurements”. *Experiments in Fluids* 56 (2013), pp. 1–16. DOI: 10.1007/S00348-014-1870-X.

[58] M. F. Unal, J. C. Lin, and D. Rockwell. “Force prediction by PIV imaging: a momentum-based approach”. *Journal of Fluid and Structures* 11 (1997), pp. 965–971. DOI: 10.1006/jfls.1997.0111.

[59] A. Villegas and F. J. Diez. “Instantaneous aerodynamic load calculations in rotating airfoils from time resolved PIV measurements at low Reynolds number”. *ASME 2013 International Mechanical Engineering Congress and Exposition* 7B (2013), p. 20. DOI: 10.1115/IMECE2013-65850.

[60] E. W. Weisstein. *Wolfram MathWorld - Circle-Circle Tangents*. 1999. URL: https://mathworld.wolfram.com/Circle-CircleTangents.html (visited on 12/15/2020).

[61] B. Wieneke. “Iterative reconstruction of volumetric particle distribution”. *Measurement Science and Technology* 24 (2013), p. 024008. DOI: 10.1088/0957-0233/24/2/024008.

[62] N. Wiener. *Extrapolation interpolation and smoothing of stationary time series*. 1 st Edition. MIT Press, Cambridge, 1949. ISBN: 9780262257190.

[63] J. C. Wu. “Theory for aerodynamic force and moment in viscous flows”. *AIAA Journal* 19 (1981), pp. 432–441. DOI: 10.2514/3.50966.

[64] J. Z. Wu, Z. L. Pan, and X. Y. Lu. “Unsteady fluid-dynamic force solely in terms of control-surface integral”. *Physics of Fluids* 17 (2005), p. 098102. DOI: 10.1063/1.2055528.